UNIVERSIDAD POLITÉCNICA DE MADRID
Escuela Técnica Superior de Ingeniería Aeronáutica y del Espacio



High order methods for the generation and propagation of wind turbine aeroacoustics

DOCTORAL THESIS

Submitted for the degree of Doctor by:

Oscar Andrés Mariño Sánchez
Mechanical Engineer

Madrid, 2024





UNIVERSIDAD POLITÉCNICA DE MADRID
Escuela Técnica Superior de Ingeniería Aeronáutica y del Espacio

Doctoral Degree in Aerospace Engineering

High order methods for the generation and propagation of wind turbine aeroacoustics

DOCTORAL THESIS

Submitted for the degree of Doctor by:

Oscar Andrés Mariño Sánchez
Mechanical Engineer

Under the supervision of:
Dr. Eusebio Valero Sánchez
Dr. Esteban Ferrer Vaccarezza

Madrid, 2024

Title: High order methods for the generation and propagation of wind turbine aeroacoustics

Author: Oscar Andrés Mariño Sánchez

Doctoral Programme: Aerospace Engineering

Thesis Supervision:

Dr. Eusebio Valero Sánchez, Catedrático de Universidad (UPM)

Dr. Esteban Ferrer Vaccarezza, Profesor Titular de Universidad (UPM)

This thesis has received funding from the European Union's Horizon 2020 Research and Innovation Program under the Marie Skłodowska-Curie grant agreement No 860101.

Esta tesis ha recibido financiación del programa Horizon 2020 de investigación e innovavión de la Unión Europea bajo el acuerdo de beca número 860101 del programa Marie Skłodowska-Curie.

A Nati, gracias por ser mi apoyo.

Acknowledgement

This thesis would not have been possible without the people that have supported me during all the time that I have been involved in this journey of doing my Ph.D.

First of all, I want to thank my two thesis advisors, Eusebio and Esteban, for all the help and advice they have given me all this time. Thanks for all the talks with incredible patience that we have had all these 3 years, for all the advice for technical details, for the academic and for the general life. I have learnt so many thinks from you during the last years.

I would also like to thank all the people in the Department of Applied Mathematics in Aerospace Engineering of ETSIAE. To Gonzalo for all the advice and for leading the development of the code. To all the professors for all the kind talks, Jesús, Javi, Marta, Dani, Mariola, Miguel, Mario, Alex. Also, for all the amazing people who have worked with me, Himpu, Kenza, Kheir-Eddine, Nour, Beka, Stefano, Carlos, Jonathan, Iván, Martín, David, it was incredible working with you. Special thanks to Andrés (Mateo), Gerasimos, Wojciech and Andrés (Rueda, and yes I am including you as part of Numath), who helped me from the very start until the end, thanks for all the discussions and talks.

I am also grateful to all the people of zEPHRY, to all the professors, for the interesting questions and advice. To all the ESRs for all the memories that we created during our meetings. To all the people that made it possible to create such an amazing project and those who were able to make it real, both scientifically and administratively.

None of this would have been possible without the support of my family. I am very grateful for all the help that I have received from you, starting way before even starting to think about doing a Ph.D. and continuing to do so until now. I want to thank my parents, mom, dad and also Martha and Francisco, and my siblings, Laura, Luis, for all the unconditional support.

Last but not least, my incredible partner, Nati, who is without a doubt the most important person in my life. Thank you for all the incredible support, patience, help and more that you have given me during this time. Thanks for accompanying me during the good and bad times; it would have been impossible for me to overcome the first and not enjoy the second enough without you.

I would also like to thank the Supercomputing and Visualization Center of Madrid (CeSViMa) for providing me with computing resources; and thankfully acknowledge the computer resources at MareNostrum and the technical support provided by Barcelona Supercomputing Center (RES-IM-2022-3-0023). Finally, I would like to thank the European Union's Horizon

2020 Research and Innovation Program under the Marie Skłodowska-Curie grant agreement No 860101 for the zEPHYR project.

Abstract

This thesis focusses on computation methods for aeroacoustics of airfoil sections and wind turbines, when simulated using compressible Navier–Stokes (NS) equations discretised with the Discontinuous Galerkin Spectral Element Method (DGSEM). We consider airfoil sections (a blade section) to assess the accuracy in predicting noise using high-order techniques to then propose an acoustic prediction method for the rotating turbines.

First, we study the airfoil level by assessing the fundamental phenomena influencing aeroacoustics in the context on Large Eddy Simulations (LES), including mesh refinement for high-order simulations (including h/p refinement) and the turbulence closure. We compare explicit LES (Vreman, Wale) and implicit LES (energy/entropy stable formulation and a new jump penalisation technique).

Second, we study two ways to calculate acoustics. The first one considers well-resolved simulations (direct approach), while the second separates generation and propagation of acoustics using acoustic analogies. The former solves the generation and propagation simultaneously, by letting the compressible formulation capture wave acoustics. The low dissipative character of the high-order DG scheme is shown to be able to propagate waves with minimal errors. The latter approach alleviates the computational requirements by using an acoustic analogy (Ffowcs-Williams and Hawkings) to propagate the sound waves to the far field. We have compared both formulations, and proved the spectral convergence for both when using our DG formulation in airfoil sections.

Third, we propose a methodology to predict the aeroacoustics of wind turbines at a reduced cost. We use the Actuator Line (AL) method that replaces the blades of the wind turbine blades with rotating source terms and mimics blade rotation. We have compared two ways of integrating AL with DGSEM and we study the mesh and polynomial interaction with the model. Finally, we couple the AL method with Amiet's acoustic models, to allow the computation of the noise generated by the rotating blades, enabling the prediction of far field noise at reduced cost.

Keywords: computational fluid dynamics, high–order method discontinuous Galerkin, wind turbines, aeroacoustic, Navier–Stokes, compressible flows, Ffowcs Williams-Hawkings, Amiet.

Resumen

Esta tesis se centra en métodos computacionales para el cálculo de aeroacústica en perfiles aerodinámicos y turbinas de viento, solucionando la formulación compresible de las ecuaciones de Navier–Stokes, utilizando el método de *Discontinuous Galerkin Spectral Element Method* (DGSEM). Consideramos perfiles aerodinámicos (una sección de la pala de una turbina) para evaluar la precisión en la predicción de ruido utilizando métodos de alto orden, para posteriormente proponer una metodología para predecir el ruido de turbinas rotatorias.

Primero, estudiamos el nivel de perfil, evaluando fenómenos fundamentales importantes que afectan la acústica en el contexto de simulaciones de grandes vórtices (LES por sus sigas en ingles), donde se incluyen refinamiento de malla para simulaciones de alto orden (incluyendo refinamiento h/p) y cierre de problemas con turbulencia. Comparamos modelos LES explícitos (WALE y Vreman), y la versión implícita de LES (formulaciones estables de conservación de energía/entropía, y una nueva técnica de penalización)

Segundo, investigamos dos formulaciones para calcular la acústica. La primera considera simulaciones bien resultas en todo el dominio (enfoque directo), mientras que la segunda realiza una separación de la generación y la propagación de la acústica utilizando analogías. Para el primer caso, se resuelven ambas (generación y propagación) de forma simultanea, aprovechando que la formulación compresible captura las ondas acústicas. La baja disipación del método numérico de alto orden ha demostrado ser capas de propagar dichas ondas con mínimos errores. Por otro lado, en el segundo caso, el requerimiento computacional es aliviado al usar una analogía acústica (Ffowcs-Williams and Hawkings) para resolver la parte de propagación de la ondas hacia el campo lejano. Ambas formulaciones son comparadas y se prueba la convergencia espectral de la formulación DGSEM en perfiles aerodinámicos.

Tercero, proponemos una metodología para predecir aeroacústica de turbinas a bajo costo computacional. Utilizamos el modelo de linea actuadora (AL por sus siglas en ingles), donde las palas de la turbina son reemplazadas por términos fuentes en movimiento, las cuales reproducen las fuerzas ejercidas por las palas en rotación. Hemos comparado dos formas de integrar el modelo AL con DGSEM, y estudiado la interacción con el nivel de discretización, es decir el tamaño de la malla y el polinomio. Finalmente, hemos acoplado este modelo con los modelos acústico de Amiet, de forma tal que se puede calcular el ruido generado por la turbina entera y que es escuchado en el campo lejano con bajo coste.

Palabras clave: dinámica de fluidos computacional, método de alto orden Galerkin discontinuo, tubinas eólicas, aero acústica, Navier-Stokes, flujos compresibles.

Contents

Acknowledgement iii

Abstract v

Resumen vi

Contents **ix**

List of Figures **xiii**

List of Tables **xix**

Abbreviations **xxi**

1 Introduction **1**

1.1 Motivation 1

1.2 Objectives and Methodology 3

1.3 Outline 5

1.4 Contributions & Highlights 6

1.5 Notation 8

I Fundamentals of the high-order methods **9**

2 The Discontinuous Galerkin Spectral Element Method (DGSEM) **11**

2.1 Introduction 11

2.2 General formulation 12

2.3 Elemental discretisation 15

2.4 Discrete equations 18

2.5 Numerical Fluxes 21

2.6 Time discretisation 22

II Introduction stabilisation techniques for under-resolved Navier–Stokes equations **25**

3 Explicit and Implicit Large Eddy Simulations **27**

3.1 Introduction 27

3.2 General LES formulations 29

3.3 Implicit LES for DGSEM 31

3.4 Numerical results 32

3.5 Summary 39

4 Jump Penalty Method **41**

4.1 Introduction 41

4.2 Background: Jump Penalty 42

4.3 Numerical results 45

4.4 Summary 52

III Aeroacoustic methods **53**

5 Direct Noise Computation for Airfoils **55**

5.1 Introduction 55

5.2 Under resolved turbulent airfoil 56

5.3 Fully resolved 2.5D airfoil 64

5.4 Summary 67

6 Aeroacoustic Analogies **69**

6.1 Introduction 69

6.2 The Ffowcs-Williams and Hawkings analogy 71

6.3 Validation 74

6.4 Airfoil acoustic computation 79

6.5 Summary 83

7 Amiet's Model for Leading and Trailing Edge **85**

7.1 Introduction 85

7.2 The Amiet model for leading edge noise 86

7.3 The Amiet model for trailing edge noise 87

7.4 Wall pressure spectra models 88

7.5 Numerical results 91

7.6 Summary 93

IV Wind turbine modelling **95**

8 Wind Turbine Modelling **97**

8.1 Introduction 97

8.2 The Actuator Line Model 99
8.3 AL in DGSEM 102
8.4 Numerical results 104
8.5 Summary 122

9 Coupling for Wind Turbine Acoustic **125**
9.1 Introduction 125
9.2 The Strip Theory 127
9.3 AL coupling 129
9.4 Numerical results 130
9.5 Summary 136

Conclusions **137**

Appendices **141**

The Governing Equations **143**
.1 Navier-Stokes equations 143

Bibliography **145**

List of Figures

1.1 Diferent length scales involved in wind turbine simulations. [131]. 3

3.1 Velocity profiles of the turbulent channel at $Re_\tau = 950$ comparison for different LES and iLES techniques. DNS results are from [75, 100] 34

3.2 Computational domain and airfoil. Dimensions are defined in terms of chord units (C). 35

3.3 h/p mesh: red lines show coarse h-mesh and black lines the polynomial order 3 (4th order accuracy) mesh using Gauss nodes. left) mesh near the airfoil; right) zoom at the trailing edge zone. 36

3.4 Velocity contour and velocity vectors and the mid-span plane for the iLES Pirozzoli case. 37

3.5 Velocity vectors in region x/C from 0.4 to 0.6: (a) LES with WALE SGS model, (b) LES with VREMAN SGS model, (c) iLES with Pirozzoli flux, and (d) iLES with KG flux. 37

3.6 Isocontours of the Q-criterion, coloured by the velocity magnitude. (a) LES with WALE SGS model, (b) LES with VREMAN SGS model, (c) iLES with Pirozzoli flux, and (d) iLES with KG flux. 38

3.7 Streamwise velocity profiles of the mean flow in the normal direction. 39

4.1 Taylor Green vortex: Q-criterion for Re =1600 at different times t/t_c =7, 10 and 13. 46

4.2 Taylor Green vortex: Evolution of the kinetic energy dissipation rate in time of the TGV for several penalty parameters compared with DNS results [171]. a) Solution Jump. b) Gradient Jump. 47

4.3 Taylor Green vortex: Kinetic energy spectra at $t/t_c = 8$ for several penalty parameters. a) Solution Jump. b) Gradient Jump. 48

4.4 Taylor Green vortex: Comparison with of jump penalty strategy with traditional LES SGS model. a) Energy dissipation rate. b) Energy spectra at $t/t_c = 8$. 49

4.5 Kelvin-Helmholtz Instability: density for $\mathrm{Re} = 10^4$ at different times t/t_c =3, 6 and 9. Top row, well resolved case, 128^2 elements with $p = 5$. Bottom row, coarse unresolved case, 64^2 elements with $p = 3$, stabilized with solution jump penalty of $\tau_s = 0.01$ 50

4.6 Kelvin-Helmholtz Instability: Evolution of the mean mathematical Entropy with and without jump penalty stabilisation. 51

4.7 Kelvin-Helmholtz Instability: Evolution of mean a) Kinetic energy b) Enstrophy with and without jump penalty stabilisation. 51

5.1 h/p meshes: left) mesh 1: red lines show coarse h-mesh and black lines the p=5 mesh and right) mesh 2: finer h-mesh in red and the p-mesh with p=2 in black. 59

5.2 Topology of the computational domain and acoustic receiver locations. The lengths are not dimensionalized by the airfoil chord. 60

5.3 Effect of numerical tripping: Fourier transform of wall pressure near the trailing edge, the amplitude is nondimensionalized by the highest peak amplitude. 61

5.4 Instantaneous isosurface of lambda-2 criterion for refined mesh (mesh 2) with p=5. 61

5.5 Effect of the trip amplitude for the microphone array SPL for the coarse mesh (mesh 1). The SPL is subtracted by the lowest value. 62

5.6 Mesh convergence for microphone array SPL, natural transition configuration. The SPL is subtracted by the lowest value. 63

5.7 Mesh convergence for microphone array SPL, tripped configuration. The SPL is subtracted by the lowest value. 63

5.8 Instantaneous dilation field for refined mesh (mesh 2) with p=5. 64

5.9 Detail of mesh used for the NACA0012 simulation. a) h-mesh near the airfoil. b) h/p mesh near the trailing-edge, red lines show h-mesh and black lines the p=5 mesh 65

5.10 Instantaneous flow variables for p=5. a) Vorticity. b) Dilation field 66

5.11 Velocity profile at the wake for all polynomial orders at $x/C = 1.1$. a) Mean streamwise velocity. b) Fluctuations of the streamwise velocity. 66

5.12 Polynomial convergence of the PSD of the acoustic pressure of a point located in $[x, y]/C = [0.5, 0.5]$. 67

5.13 Polynomial convergence of the OSPL directivity (in dB) at $r = 2C$ calculated with direct computation. 68

6.1 Diferent categories and regions of aeroacoustics and their scales [9]. 70

6.2 Comparison between analytical and FWH acoustic pressure of the stationary monopole in a moving medium [108] with $\mathbf{M} = [0.5, 0, 0]^T$. a) Time history of the pressure at $[-20\ell, 0, 0]^T$. b) RMS of the pressure at $r = 20\ell$. 76

6.3 Comparison between analytical and FWH acoustic pressure of the stationary monopole in a moving medium [108] with $\mathbf{M} = [0.5, 0.5, 0.5]^T$. a) Time history of the pressure at $[-20\ell, 0, 0]^T$. b) RMS of the pressure at $r = 20\ell$. . . 77

6.4 Zoom of the h-mesh used to simulate the cylinder. 78

6.5 Results of NS simulation of flow over a cylinder at $\mathrm{Re} = 200$ and $M_0 = 0.2$. . . 78

6.6 Time averaged coefficients on the cylinder wall. Current results compared to the reference values of [33, 132]. 79

6.7 Directivity of the SPL (in dB) at $r = 20D$ for the flow over a cylinder obtained with the FWH acoustic analogy. Results compared with reference values of [33, 146]. 80

6.8 Polynomial convergence of the PSD of the acoustic pressure of a point located in $[x, y]/C = [0.5, 0.5]$ calculated with the FWH analogy. 81

6.9 Polynomial convergence of the OSPL directivity (in dB) at $r = 2C$ calculated with the FWH analogy. 82

6.10 82

6.11 Comparison of the PSD of the acoustic pressure of a point located in $[x, y]/C = [0.5, 0.5]$ calculated with the direct and the FWH analogy. 82

6.12 Comparison of the OSPL directivity (in dB) at $r = 2C$ calculated with the direct and the FWH analogy. 83

6.13 Polynomial convergence of the OSPL of a point located in $[x, y]/C = [0.5, 0.5]$ calculated with both, direct and the FWH analogy. 83

7.1 Far field noise comparison between current methodology, RANS simulations (from [98]) and experimental measurements (from [72]) for a NACA0012. SPL presented in 1/3 octave band. 92

8.1 Reference frame 100

8.2 Cross-sectional blade section showing velocities and forces on the airfoil. . . . 101

8.3 Schematic of the actuator point in a cell with its correspondent Gauss nodes, employing p=2. 103

8.4 Axial and tangential non-dimensional forces along the blade based on polynomial order. '—' AL1, '- -' AL2. 108

8.5 Axial and tangential forces along the blade, $\epsilon_{2.75}$. '—' AL1, '- -' AL2. 109

8.6 Velocity decay along the blade based on ϵ for different polynomial orders. '—' AL1, '- -' AL2. 110

8.7 Section of the instantaneous velocity field along the x-axis for $\epsilon_{2.75}$, a) $p = 2$, b) $p = 3$, c) $p = 4$ and d) $p = 5$ using AL1 method. 111

8.8 Detail of the near wake flow structures visualized using Q-criterion isosurfaces based on the polynomial order colored by u velocity for $\epsilon_{2.75}$ a) AL1 $p = 2$, b) AL2 $p = 2$, c) AL1 $p = 3$, d) AL2 $p = 3$, e) AL1 $p = 4$, f) AL2 $p = 4$, g) AL1 $p = 5$ and h) AL2 $p = 5$. 112

8.9 Segments in which the velocity decay, a, is represented. 113

8.10 Velocity decay, a, for different polynomial order based on ϵ, $x/D = 1$. '—' AL1, '- -' AL2 ', ■' Experimental data. 114

8.11 Velocity decay, a, for $\epsilon_{2.75}$ based on p, $x/D = 1$. '—' AL1, '- -' AL2', ■' Experimental data. 115

8.12 Velocity decay, a, for different polynomial order and ϵ parameter, $x/D = 3$. '—' AL1, '- -' AL2', ■' Experimental data. 116

8.13 Velocity decay, a, for different polynomial order and ϵ parameter, $x/D = 5$. '—' AL1, '- -' AL2', ■' Experimental data. 117

8.14 Velocity decay, a, for different polynomial order with $\epsilon_{2.75}$. a) & b) for $x/D = 3$; c) & d) for $x/D = 5$. '—' AL1, '- -' AL2', ■' Experimental data. 118

8.15 Turbulent kinetic energy at $x/D = 1$ (left), $x/D = 3$ (right) and $x/D = 5$ (below) for different polynomial order with $\epsilon_{2.75}$. '—' AL1, '- -' AL2', ■' Experimental data. 119

8.16 Velocity decay, a, with a $p = 2$ h-mesh with and without tower and nacelle implementation. '—' AL1', ■ 'Experimental data. 120

8.17 Section of the instantaneous velocity field along the y-axis with the Q-criterion isosurfaces for $\epsilon_{2.75}$ a) Actuator line without tower and nacelle. b) Actuator line with tower and nacelle, modelled using immersed boundaries. 121

8.18 Simulation time for AL1 (averaging) and AL2 (projection): 100 Iterations simulation time for polynomial orders ranging from 2 to 6. 122

9.1 Lateral view of the h-mesh. 132

9.2 Iso-countours of the Q-criteria and vertical slice of the magnitude of the velocity for the AL simulation at O.C. 1. The tower and nacelle are included for visualization purposes only. 132

9.3 Comparison of apparent velocity and angle of attack distribution along the blade between actuator line averaged over one rotation and BEMT simulations. 133

9.4 Comparison of the wind turbine noise prediction in one-third octave for several operational conditions. 134

9.5 OASPL of each blade using over one rotation. O.C. 1 135

List of Tables

7.1 Comparison of the overall sound pressure level in the frequency range from 1000 to 6300 Hz. Values are presented in dB. (LWT: Laminar Wind Tunnel; AWB: Braunschweig Aeroacoustic Wind Tunnel) 92

8.1 Values of the projection parameter, ϵ, based on the polynomial order. 105

8.2 Averaged velocity method: C_P and C_T based on the polynomial order and ϵ. . 106

8.3 Weighted sums method: C_P and C_T based on the polynomial order and ϵ. . . 107

9.1 Operational conditions of the wind turbine. 131

Abbreviations

Acronyms

AL	Actuator Line
APE	Acoustic Perturbation Equation
BEMT	Blade Element Momentum Theory
BR	Bassi and Rebay
CAA	Computational Aeroacoustic
CFD	Computational Fluid Dynamics
DG	Discontinuous Galerkin
DGSEM	Discontinuous Galerkin Spectral Element Method
DNC	Direct Noise Calculation
DNS	Direct Numerical Simulation
FD	Finite Difference
FE	Finite Element
FV	Finite Volume
FWH	Ffowcs-Williams and Hawkings
GL	Gauss-Lobatto
HO	High-Order
HORSES3D	High-Order Spectral Element Solver
HPC	High performance computing
iLES	Implicit Large Eddy Simulation
KHI	Kelvin-Helmholtz Instability
LEE	Linearized Euler Equations
LE	Leading-Edge
LES	Large Eddy Simulation
NS	Navier-Stokes
SGS	Sub-grid Scale
SIP	Symmetrical Interior Penalty
TE	Trailing-Edge
TGV	Taylor-Green Vortex
TSR	Tip Speed Ratio

Chapter 1

Introduction

Contents

1.1 Motivation **1**

1.2 Objectives and Methodology **3**

1.3 Outline **5**

1.4 Contributions & Highlights **6**

1.4.1 List of Publications 6

1.5 Notation **8**

1.1 Motivation

Wind turbines play an important role in decreasing the use of fossil fuels in favour of renewable energies. However, one of the main environmental concerns regarding the deployment of wind turbines is the noise produced by its operation. In fact, aeroacoustic emissions have been categorised as an annoying factor [129] and are associated with potentially damaging physical and psychological effects on humans and wild animals [1, 70, 99]. Regulations have been tightened in several countries to limit the noise of wind turbines [40, 90, 125]. This creates limitations to the wider exploitation of wind energy resources, especially in the integration of turbines in urban environments, where noise nuisances can be of great concern [77, 136]. For these reasons, accurate prediction of wind turbine noise is of

paramount importance for the design of new and quieter wind turbines.

One of the main tools for accurately predicting wind turbine noise is the use of Computational Aeroacoustic (CAA), where the generation and propagation of noise produced by aerodynamic flows are studied using computer-based simulations. It can be categorised as a subset of a more general technique, known as Computational Fluid Dynamics (CFD), that solves partial differential equations (PDEs) that govern the physics of fluids by approximating the solution using numerical methods.

There have been a enormous advance in CFD software, making it one of the most widely used tools for industry design. However, industrial CFD software mostly relies on low-order methods, being finite volumes tho most popular one. In addition, it is used along with simple turbulence models, such as the Rynolds Average Navier–Stokes (RANS) model, rather than resolving the turbulence small scales. This is a powerful tool for aerodynamic design, but not reliable enough for aeroacoustic simulations, since it is by physical definition a time dependent problem. In this scenario, using a Large Eddy Simulation (LES) approach can be a good option, since it has a good resolution of space and time.

Since CAA simulations require high accuracy to predict generated noise, numerical models should be, by necessity, very accurate. Traditional, low-order numerical techniques such as finite volumes methods suffer from non-negligible numerical errors (i.e. dissipative and dispersive errors) that can increase nonphysical dissipation and dispersion of flow structures or acoustic waves and provide unrealistic results. The alternative is to use high-order techniques, which are characterised by low numerical errors [27] and their ability to use mesh refinement (increased number of mesh nodes or h-refinement) and/or polynomial enrichment (p-refinement) to achieve highly accurate solutions [88, 89, 140]. High-order methods provide exponential decay of the error for smooth solutions instead of the algebraic decay provided by low-order techniques.

High order methods have been extensively used in computational fluid dynamics due to their accuracy and efficiency in the simulation of fluid flows. This type of discretisation scheme shows lower diffusion and dissipative errors and higher numerical accuracy for the same number of degrees of freedom compared to standard low-order schemes [28, 83, 92]. This characteristic makes them better suited for

problems where high accuracy is required.

1.2 Objectives and Methodology

Simulating wind turbines includes many different physical processes, which take place at different length and time scales. It can go from the very small details of turbulence developing in the airfoil of a blade section, passing to the tip vertices produced by the rotation of the blades, to the atmospheric flows that include thousands of kilometres. Figure 1.1 summarises these scales and points out the most important ones: airfoil scale, wind turbine scale, farm scale and macroscale.

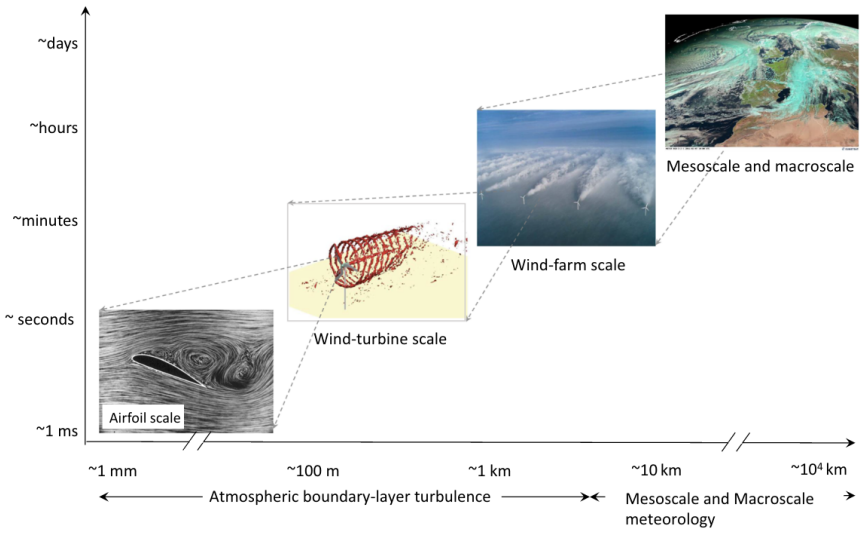


Figure 1.1: Diferent length scales involved in wind turbine simulations. [131].

Resolving all these different scales in one single simulation is not possible with the technology currently available, due to its huge computational cost. This is why we generally focus on one scale and use simple models for the others, including its effects. We will develop a similar approach, focussing on two levels separately: the first one is the airfoil scale while the second one is the wind turbine scale, with the potential to extend it to farm scale.

The airfoil scale is of paramount importance, because it is here where the noise generation occurs. Complex phenomena, such as turbulence, need to be taken into account, which creates special requirements such as fine time and space resolution,

along with high precision. High–order methods are very good candidates for this scenario.

The wind turbine scale is also studied as the main aerodynamic variables, such as the power produced by the turbine, need at least to contemplate one whole wind turbine. Here other physical phenomena are taken into account, such as the rotation of the blades and the wake produced by them. While one can perform a detailed simulation of a single rotating blade, it will not be possible to scale it to the wind farm level. However, by coupling wind turbine models with flow solvers, this extension is natural. This is important as the propagation of noise is most relevant in these two scales, thus being able to approach both of them with the same methodology is desirable.

For these reasons, in this thesis, we aim to develop computational tools using advance numerical methods based on high–order, and particularly the Discontinuous Galerkin Spectral Element Method. The main applications are related to the simulation of the aerodynamic and aeroacoustic of wind turbines and airfoils in a LES framework.

As the general objective includes many aspects, we can divide it into more specific ones:

- Research in the fundamentals of CFD high-order simulations, with the aim of obtaining schemes that are robust at affordable cost.
- Study advanced methods for simulating turbulent problems, including underresolved scenarios and the interaction of the numerical methods with turbulent models.
- Develop numerical methods for computing the aeroacoustic of airfoils with high precision.
- Investigate the effect of polynomial refinement in the prediction of aerodynamics and aeroacoustics of airfoils.
- Develop efficient numerical methods suitable for LES simulations of wind turbines using high-order methods.
- Study the parameters of simulation of wind turbines using high–order methods.

- Elaborate a methodology that can be used to compute the aeroacoustic of a whole wind turbine.

In this way, we can tackle the problem of simulating the aerodynamic and aeroacoustic of wind turbines from a top-and-bottom approach, with the goal of advancing toward combining both in future work.

1.3 Outline

The remaining chapters of this thesis are separated in four parts:

- Part I provides the general concepts of the numerical methods used in the thesis. Mainly, we present the spatial discretisation formulation called Discontinuous Galerkin Spectral Element Method (DGSEM), with emphasis on solving conservation laws. We provide details on inviscid and viscous discretisation, and handling complex geometries using curvilinear mapping.
- Part II is focused on the fundamentals of turbulent simulations, validating different strategies for dealing with under-resolved simulations using DGSEM. In Chapter 3 we introduce the Large Eddy Simulation method as a first approach to stabilise the numerical simulation, and we compare it to more numerically advanced methods that do it implicitly. Chapter 4 keeps this latter approach further, using the jump penalty method to handle very challenging cases.
- Part III deals with the computation of aeroacoustics of airfoils, going from high-fidelity simulations to low-fidelity models. Chapter 5 introduces aeroacoustic simulations by solving together the flow and acoustic field directly using the compressible Navier-Stokes equations with good refinement. In Chapter 6 we separate generation from sound propagation using the Ffowcs-Williams and Hawkings aeroacoustics analogy. Chapter 7 presents the Amiet's theory, a semi-analytical approach to compute noise generation and propagation, along with the whole procedure that enables it to be used in airfoil noise.
- Part IV presents the methodology that enables wind turbine simulations, using DGSEM. In Chapter 8 we introduce the Actuator Line method,as the wind turbine model that is used to represent the motion of the turbine blades, focussing on the solution of the wake and the aerodynamics. In Chapter 9 we use the Actuator Line and Amiet's theory to provide a methodology that can compute aeroacoustics of the whole turbine.

1.4 Contributions & Highlights

The main contributions that can be highlighted in this work are:

- Comparison of LES and iLES approaches for different kinds of turbulent simulations in high order schemes. Both, h-mesh and polynomial refinement are studied for each method in standard and complex cases, where the standard DGSEM formulation is not able to provide a solution due to numerical divergence.

- Performing aeroacoustic predictions of airfoils using methodologies of different fidelities, ranging from very good resolved CFD, to aeroacoustic analogies, to semi-analytical models. For the first two, the DGSEM discretisation is used and the influence of the polynomial on noise generation and propagation is studied.

- Two different implementations of the Actuator Line model in the DGSEM solver, one that uses the arithmetical average and another a Gaussian weighted average. For both methodologies, polynomial refinement is studied, finding the advantages and disadvantages of each.

- Coupling CFD Actuator Line simulations with semi-analytical model to provide a methodology that can be used to predict the noise of a wind turbine. The Amiet's and strip theory are used as a post-process tool that uses both, the time-averaged and instantaneous CFD results.

- Contribute to the development of the CFD solver, HORSES3D [58] (High Order Spectral Element Method Solver), focusing on the solution of the compressible Navier–Stokes in 3D problems. Aeroacoustic integration, pre- and post-process features, and wind turbine models can be highlighted as the main contributions.

1.4.1 List of Publications

Parts of this thesis have been published in peer-reviewed journals and in international conferences:

Journal Publications

- Kou, J., **Marino, O.A.**, Ferrer E. Jump penalty stabilization techniques for under-resolved turbulence in discontinuous Galerkin schemes. Journal of Computational Physics, 491, 112399 (2023).

- Kou, J., Botero-Bolívar, L., Ballano, R., **Marino, O.**, de Santana, L., Valero, E., Ferrer E. Aeroacoustic airfoil shape optimization enhanced by autoencoders. Expert Systems with Applications, 217, 119513 (2023).

- Otmani, K-E., Ntoukas, G., **Mariño, O.A.**, Ferrer, E. Toward a robust detection of viscous and turbulent flow regions using unsupervised machine learning. Physics of Fluids 35, 027112 (2023).

- Ferrer E, Rubio G, Ntoukas G, Laskowski W, **Mariño, OA**, Colombo S, Mateo-Gabín A, de Lara FM, Huergo D, Manzanero J, Rueda-Ramírez AM. HORSES3D: a high-order discontinuous Galerkin solver for flow simulations and multi-physics applications.Computer Physics Communications, 287, 108700 (2023).

International Conferences

- **Marino, O.A.**; Errasti, J.; Ferrer E.; Valero E. "EXPLICIT AND IMPLICIT LARGE EDDY SIMULATION FOR A NACA0012 USING A HIGH ORDER DISCONTINUOUS GALERKIN SOLVE". ECCOMAS 2022. Oslo, Norway.

- **Marino, O.A.**; Ferret, O.; Ferrer E.; Valero E. "Aeroacoustic simulations of 3D airfoil sections using a high order discontinuous Galerkin solver". Aiaa Science And Technology Forum And Exposition, Aiaa Scitech Forum 2022, San Diego, USA.

- Ferrer, E.; Manzanero, J.; Rueda-Ramírez, A. M.; Laskowski, W.; Ntoukas G; **Marino, O.**; Rubio, G.; Kopriva, D.; Valero, E. "HORSES3D: A high order discontinuous Galerkin for flow simulations and multiphysics applications". ICOSAHOM 2020. Vienna, Austria.

Moreover, following papers are currently under review:

- Botero-Bolívar, L., **Marino, O.**, Venner, C., de Santana, L., Valero, E., Ferrer E. Low-cost wind turbine aeroacoustic predictions using actuator lines.

1.5 Notation

Throughout this thesis, we indicate generic vectors and matrices by small bold letters $\mathbf{q}$ for the former and capital bold letters $\mathbf{A}$ for the latter. In addition, inner product is denoted as $\langle \cdot, \cdot \rangle$.

The states of the face of an element are represented as $\mathbf{q}^+$ and $\mathbf{q}^-$ to be the values on the right and left interfaces, respectively.

Part I
Fundamentals of the high-order methods

Summary In the first part, we introduce the discretisation method that is used throughout the thesis, the Discontinuous Galerkin Spectral Element Method (DGSEM). We start by providing the derivation of the DGSEM general formulation, adding important details such as numerical fluxes and curve geometries, obtaining a formulation that can be used in a general 3D case.

Chapter 2

The Discontinuous Galerkin Spectral Element Method (DGSEM)

Contents

2.1 Introduction 11
2.2 General formulation 12
2.2.1 Polynomial approximation 13
2.2.2 Quadratures 14
2.3 Elemental discretisation 15
2.3.1 Metric tensors 16
2.4 Discrete equations 18
2.5 Numerical Fluxes 21
2.6 Time discretisation 22

2.1 Introduction

In this chapter we present the mathematical details of the high-order DG formulation, obtaining a discretisation of conservative laws for general geometries. In Section 2.2 we introduce the DG discretisation starting from the continuous equations, and how it is transformed into a spectral method in a reference space. Then, in Section 2.3 we deal with the discretisation of the physical space for general geometries and the relations between the physical and reference space. Section 2.4 develops

the formulation that ends in a complete set of discrete equations. Section 2.5 gives important details of the communication between elements and some methods to handle the discontinuity between them. Finally, in Section 2.6 we overview time marching methods, such that we can solve time evolving problems.

2.2 General formulation

We start with the system of equations of a general problem that can be written in conservative form as:

$$\mathbf{q}_t + \nabla \cdot \mathbf{f} = \mathbf{s}, \text{ in } \Omega, \tag{2.1}$$

where $\mathbf{q}$ is the state vector of conserved variables, of length N_{cons}, $\mathbf{f}$ is the flux vector, $\mathbf{s}$ is a source term, and Ω is the domain of the problem. Although (2.1) represents a general problem, in this thesis we work specifically with the compressible Navier–Stokes equations, which are presented in more detail in Section .1. In addition, in general form, the domain can be a subset of a N_d dimension space; however, we will restrict our problem to be $\Omega \in \mathbb{R}^3$. To derive the Discontinuous Galerkin (DG) formulation, we first obtain the weak form, multiplying (2.1) by an arbitrary continuous and smooth test function $\mathbf{v}$ and integrate over the whole domain:

$$\int_\Omega \mathbf{q}_t \cdot \mathbf{v} \, d\Omega + \int_\Omega \nabla \cdot \mathbf{f} \cdot \mathbf{v} \, d\Omega = \int_\Omega \mathbf{s} \cdot \mathbf{v} \, d\Omega, \tag{2.2}$$

and then integrating by parts, that in the more general 3D case is applying the Gauss law,

$$\int_\Omega \mathbf{q}_t \cdot \mathbf{v} \, d\Omega + \int_{\partial\Omega} (\mathbf{f} \cdot \mathbf{n}) \mathbf{v} \, dS - \int_\Omega \mathbf{f} \cdot \nabla \mathbf{v} \, d\Omega = \int_\Omega \mathbf{s} \cdot \mathbf{v} \, d\Omega, \tag{2.3}$$

where $\partial\Omega$ is the boundary of the domain and $\mathbf{n}$ is its normal unit vector. To obtain the complete DGSEM derivation, we will first introduce some approximations and definitions.

2.2.1 Polynomial approximation

The Discontinuous Galerkin establishes that the variables of interest can be approximated by a continuous polynomial function of arbitrary order N. In our case, we approximate $\mathbf{q}$, $\mathbf{f}$, $\mathbf{s}$ and $\mathbf{v}$ by $\mathbf{q}^N$, $\mathbf{f}^N$, $\mathbf{s}^N$ and $\mathbf{v}^N$, each of them belonging to the space of L^2 functions $\mathcal{V} = \{\mathbf{v} \in L^2(\Omega),\ \forall i \in [1,...,K],\ \mathbf{v}|_\Omega \in \mathscr{P}^N\}$, being $\mathscr{P}^N$ the space of polynomials of degrees at most N. Therefore, we can express its function as a linear combination of basis functions $\phi_n \in \mathscr{P}^N$:

$$\mathbf{q}(\mathbf{x}) \approx \mathbf{q}^N(\mathbf{x}) = \sum_{n=1}^{\text{NDOF}} \mathbf{q}_n^N \phi_n(\mathbf{x}), \tag{2.4}$$

where $\mathbf{q}_n^N$ are the coefficients of the polynomial expansion, and NDOF is the number of degrees of freedom of the approximation,

$$\text{NDOF} = \prod_{i=1}^{N_d=3} (N_i + 1). \tag{2.5}$$

Three important remarks must now be highlighted. First is that in the Galerkin formulation, the test function $\mathbf{v}$ is approximated using the same basis functions as for the solution $\mathbf{q}$, and in the current work, it is also for the fluxes and the source term. Second, the polynomial expansion of (2.4) is usually performed in a reference space where the domain is in $[-1,1]^3$, using the correspondent reference coordinate $\boldsymbol{\xi} = [\xi, \eta, \zeta]^T$ instead of the physical coordinate $\mathbf{x}$. More details of the mapping between both for general geometries are presented in Section 2.3. Third, the DGSEM formulation is a nodal form of the DG discretisation, where the basis functions ϕ_n are defined as the tensor product of 1D Lagrange polynomials of order N,

$$\mathbf{q}^N(\boldsymbol{\xi}) = \sum_{n=1}^{\text{NDOF}} \mathbf{q}_n^N \phi_n(\boldsymbol{\xi}) = \sum_{i=0}^{N_1} \sum_{j=0}^{N_2} \sum_{k=0}^{N_3} \mathbf{q}_{i,j,k}^N \ell_i(\xi) \ell_j(\eta) \ell_k(\zeta), \tag{2.6}$$

where ℓ_i are the Lagrange polynomials, defined as,

$$\ell_i(\xi) = \prod_{\substack{j=0 \\ j \neq i}}^{N} \frac{\xi - \xi_j}{\xi_j - \xi_i}. \tag{2.7}$$

Lagrange polynomials are discretely orthogonal in the interval $\xi \in [-1, 1]$:

$$\ell_i\left(\xi_j\right) = \delta_{ij}, \tag{2.8}$$

where δ_{ij} the Kronecker delta. This leads to one of the main characteristics of the formulation, the solution at the position of each of the NDOF node points is the nodal value of the polynomial approximation on them,

$$\mathbf{q}\left(\mathbf{x}\left(\boldsymbol{\xi}_{i,j,k}\right)\right) \approx \mathbf{q}^N\left(\boldsymbol{\xi}_{i,j,k}\right) = \mathbf{q}^N_{i,j,k} = \mathbf{q}^N_n. \tag{2.9}$$

2.2.2 Quadratures

As (2.3) involves integrals of polynomial expansions, we use of the Gauss quadrature rule of order N to approximate them numerically, due to its high precision. It is defined in 1D as,

$$\int_\xi f \,\mathrm{d}\xi = \int_{-1}^{1} f \,\mathrm{d}\xi \approx \sum_{i=0}^{N} f(\xi_i)\mathrm{w}_i, \tag{2.10}$$

where w_i are the weights at each quadrature node ξ_i. To extend in to 3D we use the tensor product definition,

$$\int_{-1}^{1}\int_{-1}^{1}\int_{-1}^{1} f \,\mathrm{d}\xi \,\mathrm{d}\eta \,\mathrm{d}\zeta \approx \sum_{i=0}^{N_1}\sum_{j=0}^{N_2}\sum_{k=0}^{N_3} \mathrm{w}_i\mathrm{w}_j\mathrm{w}_k f\left(\xi_i, \eta_j, \zeta_k\right). \tag{2.11}$$

When (2.11) is applied to the product of a functions that can be approximated by the polynomial expansion of (2.6) , i.e. the inner product of them in the reference space E, we obtain,

$$\left\langle \mathbf{q}^N, \mathbf{v}^N \right\rangle_E = \int_{-1}^{1}\int_{-1}^{1}\int_{-1}^{1} \mathbf{q}^N \cdot \mathbf{v}^N \,\mathrm{d}\xi \,\mathrm{d}\eta \,\mathrm{d}\zeta = \sum_{i=0}^{N_1}\sum_{j=0}^{N_2}\sum_{k=0}^{N_3} \mathrm{w}_i\mathrm{w}_j\mathrm{w}_k \mathbf{q}^N_{i,j,k}\mathbf{v}^N_{i,j,k}, \tag{2.12}$$

and if one of the functions corresponds to the basis functions of the expansion, ϕ_{ijk}, it can be further simplified using the orthogonal property (2.8),

$$\left\langle \mathbf{q}^N, \phi_{ijk} \right\rangle_E = \int_{-1}^{1}\int_{-1}^{1}\int_{-1}^{1} \mathbf{q}^N \ell_i(\xi)\ell_j(\eta)\ell_k(\zeta)\,\mathrm{d}\xi\,\mathrm{d}\eta\,\mathrm{d}\zeta = \mathrm{w}_i\mathrm{w}_j\mathrm{w}_k\mathbf{q}^N_{i,j,k}. \tag{2.13}$$

Another important aspect is to ensure that the set of collocation nodes $\boldsymbol{\xi}$ ensures an accurate numerical approximation of the integrals. The most common choices for the nodes of the quadrature rule are the Legendre-Gauss (also referred as just Gauss nodes) and the Legendre-Gauss-Lobatto [91] (also referred as just Gauss-Lobatto nodes or GL nodes). Both set of nodes have its own advantages and disadvantages. The latter includes the end points of the $[-1,1]$ interval, but the integration is exact up to the order $2N-1$, while the former does not include the end points (thus interpolating is necessary if the value at this locations is needed), although it has a higher precision, up to $2N+1$ [91]. In this way, for both the integral quadrature and the polynomial expansions, we use the Lagrange interpolating polynomials evaluated on the Gauss or GL nodes.

In addition, (2.3) includes the gradient of the test function $\mathbf{v}$, which is approximated using the polynomial expansion. Therefore, it is natural to approximate the spatial derivative of the function as the derivative of the Lagrange polynomials at the location of the node. For a generic function f^N, the partial derivative with respect to the coordinate ξ at the node $_{i,j,k}$, taking into account the property (2.8) is expressed as,

$$\frac{\partial f^N_{ijk}}{\partial \xi} = \sum_{m=0}^{N} f^N_{mjk}\ell'_m(\xi_i)\ell_j\left(\eta_j\right)\ell_k(\zeta_k) = \sum_{m=0}^{N} f^N_{mjk}\ell'_m(\xi_i) = \sum_{m=0}^{N} D_{im}f^N_{mjk}, \tag{2.14}$$

where $D_{ij} = \ell'_i\left(\xi_j\right)$ is a matrix whose entries are the derivatives of the Lagrange polynomials at the nodes, called the derivative matrix.

2.3 Elemental discretisation

In the DGSEM formulation, we combine the spectral discretisation of the solution using polynomial expansion with the classical discretisation of the physical space, as for example for FV. We start by approximating the domain Ω by a tessellation $\mathscr{T} = \{e\}$ of non-overlapping hexahedral elements e. Each element has a domain Ω^e and a boundary $\partial\Omega^e$. We rewrite (2.3) for each element instead of the whole domain

and replace the variables by its polynomial approximation as defined in (2.4),

$$\int_{\Omega^e} \mathbf{q}_t^{eN} \cdot \mathbf{v}^{eN} \, \mathrm{d}\Omega^e + \int_{\partial\Omega^e} \left(\mathbf{f}^{eN} \cdot \mathbf{n}\right) \mathbf{v}^{eN} \, \mathrm{d}S - \int_{\Omega^e} \mathbf{f}^{eN} \cdot \nabla \mathbf{v}^{eN} \, \mathrm{d}\Omega^e = \int_{\Omega^e} \mathbf{s}^{eN} \cdot \mathbf{v}^{eN} \, \mathrm{d}\Omega^e, \quad (2.15)$$

where the superindex e refers to the functions evaluated inside the element e. This way, the solution of each element is approximated as a continuous polynomial, but can be discontinuous at the interfaces of two elements.

In addition, in Section 2.2.1 we stated that the polynomial expansion and quadrature rules are usually performed in a reference coordinate system ξ rather than the physical one $\mathbf{x}$. We now address the relations between each other that are used for the DGSEM formulation. The physical space Ω^e of a generic element e is transformed into a reference cubic element E of domain $\Omega^E = [-1, 1]^3$ with the reference spatial coordinates ξ^e by transfinite mapping $\boldsymbol{\chi}^e$:

$$\boldsymbol{\chi}^e : \xi^e \rightarrow \mathbf{x}^e. \quad (2.16)$$

Note that the tessellation of the domain does not have the restriction of being homogeneous; thus, each element can have different characteristics such as size or rotation, that creates an individual mapping per element. In addition, for general geometries, linear elements might not be sufficient to approximate it, therefore it is characteristic of high-order methods to use curvilinear elements. For these kinds of elements, the mapping $\boldsymbol{\chi}^e$ is created by approximating the space using polynomials of order M,

$$\boldsymbol{\chi}^e \approx \boldsymbol{\chi}^e \in \mathscr{P}^M. \quad (2.17)$$

2.3.1 Metric tensors

We have seen in Section 2.2.1 and Section 2.2.2 how to approximate the solution, integrals and derivatives using polynomial expansion and quadratures in the reference space. However, (2.15) is based on derivatives operators in the physical space. To transform these operators in the reference space, we first need to define two crucial space vectors, also known as *metric tensors*. The first one is the *covariant* basis vector, $\mathbf{a}_i$, which represents the variation of the mapping along a coordinate

line [91] ξ^i, using Einstein notation for the index, i.e. $\boldsymbol{\xi} = [\xi, \eta, \zeta]^T = \left[\xi^1, \xi^2, \xi^3\right]^T$,

$$\mathbf{a}_i = \frac{\partial \boldsymbol{\chi}}{\partial \xi^i}, \tag{2.18}$$

and the *contravariant* basis vector $\mathbf{a}^i$, which is normal to the coordinate line and is defined by its gradients,

$$\mathbf{a}^i = \nabla \xi^i. \tag{2.19}$$

We can use the two vectors to define the determinant of the Jacobian of the transformation, J (sometimes just referred as the Jacobian),

$$J = \mathbf{a}_1 \cdot (\mathbf{a}_2 \times \mathbf{a}_3), \tag{2.20}$$

and the Jacobian itself to define the matrix $\mathscr{M}$ [93], a volume-weighted expanded version of the Jacobian matrix of the transformation, whose columns are composed by $J\mathbf{a}^i$,

$$\mathscr{M} = \begin{pmatrix} Ja_1^1 \underline{I}_{N_{cons}} & Ja_1^2 \underline{I}_{N_{cons}} & Ja_1^3 \underline{I}_{N_{cons}} \\ Ja_2^1 \underline{I}_{N_{cons}} & Ja_2^2 \underline{I}_{N_{cons}} & Ja_2^3 \underline{I}_{N_{cons}} \\ Ja_3^1 \underline{I}_{N_{cons}} & Ja_3^2 \underline{I}_{N_{cons}} & Ja_3^3 \underline{I}_{N_{cons}} \end{pmatrix}. \tag{2.21}$$

With these definitions, the gradient of a state vector $\mathbf{q}$ can be expressed as,

$$\nabla \mathbf{q} = \frac{1}{J} \mathscr{M}^T \nabla_\xi \mathbf{q}, \tag{2.22}$$

where $\nabla_\xi \mathbf{q}$ refers to the gradient of the vector with respect to the coordinates of the reference space. Likewise, the divergence of a flux $\mathbf{f}$ is calculated as,

$$\nabla \cdot \mathbf{f} = \frac{1}{J} \nabla_\xi \cdot \left(\mathscr{M}^T \mathbf{f}\right) = \frac{1}{J} \nabla_\xi \cdot \tilde{\mathbf{f}}, \tag{2.23}$$

where $\tilde{\mathbf{f}}$ is called the contravariant flux.

The integral using the quadratures defined in Section 2.2.2 can be transformed as,

$$\int_{\Omega^e} f \,\mathrm{d}x\,\mathrm{d}y\,\mathrm{d}z = \int_{\Omega^E} Jf \,\mathrm{d}\xi\,\mathrm{d}\eta\,\mathrm{d}\zeta = \sum_{i=0}^{N_1}\sum_{j=0}^{N_2}\sum_{k=0}^{N_3} \mathrm{w}_i \mathrm{w}_j \mathrm{w}_k J_{i,j,k} f_{i,j,k}, \tag{2.24}$$

and by extension, the inner product, of (2.13) as,

$$\left\langle \mathbf{q}^N, \phi_{ijk} \right\rangle_e = \left\langle J\mathbf{q}^N, \phi_{ijk} \right\rangle_E = J_{i,j,k} \mathrm{w}_i \mathrm{w}_j \mathrm{w}_k \mathbf{q}^N_{i,j,k}. \tag{2.25}$$

2.4 Discrete equations

In this section we are interested in deriving a complete set of discrete equations the compressible Navier–Stokes. For this, we recognized the flux block vector $\mathbf{f}$ in (2.1) as the difference of two individual terms based on the physical properties, the inviscid flux part $\mathbf{f}_a(\boldsymbol{q})$, related with the advective part of the NS equations, and the viscous flux part $\mathbf{f}_v(\mathbf{q}, \nabla\mathbf{q})$, that depends on the viscosity of the fluid, the state vector and its gradients. We introduce this definition in (2.1) to obtain,

$$\mathbf{q}_t + \nabla \cdot \mathbf{f}_a - \nabla \cdot \mathbf{f}_v = \mathbf{s}. \tag{2.26}$$

Since the viscous flux term in (2.26) depends on the second derivative of the state vector $\vec{q}$, for using the DGSEM discretisation, we need to rearrange it into a system of two first order equations. There are many options for these splitting, but we will use the *conservative gradient approach*, since we keep working with the conservative variables and provides a good flexibility. This way we defined the new variable, $\mathbf{g} = \nabla\mathbf{q}$ and rearrange (2.26) into two equations,

$$\begin{aligned} \mathbf{q}_t + \nabla \cdot \mathbf{f}_a(\mathbf{q}) - \nabla \cdot \mathbf{f}_v(\mathbf{q}, \mathbf{g}) &= \mathbf{s}, \\ \nabla\mathbf{q} &= \mathbf{g}. \end{aligned} \tag{2.27}$$

As we need to perform all the future operations in the reference space, we convert all the derivative operators from the physical space using the transformation for the gradient, (2.23) and the divergence (2.22),

$$\begin{aligned} \mathbf{q}_t + \frac{1}{J}\nabla_\xi \cdot \tilde{\mathbf{f}}_a - \frac{1}{J}\nabla_\xi \cdot \tilde{\mathbf{f}}_v = \mathbf{s}, \\ \frac{1}{J}\mathscr{M}^T \nabla_\xi \mathbf{q} = \mathbf{g}. \end{aligned} \tag{2.28}$$

We get the weak form following the same procedure as before, i.e. multiplying by a test function, integrating in one element e that is part of the domain, applying the Gauss law and then replacing by the polynomial approximation,

$$\begin{aligned} &\int_{\Omega^e} \mathbf{q}_t^{eN} \cdot \mathbf{v}^{eN} \,\mathrm{d}\Omega^e + \frac{1}{J}\int_{\partial\Omega^e} \left(\tilde{\mathbf{f}}_a^{eN} - \tilde{\mathbf{f}}_v^{eN}\right) \cdot \mathbf{n}\mathbf{v}^{eN} \,\mathrm{d}S - \frac{1}{J}\int_{\Omega^e} \left(\tilde{\mathbf{f}}_a^{eN} - \tilde{\mathbf{f}}_v^{eN}\right) \cdot \nabla_\xi \mathbf{v}^{eN} \,\mathrm{d}\Omega^e = \int_{\Omega^e} \mathbf{s}^{eN} \cdot \mathbf{v}^{eN} \,\mathrm{d}\Omega^e, \\ &\int_{\Omega^e} \mathbf{g}^{eN} \cdot \mathbf{v}^{eN} \,\mathrm{d}\Omega^e = \frac{1}{J}\int_{\partial\Omega^e} \mathbf{q}^{eN} \cdot \tilde{\mathbf{v}}^{eN}\mathbf{n} \,\mathrm{d}S - \frac{1}{J}\int_{\Omega^e} \mathbf{q}^{eN} \cdot \nabla_\xi \tilde{\mathbf{v}}^{eN} \,\mathrm{d}\Omega^e, \end{aligned} \tag{2.29}$$

where $\tilde{\mathbf{v}}^{eN} = \mathscr{M}^T \mathbf{v}^{eN}$ is the test function projected into the contravariant basis. Since (2.29) is valid for an arbitrary test function in polynomial expansion $\mathbf{v}^{eN}$, it must be valid also for one of its basis function ϕ_{ijk}^e, that is the tensor product of three individual Lagrange polynomials. Changing this and recognizing all the volume integrals as the inner product of two functions, we obtain,

$$\begin{aligned} &\left\langle \mathbf{q}_t^{eN}, \phi_{ijk}^e \right\rangle_e + \frac{1}{J}\int_{\partial\Omega^e} \left(\tilde{\mathbf{f}}_a^{eN} - \tilde{\mathbf{f}}_v^{eN}\right) \cdot \mathbf{n}\phi_{ijk}^e \,\mathrm{d}S - \frac{1}{J}\left\langle \tilde{\mathbf{f}}_a^{eN}, \nabla_\xi \phi_{ijk}^e \right\rangle_e + \frac{1}{J}\left\langle \tilde{\mathbf{f}}_v^{eN}, \nabla_\xi \phi_{ijk}^e \right\rangle_e = \left\langle \mathbf{s}^{eN}, \phi_{ijk}^e \right\rangle_e, \\ &\left\langle \mathbf{g}^{eN}, \phi_{ijk}^e \right\rangle_e = \frac{1}{J}\int_{\partial\Omega^e} \mathbf{q}^{eN} \tilde{\phi}_{ijk}^e \mathbf{n} \,\mathrm{d}S - \frac{1}{J}\left\langle \mathbf{q}^{eN}, \nabla_\xi \tilde{\phi}_{ijk}^e \right\rangle_e. \end{aligned} \tag{2.30}$$

We can observe that all the integrals and inner products of (2.30) are in the physical space. We change it from the physical space of the element e to its reference space E using all the definitions of Section 2.3.1, obtaining,

$$\begin{aligned}
&\left\langle J\mathbf{q}_t^{eN}, \phi_{ijk}^e \right\rangle_E + \int_{\partial\Omega^E} \left(\tilde{\mathbf{f}}_a^{eN} - \tilde{\mathbf{f}}_v^{eN}\right)\cdot\mathbf{n}\phi_{ijk}^e \,\mathrm{d}S - \left\langle \tilde{\mathbf{f}}_a^{eN}, \nabla_\xi \phi_{ijk}^e \right\rangle_E + \left\langle \tilde{\mathbf{f}}_v^{eN}, \nabla_\xi \phi_{ijk}^e \right\rangle_E = \left\langle J\mathbf{s}^{eN}, \phi_{ijk}^e \right\rangle_E, \\
&\left\langle J\mathbf{g}^{eN}, \phi_{ijk}^e \right\rangle_E = \int_{\partial\Omega^E} \mathbf{q}^{eN}\tilde{\phi}_{ijk}^e \mathbf{n}\,\mathrm{d}S - \left\langle \mathbf{q}^{eN}, \nabla_\xi \tilde{\phi}_{ijk}^e \right\rangle_E,
\end{aligned} \tag{2.31}$$

thus completing the weak formulation in inner product notation. We can develop the inner products that do not contain derivatives using (2.25), obtaining:

$$\begin{aligned}
&J_{i,j,k}\mathrm{w}_i\mathrm{w}_j\mathrm{w}_k\mathbf{q}_{t_{i,j,k}}^{eN} + \int_{\partial\Omega^E} \left(\tilde{\mathbf{f}}_a^{eN} - \tilde{\mathbf{f}}_v^{eN}\right)\cdot\mathbf{n}\phi_{ijk}^e \,\mathrm{d}S - \left\langle \tilde{\mathbf{f}}_a^{eN}, \nabla_\xi \phi_{ijk}^e \right\rangle_E + \left\langle \tilde{\mathbf{f}}_v^{eN}, \nabla_\xi \phi_{ijk}^e \right\rangle_E = J_{i,j,k}\mathrm{w}_i\mathrm{w}_j\mathrm{w}_k\mathbf{s}_{i,j,k}^{eN}, \\
&J_{i,j,k}\mathrm{w}_i\mathrm{w}_j\mathrm{w}_k\mathbf{g}_{i,j,k}^{eN} = \int_{\partial\Omega^E} \mathbf{q}^{eN}\tilde{\phi}_{ijk}^e \mathbf{n}\,\mathrm{d}S - \left\langle \mathbf{q}^{eN}, \nabla_\xi \tilde{\phi}_{ijk}^e \right\rangle_E.
\end{aligned} \tag{2.32}$$

Now we have a full system of semi-discrete equations, solving for the time derivative of the conservative variables at each node of the element, $\mathbf{q}_{i,j,k}^{eN}$. The gradients in (2.32) are calculated using (2.14), the inner product, or volume integrals with (2.12) and the surface integrals are evaluated at each face of the element and computed with the Gauss quadrature, the 2D version of (2.11). As the polynomials are continuous within one element, but is not imposed between elements, thus the surface fluxes on the face of element is not necessarily equal to the flux of the same face computed from the neighbour element. To handle this discontinuities, we replace the polynomial expansion of the fluxes of the surface integrals in (2.32) with numerical fluxes, $\mathbf{f}^*$, that are calculated using the state vector $\mathbf{q}$ on the face from both elements (some insight are given in Section 2.5), obtaining:

$$\begin{aligned}
&J_{i,j,k}\mathrm{w}_i\mathrm{w}_j\mathrm{w}_k\mathbf{q}_{t_{i,j,k}}^{eN} + \int_{\partial\Omega^E} \left(\tilde{\mathbf{f}}_a^{*} - \tilde{\mathbf{f}}_v^{*}\right)\cdot\mathbf{n}\phi_{ijk}^e \,\mathrm{d}S - \left\langle \tilde{\mathbf{f}}_a^{eN}, \nabla_\xi \phi_{ijk}^e \right\rangle_E + \left\langle \tilde{\mathbf{f}}_v^{eN}, \nabla_\xi \phi_{ijk}^e \right\rangle_E = J_{i,j,k}\mathrm{w}_i\mathrm{w}_j\mathrm{w}_k\mathbf{s}_{i,j,k}^{eN}, \\
&J_{i,j,k}\mathrm{w}_i\mathrm{w}_j\mathrm{w}_k\mathbf{g}_{i,j,k}^{eN} = \int_{\partial\Omega^E} \mathbf{q}^{*}\tilde{\phi}_{ijk}^e \mathbf{n}\,\mathrm{d}S - \left\langle \mathbf{q}^{eN}, \nabla_\xi \tilde{\phi}_{ijk}^e \right\rangle_E.
\end{aligned} \tag{2.33}$$

2.5 Numerical Fluxes

The exchange of information from one element to its neighbours is done by the surface integrals in (2.33), as all the volume integrals uses only the variables of the nodes of the same element. In this way, the numerical fluxes play the fundamental role of communicating elements, playing the role of a Riemann solver, similar to the FV methods. Choosing an appropriated numerical flux will be determinant in obtaining an stable numerical scheme, as some properties must be fulfilled, such as the flux being consistent and conservative. Many options with this properties have been developed in the FV context, and have been adapted for the DG scheme, being the most representative [105, 133, 134, 163]. All have in common that are functions of the solution on the faces of the inner ($\mathbf{q}^+$) and outer element ($\mathbf{q}^-$), also referred sometimes as left and right element, and the normal vector of the face.

Throughout this thesis we limit the numerical fluxes used for each term. We briefly introduced them:

- For the inviscid part, we use the Lax-Friederich [101] and the Roe Riemann Solver [134]. The Lax-Friederich flux is defined as,

$$\begin{aligned}\mathbf{f}_a^* \cdot \mathbf{n} &= \frac{1}{2}\left(\mathbf{f}_a(\mathbf{q}^+)\cdot\mathbf{n} + \mathbf{f}_a(\mathbf{q}^-)\cdot\mathbf{n} + \lambda(\mathbf{q}^+ - \mathbf{q}^-)\right), \\ &= \{\!\{\mathbf{f}_a\}\!\}\cdot\mathbf{n} + \frac{\lambda}{2}[\![\mathbf{q}]\!],\end{aligned} \tag{2.34}$$

  where λ is the largest eigenvalue of the linearized advective flux over $\mathbf{q}^+$ and $\mathbf{q}^-$. It has the property of being dissipative [163]. The original Roe flux is defined as,

$$\mathbf{f}_a^* \cdot \mathbf{n} = \{\!\{\mathbf{f}_a\}\!\}\cdot\mathbf{n} - \frac{1}{2}\sum_{i=1}^{Ncons} \tilde{\alpha}_i |\tilde{\lambda}_i| \tilde{\mathbf{k}}^{(i)}, \tag{2.35}$$

  where the $\tilde{\alpha}_i$ are averaged wave strengths, $\tilde{\lambda}_i$ are the average eigenvalues, and $\tilde{\mathbf{k}}^{(i)}$ are the averaged right eigenvectors in the normal direction. These parameters can be obtained by different strategies, being the most used the original one by Roe [134], and the one by Roe and Pike [133].

- For the viscous term, we use the Bassi and Rebay 1 formulation (BR1) [8],

and the Symmetrical Interior Penalty (SIP) method [50]. The BR1 scheme is a simple average of the variables on both sides of the face,

$$\begin{aligned} \mathbf{f}_c^* \cdot \mathbf{n} &= \{\{\mathbf{f}_c\}\} \cdot \mathbf{n}, \\ \mathbf{q}^* &= \{\{\mathbf{q}\}\}, \end{aligned} \tag{2.36}$$

The SIP method, adds dissipation using the difference between the state vector of each side of the face. A more detailed explanation and development is given in Chapter 4.

Boundary conditions are weakly imposed by using the boundary values as the exterior element value on the boundary faces and solving the correspondent Riemann problem using the Riemann solver of the numerical fluxes.

2.6 Time discretisation

As the main objective is solving time evolving cases, as aeroacoustic and turbulence are non-stationary, we need to integrate in time the semi-discrete set of equations. We start by rewriting (2.33) in a more compact and generic form:

$$\mathbf{q}^{eN}_{t_{i,j,k}}(t) = \frac{\mathrm{d}\mathbf{q}^{eN}_{i,j,k}}{\mathrm{d}t}(t) = RHS(\mathbf{q}^{eN}_{i,j,k}(t)), \tag{2.37}$$

where *RHS* stands for the right hand side part of the equation that includes all the integrals, jacobians and weights. The most simple classification of time integration methods is the way we treat the *RHS* term, more specifically, its dependence with the state variable vector $\mathbf{q}$. Defining $\mathbf{q}^{n+1}$ and $\mathbf{q}^n$ as two consecutive time steps, with n being the actual time step, we can calculate the $n+1$ step using the *RHS* evaluating it at $\mathbf{q}^n$, which is called an explicit time integration, or using $\mathbf{q}^{n+1}$, called implicit time integration. The former has the advantage that there are no unknowns variables and can be evaluated directly, thus are very simple and low cost [74, 105]. The latter creates a nonlinear system of equations, adding more cost, but with the advantage of having a wider stability region [11, 105].

In this thesis we will only use one method, which is an explicit one, the explicit Runge-Kutta of third order (ERK3) [173], formulated as,

$$\mathbf{q}^{n+1} = \mathbf{q}^n + \Delta t \sum_{i=1}^{s=3} b_i \mathbf{y}_i. \tag{2.38}$$

where the variable $\mathbf{y}$ can be defined as follows:

$$\begin{aligned} \mathbf{y}_1 &= RHS\left(\mathbf{q}^n\right), \\ \mathbf{y}_2 &= RHS\left(\mathbf{q}^n + \Delta t(a_{21}\mathbf{y}_1)\right), \\ \mathbf{y}_3 &= RHS\left(\mathbf{q}^n + \Delta t(a_{31}\mathbf{y}_1 + a_{32}\mathbf{y}_2)\right), \end{aligned} \tag{2.39}$$

and a_{ij} and b are constants of the method.

Part II

Introduction stabilisation techniques for under-resolved Navier–Stokes equations

Summary In this part we provide an introduction to techniques that make possible simulating under-resolved simulations using the DGSEM method, which are commonly encountered in real case scenarios. In Chapter 3 we describe the well-known Large Eddy Simulation method, along with different closure models, as well as an implicit version of the technique, detailing the changes of the numerical method that are necessary to achieve it. In Chapter 4, we continue with other implicit LES strategies, based on jump penalty methods, that create the dissipation that is needed for the stabilisation of challenging problems.

Chapter 3

Explicit and Implicit Large Eddy Simulations

Contents

3.1 Introduction 27
3.2 General LES formulations 29
3.2.1 Sub-grid scale models 29
3.3 Implicit LES for DGSEM 31
3.4 Numerical results 32
3.4.1 Turbulent channel 32
3.4.2 Turbulent airfoil 34
3.5 Summary 39

3.1 Introduction

In turbulent flows, there are many important scales, with different characteristics and behaviour. Some of the most important are the small scales, where the energy input from nonlinear interactions and the energy drain from viscous dissipation are in exact balance. These small scales have high frequency, causing turbulence to be locally isotropic and homogeneous, this feature of turbulence is called *Kolmogorov length scales* [167]. Properly solving these scales, with a mesh refined enough is called Direct Numerical Simulation (DNS), and is the most reliable method since no

models are used. However, the range of length scales and complexity of phenomena involved in turbulent flows make the DNS simulation prohibitively expensive, as the resolution required to resolve all scales is beyond what is computationally possible for many cases. Here, under-resolved simulations are the only possible option for obtaining high-fidelity solutions.

High order Discontinuous Galerkin (DG) methods provide accurate solutions by enabling arbitrarily high polynomial approximations inside each grid element. For high-order polynomials, numerical errors are not distributed along all wave numbers, but localised at high wave numbers [62, 73, 112, 119, 148]. This characteristic of high-order methods results in accurate simulations with low dissipative and dispersive errors. Although this characteristic is beneficial for well-resolved simulations, when computing under-resolved simulations, it can lead to unstable simulations.

In contrast to low order methods, high order methods do not have enough inherent numerical dissipation in under-resolved simulations, to dissipate large flow structures (when compared to the Kolmogorov scales). Therefore, computation of this kind of flows using DGSEM solvers requires localised dissipative mechanisms to dissipate flow structures close to cut-off size. Without it, the simulations will accumulate energy (and entropy) due to the lack of resolution of the small scales, which will eventually cause numerical divergence.

Different methods have been proposed to stabilise under-resolved computations with aliasing. Among others, split forms or skew symmetric variants [13, 178], localised interior penalty fluxes [56], over-integration [85, 86, 116], Spectral Vanishing Viscosity (SVV) [87, 110, 111] or filtering [12] can be incorporated into the solver to stabilise the computations and remove or alleviate the aliasing. Different stabilisation methods have been summarised in [16, 26].

In the current chapter we compare two dissipative stabilising mechanisms that enable the simulation of turbulent under-resolved flows. The former is the classic LES technique that uses explicit models to enhance the viscosity of the flow, and thus create dissipation. The latter relies on changing the numerical scheme in such a way that we can obtain energy stable properties. Both techniques are challenged with two test cases that are under-resolved turbulent flows, a turbulent channel and a turbulent NACA0012 airfoil.

3.2 General LES formulations

Large Eddy Simulation (LES) models are able to resolve turbulent fluctuation up to specific length scales. The principal idea behind LES is to reduce the computational cost of a fully resolved flow (DNS) by modelling the smallest length scales, which are the most computationally expensive to resolve, via low-pass filtering of the Navier–Stokes equations [167]. The large eddies are resolved, whereas the smallest ones can be modelled due to their isotropic behaviour. The effects on the resolved flow caused by the smallest eddies are included by means of a so-called sub-grid scale (SGS) model.

The filtered Navier–Stokes equations are similar to the original set of equations, having an extra term, τ_{ij}, which is the SGS stress tensor, and reflects the contribution of the smallest unresolved eddies. As mentioned above, the SGS contribution to the Navier-Stokes equations needs to be modelled. Most of the models assume a local equilibrium of the sub-grid scales,

$$\tau_{ij} = -2\nu_{SGS}\overline{S}_{ij} + \frac{1}{3}\tau_{kk}\delta_{ij}, \tag{3.1}$$

where ν_{SGS} is the sub-grid viscosity, δ_{ij} is the Kronecker delta, and

$$\overline{S}_{ij} = \frac{1}{2}\left(\frac{\partial \overline{u}_i}{\partial x_j} + \frac{\partial \overline{u}_j}{\partial x_i}\right), \tag{3.2}$$

is the large-scale rate-of-strain tensor. The use of the overbar indicates that the variables are filtered. To complete the equations, the sub-grid viscosity is added to the physical fluid viscosity to compute stress tensor in (15) that is part of the viscous flux, (12).

3.2.1 Sub-grid scale models

Most of the SGS models seek to model the sub-grid viscosity (also known as eddy viscosity) as a function of local resolved flow variables and the local filter width. Within all the models that have been proposed, the most famous is the Smagorinsky one [152], being the viscosity proportional to the local strain rate ($|\overline{S}| = \sqrt{2\overline{S}_{ij}\overline{S}_{ji}}$), which acts as a characteristic turbulent velocity,

$$\nu_{SGS} = (C_s\Delta)^2|\overline{S}|, \tag{3.3}$$

where Δ is the filter width that acts as a characteristic turbulent length scale, and C_s is a constant called the Smagorinsky constant, with a typical value of $C_s \approx 0.18$. This model has a variation that uses a dynamic C_S constant [104].

More advance models have been proposed, such as the Wall-Adapting Local Eddy-Viscosity model (WALE) [124], where the behaviour of the viscosity near the wall has been improved:

$$\begin{aligned} \nu_{SGS} &= (C_w\Delta)^2 \frac{\left(S^d_{ij}S^d_{ji}\right)^{3/2}}{\left(\overline{S}_{ij}\overline{S}_{ji}\right)^{5/2}\left(S^d_{ij}S^d_{ji}\right)^{5/4}}, \\ S^d_{ij} &= \frac{1}{2}\left(\frac{\partial \overline{u}_i}{\partial x_j}^2 + \frac{\partial \overline{u}_j}{\partial x_i}^2\right) - \frac{1}{3}\frac{\partial \overline{u}_k}{\partial x_k}^2 \delta_{ij}, \end{aligned} \tag{3.4}$$

where C_w is the constant of the model and δ_{ij} is the Kronecker delta. Another model is the one proposed by VREMAN [168], where the dissipation is small in the transitional and near-wall regions. It is defined as:

$$\begin{aligned} \nu_{SGS} &= C_v\sqrt{\frac{B_\beta}{\alpha_{ij}\alpha_{ij}}}, \\ \alpha_{ij} &= \frac{\partial \overline{u}_j}{\partial x_i}, \\ \beta_{ij} &= \Delta^2\alpha_{mi}\alpha_{mj}, \\ B_\beta &= \beta_{11}\beta_{22} - \beta_{12}^2 + \beta_{11}\beta_{33} - \beta_{13}^2 + \beta_{22}\beta_{33} - \beta_{23}^2, \end{aligned} \tag{3.5}$$

where C_v is the constant of the model and can be related to the Smagorinsky constant as $C_v \approx 2.5C_s^2$.

In low order methods, the definition of the filter length is clear, as is related with the size of the mesh. However, in the case of DGSEM, the polynomial order must also be taken into account. In this Chapter and all others that uses SGS models,

the filter length is averaged in each element, calculated as:

$$\Delta = \frac{\left(\Delta_x \Delta_y \Delta_z\right)^{1/3}}{p+1}. \tag{3.6}$$

where Δ_i is the size of the element in each direction.

3.3 Implicit LES for DGSEM

Another option to solve the Navier-Stokes equations in an under-resolved spatial discretisation is called implicit LES (iLES). The main idea is to rely on the numerical method to add dissipation, instead of using an explicit SGS model. In this case it is important that the numerical dissipation acts in a similar way, adding dissipation only at high wave numbers. Since high-order methods are able to resolve accurately low to medium wavelengths, iLES techniques are a good choice for challenging problems at moderate Reynolds numbers.

Riemann solvers are the classic option to include numerical dissipation in DG schemes [10, 171], since they naturally arise when discretising the non-linear terms. However, this dissipation is not enough for high Reynolds number applications, where there could be instability issues, related to aliasing errors [111]. To overcome these problems, stable and energy conserving formulations, mimicking the continuous equations can be included. In our work, we selected split-form discretisations, that are energy preserving [64].

Many studies have focused on the construction of entropy and energy stable schemes for the discontinuous Galerkin method [59, 61, 62, 64, 94, 112]. A review of entropy stable DGSEM schemes is given in [149]. For the compressible Navier–Stokes equations, we can modify the standard discrete version by rearranging (2.33), starting by splitting the volumetric integral of the inviscid and viscous fluxes, and applying the Gauss law to the former,

$$
\begin{aligned}
J_{i,j,k}\mathrm{w}_i\mathrm{w}_j\mathrm{w}_k\mathbf{q}^{eN}_{t_{i,j,k}} &+ \int_{\partial\Omega^E}\left(\tilde{\mathbf{f}}^*_a - \tilde{\mathbf{f}}^{eN}_a\right)\cdot\mathbf{n}\phi^e_{ijk}\,\mathrm{d}S + \left\langle\nabla_\xi\cdot\tilde{\mathbf{f}}^{eN}_a, \phi^e_{ijk}\right\rangle_E \\
&- \int_{\partial\Omega^E}\tilde{\mathbf{f}}^*_v\cdot\mathbf{n}\phi^e_{ijk}\,\mathrm{d}S + \left\langle\tilde{\mathbf{f}}^{eN}_v, \nabla_\xi\phi^e_{ijk}\right\rangle_E = J_{i,j,k}\mathrm{w}_i\mathrm{w}_j\mathrm{w}_k\mathbf{s}^{eN}_{i,j,k}, \qquad (3.7)\\
J_{i,j,k}\mathrm{w}_i\mathrm{w}_j\mathrm{w}_k\mathbf{g}^{eN}_{i,j,k} &= \int_{\partial\Omega^E}\mathbf{q}^*\tilde{\phi}^e_{ijk}\mathbf{n}\,\mathrm{d}S - \left\langle\mathbf{q}^{eN}, \nabla_\xi\tilde{\phi}^e_{ijk}\right\rangle_E.
\end{aligned}
$$

The required split-form necessitate Gauss–Lobatto (GL) quadrature points to cancel out boundary terms using the summation-by-parts simultaneous-approximation-term property (SBP–SAT) [30, 59], together with a two-point fluxes, to represent the divergence of the inviscid flux in equation(3.7).

These type of conserving schemes are designed to remain stable and energy conserving, mimicking the continuous equations, and consequently do not necessitate additional numerical dissipation. For this reason, they are often suitable for iLES simulations, where no sub-grid scales is used. Energy stable formulations have been used to enhance stability of the iLES simulations [64], and have been shown to achieve good predictions of global variables such as lift and drag [57]. This work continues with this idea and explores the prediction capabilities of modelling more detailed variables.

3.4 Numerical results

In this section we challenged the explicit and implicit LES techniques described in this chapter with two under-resolved cases, comparing both of them with reference results of very well resolved simulations (DNS). Both test cases are fully 3D and turbulent. The former one is a classic turbulent channel, while the latter is a NACA0012 airfoil, where transition to turbulence is expected along the airfoil.

3.4.1 Turbulent channel

In this Section, we test the stabilisation techniques with a turbulent channel flow at friction Reynolds number $Re_\tau = 950$ and Mach number $M = 0.2$. The friction Reynolds number is defined as $Re_\tau = u_\tau\delta/\nu$, where u_τ is the characteristic friction

velocity, δ is the half-height of the channel and ν is the kinematic viscosity. The channel geometry is set as $6\delta \times 2\delta \times 3\delta$ in the x, y, z axis, respectively. An initial stage of 20 flow-through units ($T = L_x/U$) is simulated to ensure a fully developed turbulent flow. The turbulence statistics are then recorded during a time span of $33T$.

Two wall-resolving grids (first node from the wall is located at $y^+ = 1$) with different levels of refinement are considered, labelled m1 (coarse) and m2 (fine). m1 consists of 121,500 degrees of freedom (NDOF) distributed as $45 \times 60 \times 45$ in the domain; m2 consists of 992,750 DOFs distributed as $95 \times 110 \times 95$. We consider two levels of polynomial order for each level of refinement, such that total NDOF and its distribution in each direction are achieved. Therefore, we used four different h-meshes, each of them with its respective polynomial order. These polynomials are either $p = 2$ or $p = 4$ for all cases.

Three different turbulence modelling strategies are considered: first the explicit WALE and Vreman SGS models using the standard DGSEM discretisation shown in Chapter 2, the second is the iLES simulation using the energy conserving formulation explained in Section 3.3, and the last is a combination of both, using explicit SGS models (WALE and Vreman) but using the energy conserving formulation.

The complete numerical formulation couples the standard DGSEM with the SGS models, using the Lax-Friederich flux and BR1 scheme for the inviscid and viscous flows, respectively. In addition, the polynomial discretisation is done using Gauss nodes for the standard DG formulation, while GL are used for the split-form formulation. In addition, for the latter the Kennedy-Gruber two-point flux [84] in order to be kinetic energy preserving.

The results for all cases are shown in Figure 3.1 for the mean velocity and the fluctuations in the streamwise direction and the cross streamwise-normal direction and compared with DNS simulations as reference. In general, for the coarse level of refinement (m1), there is a mismatch with the DNS results, although it is significantly smaller for the high polynomial order (p4) than for the lower one (p2). For the finer level, good agreement is found for the energy conserving formulations, both with and without SGS models. However, the mean velocity predicted by the WALE model with the standard DGSEM has larger values than the DNS simulations for the region after $y^+ = 10$, for the case of p2, while for the p4 the simulation was

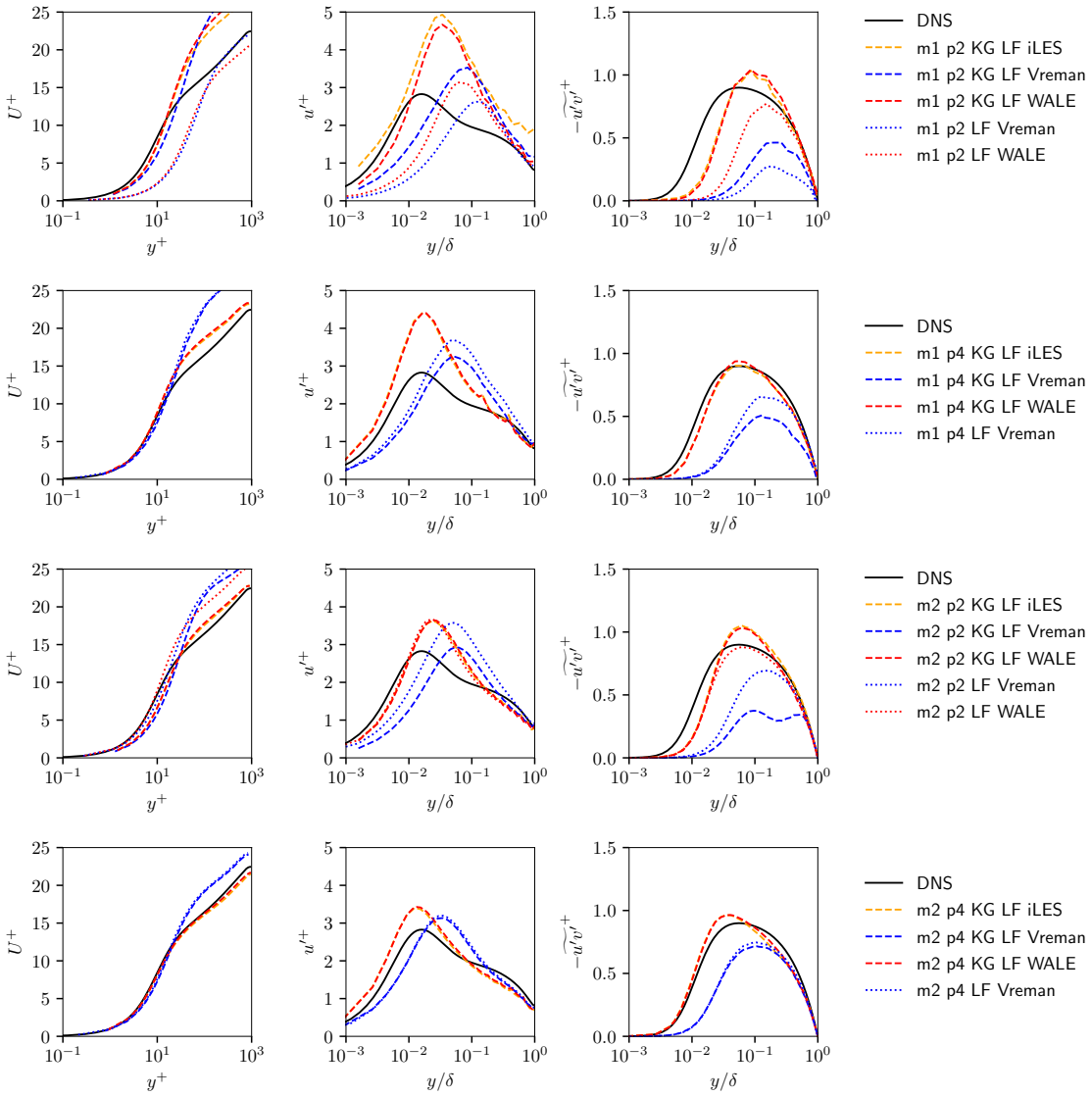


Figure 3.1: Velocity profiles of the turbulent channel at $\mathrm{Re}_\tau = 950$ comparison for different LES and iLES techniques. DNS results are from [75, 100]

not stable, finding a numerical divergence.

3.4.2 Turbulent airfoil

In this Section, we continue the comparison of explicit LES models and iLES in a different test case. Contrary to Section 3.4.1, we used both the WALE and VREMAN models as the explicit SGS models. In addition, the two-point fluxes used for the inviscid discretisation of the iLES are chosen to be kinetic energy preserving,

being the Pirozzoli flux [130], and the Kennedy-Gruber one (KG) [84]. An important remark is the change from Gauss nodes to Gauss-Lobatto nodes (compared to the explicit LES formulation), especially since the former provide higher accuracy [64, 91]. In all cases, we keep the same numerical fluxes used in Section 3.4.1, namely Lax-Friederich and BR1.

This test case consists of a NACA0012 airfoil section (of constant thickness and chord) with a sharp trailing edge and a low angle of attack, of $AoA = 4.0°$. We simulate it using the HORSES3D compressible Navier–Stokes solver and a Reynolds Number (Re) of $1.0 \cdot 10^5$, based on the chord of the airfoil (C) and the free stream velocity (U_∞), and a Mach Number ($Ma = 0.2$). Periodic boundary conditions are imposed in the spanwise direction.

The computational domain has dimensions of about $22C \times 20C \times 0.1C$, with the leading edge located at $[0, 0, 0]$ (see Figure 3.2). All the boundary conditions are weakly imposed via Riemann solver. An adiabatic no-slip wall on the airfoil surface; constant and uniform velocity profile of $[v_1, v_1, v_3] = [U_\infty cos(AoA), U_\infty sin(AoA), 0]$ at the inlet (left and bottom boundaries of the domain); and a pressure-based boundary condition is imposed at the outlet (right and top of the domain).

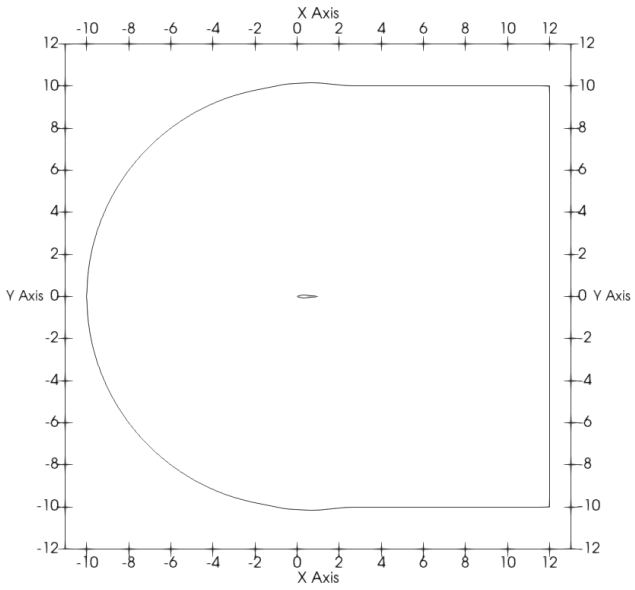


Figure 3.2: Computational domain and airfoil. Dimensions are defined in terms of chord units (C).

The external h-mesh is created using a C-type topology and is conforming. It is

constructed extruding uniformly a 2D mesh in the spanwise direction, having this 2D mesh a more refined region near the leading and trailing edge and near the airfoil surface. The 3D h-mesh consists of 23,370 elements.

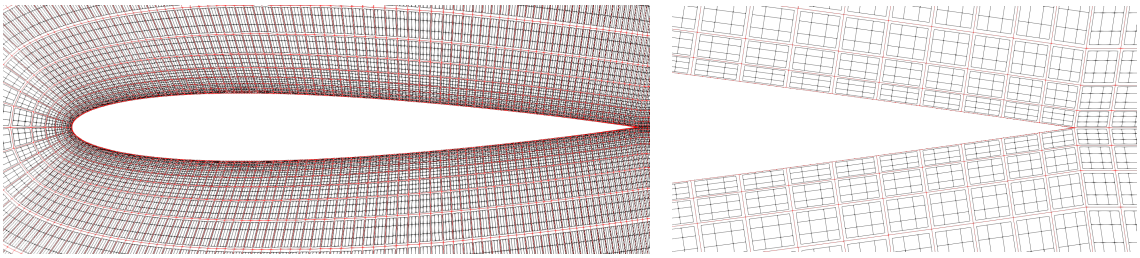


Figure 3.3: h/p mesh: red lines show coarse h-mesh and black lines the polynomial order 3 (4th order accuracy) mesh using Gauss nodes. left) mesh near the airfoil; right) zoom at the trailing edge zone.

The p-mesh uses isotropic polynomial order equal to 3, obtaining a total of almost 1.5 millions degrees of freedom (DoF). For the standard DG discretisation using SGS, the internal p-mesh is created using Gauss nodes, as seen in Figure 3.3; while for the split-form discretisation used in the iLES case, it uses Gauss-Lobatto nodes (as it is a requirement for the SBP-SAT, see Section 3.3).

The same domain and mesh is used for the LES with explicit SGS simulation (WALE and VREMAN), and for the iLES simulations (Pirozzoli and KG two-point fluxes). In all cases the simulations are advance in time using an explicit 3rd order Runge-Kutta scheme, with a Courant-Friederichs-Lewy (CFL) of 0.5. All the cases are run until the turbulent flow has fully developed, which typically consists of 70 convective time units ($T^* = C/U_\infty$) (starting from a uniform flow field). Subsequently, statistics are collected for $40T^*$.

The instantaneous contour of the velocity in the mid-span plane is shown in Figure 3.4 for the case of iLES using the Pirozzoli flux. The expected behaviour of the flow field can be seen, having a transition from a laminar flow at the vicinity of the leading edge to a turbulent flow exiting at the trailing edge in the suction side of the airfoil, while the pressure side exhibits a laminar behaviour at the wall of the airfoil.

The highlighted zone in Figure 3.4, the region between x/C 0.4 and 0.6 on the suction side, is zoomed in Figure 3.5, for all cases. In all but one case (WALE SGS), recirculation flow can be seen, but at very different positions and extensions. For

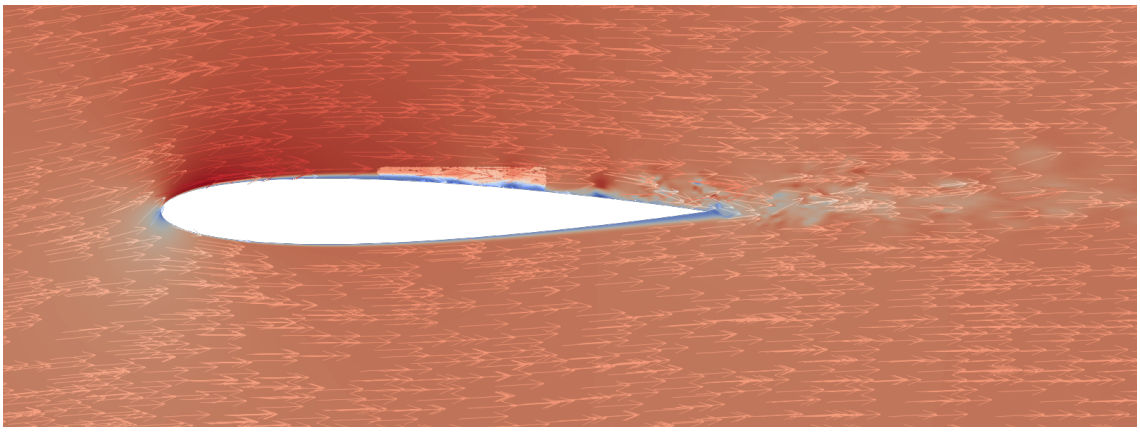


Figure 3.4: Velocity contour and velocity vectors and the mid-span plane for the iLES Pirozzoli case.

the LES cases with explicit SGS models, the attachment of the flow is clearer, being the WALE model the first one, showing already no recirculation at these positions. The VREMAN model follows a similar behaviour, being more attenuated, as there is a smaller bubble at $x/C \approx 0.43$. On the other hand, both iLES models show similar patterns, where several small recirculation bubbles can be observed along the cord.

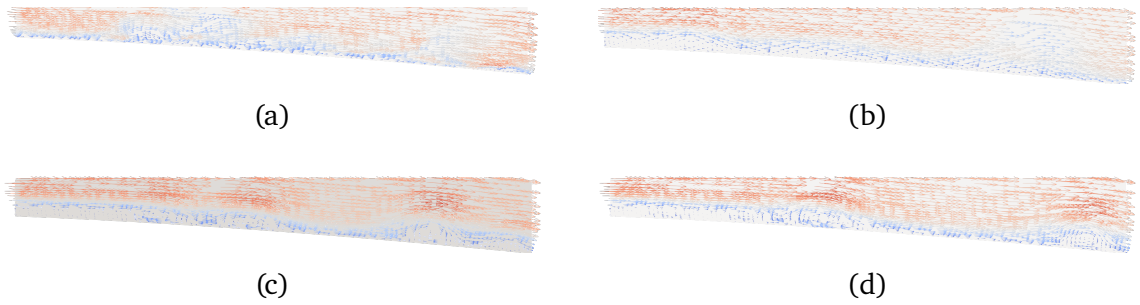
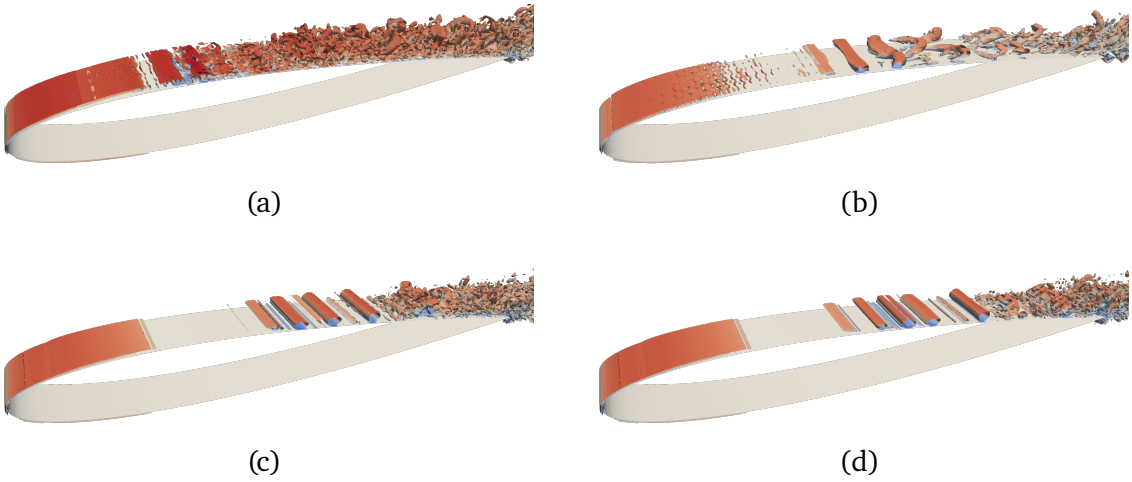


Figure 3.5: Velocity vectors in region x/C from 0.4 to 0.6: (a) LES with WALE SGS model, (b) LES with VREMAN SGS model, (c) iLES with Pirozzoli flux, and (d) iLES with KG flux.

The differences between each case can also be seen in the 3D flow. Figure 3.6 shows, for all cases, the instantaneous isocountours of the Q criterion proposed by Hunt et al. [78]. This criterion defines turbulent structures where there are positive values of the second invariant of the velocity gradient tensor (Q), which are regions where the rotations are more relevant than the strain. The WALE model predicted the transition to turbulence before mid-cord position, with a very small recirculation zone upstream (at $x/C \approx [0.1, 0.3]$). In contrast, the VREMAN model produces clearer laminar recirculation bubbles that are mostly 2D and evolve into

corrugated 3D structures which become later on turbulent structures at the vicinity of the trailing edge. As for the iLES cases, both show the exact behaviour, with a larger 2D laminar separation bubble until transition occurs (at $x/C \approx 0.6$).



(a) (b)

(c) (d)

Figure 3.6: Isocontours of the Q-criterion, coloured by the velocity magnitude. (a) LES with WALE SGS model, (b) LES with VREMAN SGS model, (c) iLES with Pirozzoli flux, and (d) iLES with KG flux.

To obtain a better understanding of the flow at the boundary layer, the streamwise velocity profiles in the normal direction of the time averaged flows are shown in Figure 3.7 at different positions along the chord. Averaged and instantaneous flows fields show similar patterns, and show a laminar separation bubble followed by a turbulent profile. The WALE model generates the separation bubble closer to the leading edge and also shows the shortest bubble length. After the mid-chord position, the profile shows the characteristic behaviour of a fully developed turbulent flow. Again, the VREMAN model predicts a more downstream start of the separation, with a slightly longer length. In contrast, the results obtained by the iLES configurations are almost identical, with very small differences, only appreciable at the trailing edge vicinity. The iLES cases predict a similar start of the separation bubble as the VREMAN model, but with a further downstream reattachment.

Overall we observe that all these LES technique predict a laminar region, transition to turbulence, and turbulence separation.

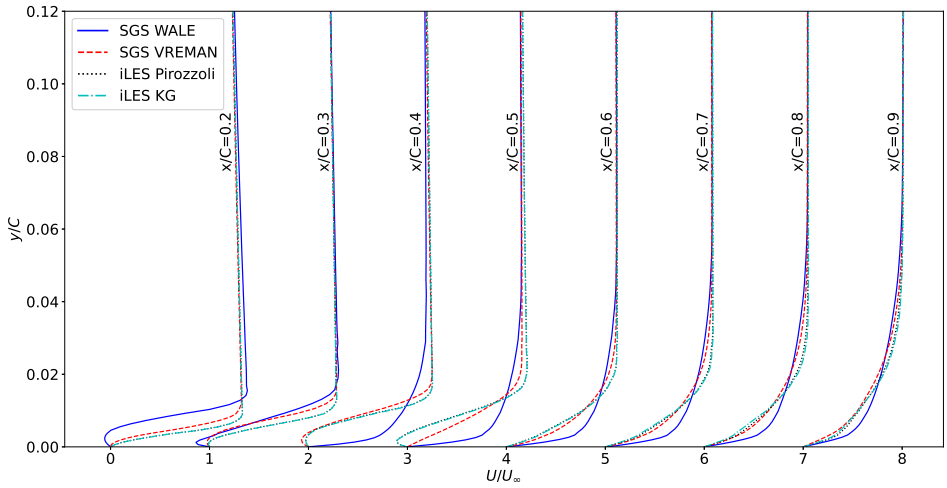


Figure 3.7: Streamwise velocity profiles of the mean flow in the normal direction.

3.5 Summary

In this Chapter we have introduced two different strategies to deal with turbulence in Large Eddy Simulation: explicit Subgrid Scale models and energy stable formulations for doing implicit LES. We have tested these techniques in the DGSEM framework for two test cases, both being fully 3D and time-dependent. The first case is a turbulent channel at $\mathrm{Re}_\tau = 950$, while the second is a NACA0012 airfoil at moderate Reynolds number, $\mathrm{Re} = 10^5$, where we found laminar separation bubble and transition to turbulence. In both test cases, we were able to obtain instantaneous and time averaged results for meshes that are in under resolved resolution, challenging the LES and iLES techniques.

In the turbulent channel we compared the explicit LES model in the standard DGSEM and the iLES using energy conserving formulations, as well as mixing them. The three of them are able to predict results with good agreement with more refined scenarios, namely DNS simulations, although the explicit LES with standard DGSEM using the WALE SGS model was not stable for higher polynomial orders. This case being fully turbulent, the energy conserving formulation proved to be more stable and compatible with explicit SGS models.

For the airfoil case, we challenge two SGS models and two two-point kinetic energy conserving fluxes. Both are able to capture the main physics, including the laminar

separation bubble and the transition to turbulence. Differences have been found in the locations of the position of the separation and reattachment, with explicit SGS models providing the smallest length of the bubble and at a more upstream position. While there are appreciable differences between both SGS models, the WALE and the VREMAN, for the implicit LES, the results of both two-point fluxes, the Pirozzoli and the Kennedy-Gruber are almost identical.

Chapter 4

Jump Penalty Method

Contents

4.1 Introduction 41
4.2 Background: Jump Penalty 42
4.3 Numerical results 45
4.3.1 Taylor-Green Vortex 45
4.3.2 Kelvin-Helmholtz Instability 48
4.4 Summary 52

4.1 Introduction

In Chapter 3 we presented methods that relies on preserving the energy or entropy to mantain the iLES simulations. On the other hand, a natural choice to enhance the robustness and control dissipation for DG is to rely on upwind Riemann solvers to dissipate small-scale flow structures that cannot be resolved by the selected discretisation (including grid size and polynomial order). The stabilising effect of Riemann solvers has been studied using von Neumann analyzes [3, 63, 121] for advection, showing promise as the solution jump correlates with the under-resolved scales. In addition for the compressible Navier–Stokes equations, it has been found that DGSEM offers controlled dissipation with improved robustness through the use of upwind Riemann fluxes across element interfaces [111].

An alternative to linking the stabilising dissipation to the advection fluxes is to consider the diffusive fluxes. Ferrer [56] proposed novel DG stabilisation for under-resolved turbulent flows and the incompressible Navier-Stokes equations, where the penalty parameter included in the DG Interior Penalty (IP) formulation was increased to provide stabilisation. When considering continuous methods like CG (C^0 continuity is imposed across the element interfaces), there are no jumps in the solution, but dissipative effects can be introduced considering the jumps of the gradient of the solution. This leads to the Continuous Interior Penalty (CIP) method [50] and the Gradient Jump Penalty (GJP) stabilisation [25], where the penalty is introduced for the jump of the solution gradient at the element interfaces. This method has been shown to be effective in stabilising laminar and turbulent flow simulations in [24] and [120]. Recently, jump penalty stabilisation has been proposed for spline approximations with higher smoothness to handle incompressible flow problems of high Reynolds number [162]. An advantage of jump penalty stabilisations is that the stabilisation is independent of the scheme, therefore, no change is needed for the original numerical methods. In addition, this stabilisation strategy is symmetric and completely decoupled from the time discretisation [120]. Therefore, it is potentially very useful for DG stabilisation, where the C^0 continuity is not required (and both gradient or solution jump penalties can be considered).

In this chapter we investigate the effect of jump penalty methods (penalising gradient or solution) for stabilisation and improvement of high-order DG schemes in for under-resolved cases of the compressible Navier–Stokes equations. Two cases are discussed, including the Taylor-Green vortex and the Kelvin-Helmholtz Instability problem.

4.2 Background: Jump Penalty

Recalling the numerical fluxes definition presented in Section 2.5, and in particular the Symmetrical Interior Penalty (SIP) method [50] for the viscous one, we can formulate it as

$$\mathbf{f}_v^* \cdot \mathbf{n} = \{\!\{\mathbf{f}_v\}\!\} \cdot \mathbf{n} + \sigma [\![\mathbf{q}]\!], \tag{4.1}$$

where $\{\!\{\bullet\}\!\}$ and $[\![\bullet]\!]$ stand for the average and jump operators, defined as,

$$\{\{\mathbf{q}\}\} = \frac{\mathbf{q}^+ + \mathbf{q}^-}{2}, \quad [\![\mathbf{q}]\!] = \mathbf{q}^+\mathbf{n}^+ + \mathbf{q}^-\mathbf{n}^-, \tag{4.2}$$

and

$$\{\{\mathbf{f}\}\} = \frac{\mathbf{f}^+ + \mathbf{f}^-}{2}, \quad [\![\mathbf{f}]\!] = \mathbf{f}^+ \cdot \mathbf{n}^+ + \mathbf{f}^- \cdot \mathbf{n}^-, \tag{4.3}$$

where the symbols + and − refer to the left and right interfaces, which is the projection of the values of the left and right elements onto the face. An explicit version of the solution jump penalty can be obtained by replacing (4.1) into (2.33) and rearranging

$$\begin{aligned} J_{i,j,k}\mathrm{w}_i\mathrm{w}_j\mathrm{w}_k\mathbf{q}^{eN}_{t_{i,j,k}} + \int_{\partial\Omega^E} \tilde{\mathbf{f}}^*_a \cdot \mathbf{n}\phi^e_{ijk}\,\mathrm{d}S - \left\langle \tilde{\mathbf{f}}^{eN}_a, \nabla_\xi \phi^e_{ijk} \right\rangle_E + \left\langle \tilde{\mathbf{f}}^{eN}_v, \nabla_\xi \phi^e_{ijk} \right\rangle_E \\ - \int_{\partial\Omega^E} \{\{\tilde{\mathbf{f}}^{eN}_v\}\} \cdot \mathbf{n}\phi^e_{ijk}\,\mathrm{d}S = J_{i,j,k}\mathrm{w}_i\mathrm{w}_j\mathrm{w}_k\mathbf{s}^{eN}_{i,j,k} + \int_{\partial\Omega^E} \sigma[\![\tilde{\mathbf{q}}]\!]\phi^e_{ijk}, \end{aligned} \tag{4.4}$$

making clear that the subtraction for the 1D case is replaced by the sum of the contribution of each face of the element. When we consider the Navier-Stokes equations, the vector of penalized variables $\tilde{\mathbf{q}}$ becomes:

$$\tilde{\mathbf{q}} = \mathbf{\Lambda}\mathbf{q}, \tag{4.5}$$

where $\mathbf{\Lambda}$ is the matrix that indicates the equations that are penalized.

When considering low Mach number flows (e.g., Taylor Green Vortex problem), we only penalize the jump of conservative variables in the momentum equations, and consequently:

$$\mathbf{\Lambda} = \begin{pmatrix} 0 & \mathbf{0}^T & 0 \\ \mathbf{0} & \mathbf{I}\mathrm{d}_{3\times3} & \mathbf{0} \\ 0 & \mathbf{0}^T & 0 \end{pmatrix}, \tag{4.6}$$

where $\mathbf{I}\mathrm{d}_{3\times3}$ is the 3×3 identity matrix and $\mathbf{0}$ is a column vector with 3 zero entries, with the aim of selecting only the momentum equations. If we consider compressible cases (moderate Mach numbers, e.g., Kelvin-Helmholtz Instability problem), we penalize all equations since the jumps in density and energy may become important. In the latter case, we set $\mathbf{\Lambda} = \mathbf{I}\mathrm{d}_{5\times5}$.

For the Navier-Stokes systems, the scaling of σ, in (4.4) is not trivial, the penalty can be scaled either with the local velocity of the element (part of the inviscid flux), or more naturally with the viscosity (the Reynolds number), as is part of the viscous flux, thus the explicit addition to the right-hand side of the discretised NS equation is:

$$\frac{\sigma}{\mathrm{Re}} \int_{\partial \Omega^E} [\![\tilde{\mathbf{q}}]\!] \phi_i. \tag{4.7}$$

where σ scales with the viscosity Re, $\sigma = \tau_s \mathrm{Re}$. As for the gradient jump penalty, the general expression that is added to the right-hand side of the NS equation, as proposed in [120], is in the form of,

$$\sigma \left\langle \frac{\partial \phi_i}{\partial n} G_{jump} \right\rangle \tag{4.8}$$

where the bracket term, $\langle\rangle$, represents the integration over the faces of the element, and G_{jump} is the numerical gradient-jump (the definitions of [120]). To obtain a similar form as for the solution jump, we need to consider three steps: first, the fact partial derivative of the normal is equivalent to the dot product of the gradient and the normal vector, $\partial \phi_i / \partial n = \nabla \phi_i \cdot \mathbf{n}$; second, the definition of the numerical gradient-jump in a single face, $G_{jump} = [\![\nabla \tilde{\mathbf{q}}]\!]$; and finally we use the same scaling factor as the solution penalty, i.e. the Reynolds number. Replacing, the penalty term can be expressed as

$$\frac{\sigma h^2}{\mathrm{Re}} \int_{\partial \Omega^E} [\![\nabla \tilde{\mathbf{q}}]\!] \nabla \phi_i \cdot \mathbf{n}, \tag{4.9}$$

where h is the grid size of the face (averaged). Again, σ scales with the viscosity Re, $\sigma = \tau_s \mathrm{Re}$. An important remark is that both gradients of (4.9) are with respect to the physical coordinates (x_i) and not with the reference coordinates (ξ_i), in a general mapping, the use of the Jacobian of the transformation and the contravariant vectors is needed, as explained in Section 2.3.1.

Finally, let us note that when we integrate over all elements in the mesh, we obtain global counterparts of (4.9) and (4.7), with penalty matrices, whose entries are: $\frac{\sigma}{\mathrm{Re}} \int_\Gamma [\![\phi_\mathbf{j}]\!] [\![\phi_\mathbf{i}]\!]$ and $\frac{\sigma h^2}{\mathrm{Re}} \int_\Gamma [\![\nabla \phi_j]\!] [\![\nabla \phi_i]\!] \cdot \mathbf{n}$, where Γ denote the faces of the elements in the domain. These jump penalty matrices (both for the solution and the gradi-

ent) are symmetric and positive semi-definite and therefore provide dissipation of energy to the numerical scheme. See more details in [56] for the solution penalty jump.

4.3 Numerical results

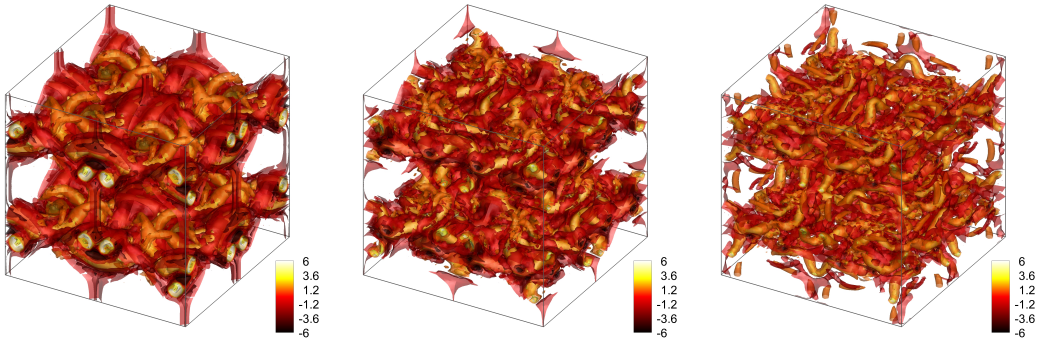
In this section we test the jump penalty stabilisation method descrived in this chapter with two under-resolved cases, comparing both of them with reference results of very well resolved simulations. The test cases are non-trivial and complex, and the selected meshes and polynomial order were found to be insufficient without the proposed stabilisation method, obtaining either a wrong behaviour of the solution or just not able to simulate the case due to numerical divergence. The proposed cases are the Taylor-Green Vortex and the Kelvin-Helmholtz Instability.

4.3.1 Taylor-Green Vortex

To challenge the jump penalization stabilisation in a 3D nonlinear case, we use the fully compressible Navier-Stokes equations to solve the classic Taylor-Green Vortex (TGV) problem. The TGV uses a three-dimensional periodic box $[-\pi, \pi]^3$ with the initial condition,

$$\begin{aligned} \rho &= \rho_0, \\ v_1 &= V_0 \sin x \cos y \cos z, \\ v_2 &= -V_0 \cos x \sin y \cos z, \\ v_3 &= 0, \\ p &= \frac{\rho_0 V_0^2}{\gamma M_0^2} + \frac{\rho_0 V_0^2}{16}(\cos 2x + \cos 2y)(\cos 2z + 2). \end{aligned} \tag{4.10}$$

The conditions for the case are set for a Reynolds number of $\mathrm{Re} = 1600$ and a Mach number of 0.1, solved using a Cartesian grid made of 32^3 elements, each of them enriched with a polynomial of order 3. The TGV problem has been widely used to study numerical methods to analyze how they can reproduce different flow regimes: an initial unstable laminar flow, a transitional laminar-turbulent flow, and a fully turbulent flow with isotropic decay; see Figure 4.1 and further details in [64, 111, 118, 144]. All reported times are non-dimensional using $t_c = L/V_0$ where



(a) $t/t_c = 7$. (b) $t/t_c = 10$. (c) $t/t_c = 13$.

Figure 4.1: Taylor Green vortex: Q-criterion for Re =1600 at different times t/t_c =7, 10 and 13.

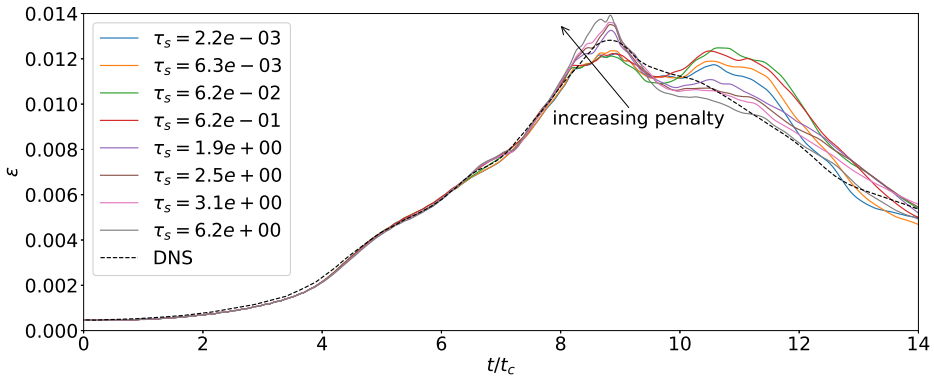
$L = 1$ is the reference length and V_0 is the characteristic velocity.

For this case the classic DG scheme (if no jump penalty term is included), the simulation diverges. As noted by Gassner et al. [61], this divergence relates to non-negligible aliasing errors in under-resolved simulations. The physical diffusion and the artificial diffusion due to the Riemann solver are, in these cases, insufficient to provide stabilisation and additional terms are needed (for example penalty jumps).

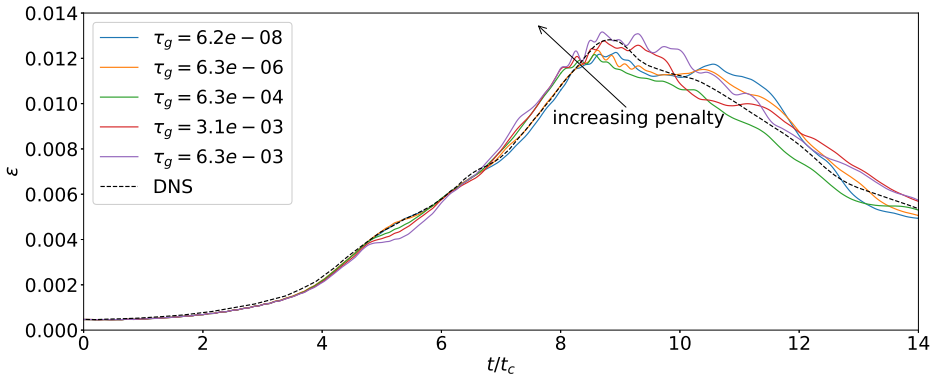
We compare in Figure 4.2 the dissipation rate of kinetic energy as the simulation evolves for the solution and the gradient jump and include a wide range of penalty parameters. Figure 4.2a shows that the penalty parameter in the solution jump significantly alters the kinetic energy dissipation rate; in particular, we observe that for low penalties there exist two peaks at t/t_c =9 and 11, while the DNS solution shows only one distinct peak at t/t_c =9. Increasing the penalty parameters decreases the second peak and recovers a time evolution similar to the DNS. The previous von Neumann analysis suggests that for low penalities there are significant dispersion errors at mid-large wavenumbers that alter the energy dissipation leading to the second artificial peak at t/t_c =11. When the penalty parameter is sufficiently large ($\tau_s > 1.9$), the second peak is lost and the correct energy dissipation is found. However, we observe a higher first peak (than in the DNS) when increasing the penalty, although the overall shape is correct.

Figure 4.2b shows the results for the gradient jump penalty stabilisation. Here, we also see that for very low penalization (baseline configuration) we obtain 2 peaks at t/t_c =9 and 11. When the penalty parameter is sufficiently large ($\tau_g > 6.3 \times 10^{-4}$),

the second artificial peak is lost, and we recover the DNS shape. In this case, the largest penalty recovers the correct magnitude for the peak at t/t_c =9 but provides an oscillatory behaviour at larger times. The overall trend is correct. Note that due to the scaling of the penalization parameter introduced in Section 4.2, very large penalization may be involved. For this reason, the system can become very stiff, and lower time step may be neede. One option to overcome this, is to treat this term implicitly, which is worth investigating in future works.



(a)

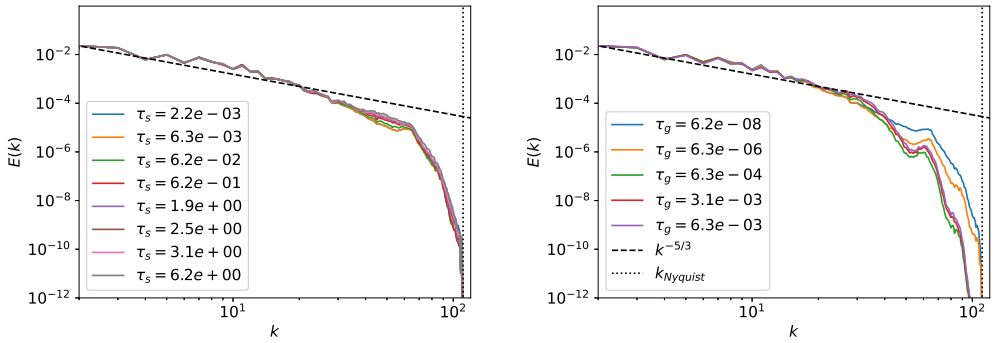


(b)

Figure 4.2: Taylor Green vortex: Evolution of the kinetic energy dissipation rate in time of the TGV for several penalty parameters compared with DNS results [171]. a) Solution Jump. b) Gradient Jump.

Having analyzed the integral quantities (over all wavenumbers), we now analyze the energy for all wavenumbers in Figures 4.3a and b. The figures depict the kinetic energy spectra at a fixed time $t/t_c = 8$ for the solution and the gradient jump, respectively. We observe that the value of the penalty parameter does not have a

significant effect in the case of the solution jump, while the energy decays significantly faster when considering large values for the gradient jump.



(a) (b)

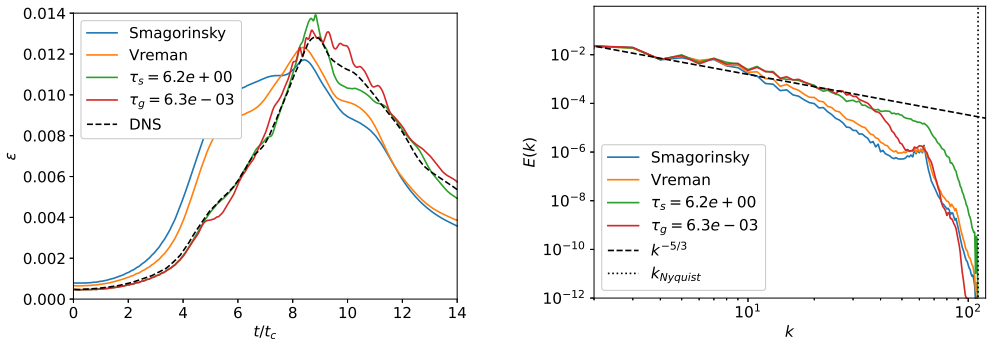
Figure 4.3: Taylor Green vortex: Kinetic energy spectra at $t/t_c = 8$ for several penalty parameters. a) Solution Jump. b) Gradient Jump.

Finally, we compare both jump penalty strategies (optimal penalty parameters) with the traditional LES Sub-Grid Scale (SGS) model (Smagorinsky [151] or Vreman [169] adapted to DG) in figure 4.4. Both the energy dissipation rate with respect to time (Figure 4.4a) and the energy spectra (Figure 4.4b) show the clear superiority of the jump penalty strategies over classic LES closure models. Figure 4.4a shows that classic closure models provide a lower maximum peak and a higher energy dissipation rate at earlier times than the peak $t/t_c < 8$, compared to DNS results.

Figure 4.4b shows that classic closure models dissipate significantly at midwave numbers, while jump penalties maintain the correct energy dissipation for higher wavenumbers. In addition, we observe that the solution jump allows higher wavenumbers to be captured. We conclude that both gradient and solution jump penalization stabilize under-resolved simulations and improve the simulations, when compared to the original unpenalized scheme and to classic explicit subgrid models (Smagorisnky and Vreman).

4.3.2 Kelvin-Helmholtz Instability

In this final section, we challenge the jump penalization methodology with the compressible and viscous Kelvin-Helmholtz Instability (KHI) problem. For this case



(a) (b)

Figure 4.4: Taylor Green vortex: Comparison with of jump penalty strategy with traditional LES SGS model. a) Energy dissipation rate. b) Energy spectra at $t/t_c = 8$.

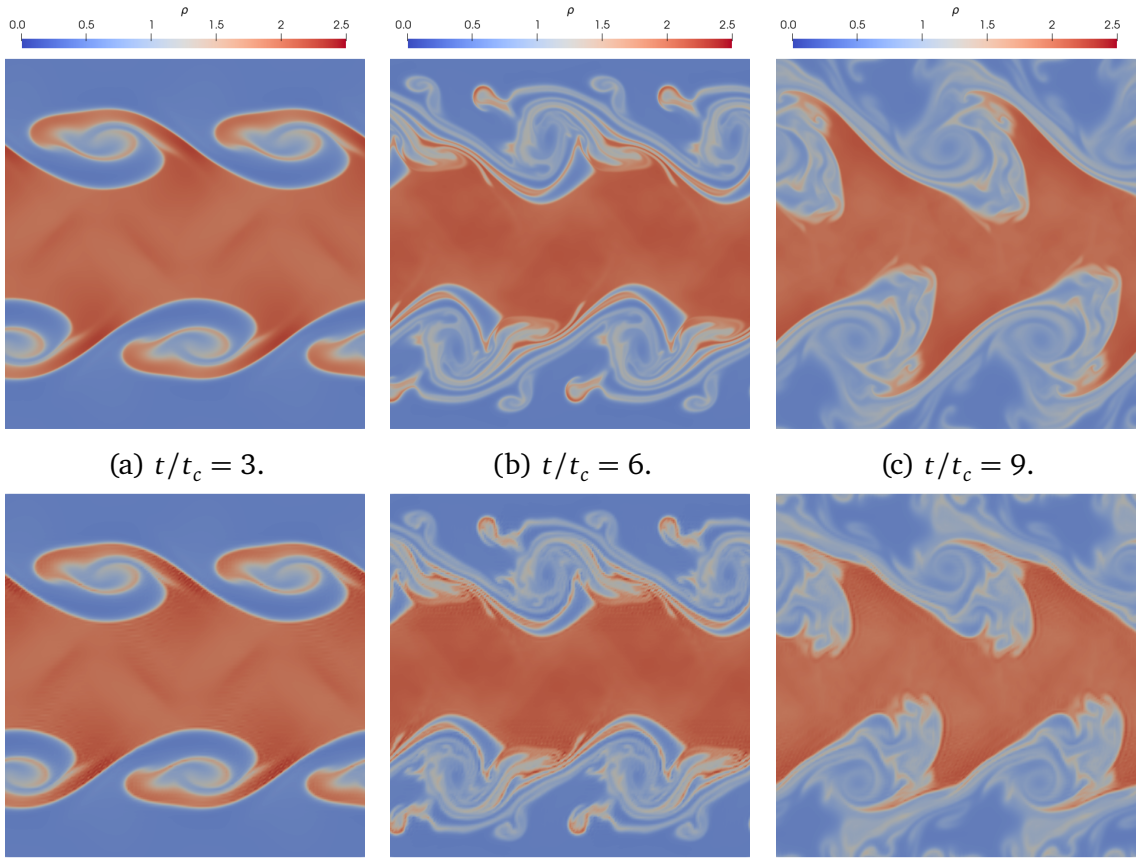
we use a 2D compressible Navier–Stokes equations, in a periodic square $[-1,1]^2$ with initial condition:

$$\begin{aligned} \rho &= \rho_0(0.5 + 0.75B), \\ v_1 &= 0.5V_0(B-1), \\ v_2 &= 0.1V_0 sin(2\pi x), \\ v_3 &= 0, \\ p &= 1, \\ B &= tanh(15y + 7.5). \end{aligned} \tag{4.11}$$

The KHI consist of a shear layer roll-up, as shown in Figure 4.5.

The initial conditions results in a high density contrast that makes compressible effects non negligible, reaching conditions of Mach number $Ma \leq 0.6$, see Rueda-Ramírez and G. Gassner [139]. Various studies have reported difficulties when time advancing this problem in coarse resolution, leading to numerical instabilities and divergence [32, 117]. In particular, DG schemes with and without entropy stable formulations [139] diverge for this case.

We set a Reynolds number of $\mathrm{Re} = 10^4$ (similar to the thin shear layer proposed by [117]) and a Mach number of 0.5. The domain is discretised in a Cartesian grid of 64^2 elements, each of them solved with a polynomial of order 3. The KHI is simulated using a standard DG discretisation (without jump penalization), and later using the solution penalty jump with a penalty parameter of $\tau_s = 0.01$. In



(a) $t/t_c = 3.$ (b) $t/t_c = 6.$ (c) $t/t_c = 9.$

(d) $t/t_c = 3.$ (e) $t/t_c = 6.$ (f) $t/t_c = 9.$

Figure 4.5: Kelvin-Helmholtz Instability: density for $\mathrm{Re} = 10^4$ at different times t/t_c =3, 6 and 9. Top row, well resolved case, 128^2 elements with $p = 5$. Bottom row, coarse unresolved case, 64^2 elements with $p = 3$, stabilized with solution jump penalty of $\tau_s = 0.01$

.

addition, we provide a well resolved case that we call reference solution. The latter uses a Cartesian grid of 128^2 elements, each of them with a polynomial of order 5, meaning $DOF = 768^2$ degrees of freedom, very similar to the resolution provided in [117]. Note that we do not include simulations using the gradient penalty jump, since these simulations diverged (for all τ_g considered, including $-1e-8, -1e-7, 1e-6, 5e-6, 1e-5, 5e-5$). Figure 4.6 shows the evolution of the mathematical entropy over time,

$$S_\Omega(t) = -\int_\Omega \frac{\rho s}{\gamma - 1} \;\; ; \;\; s = \ln(p\rho^{-\gamma}), \tag{4.12}$$

where γ is the gas heat capacity ratio.

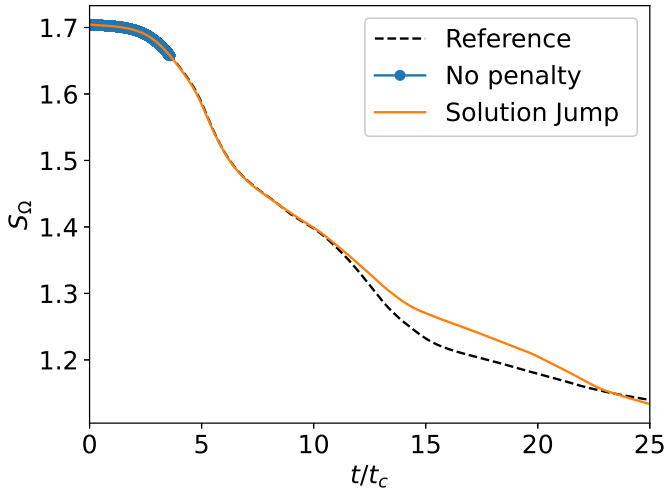
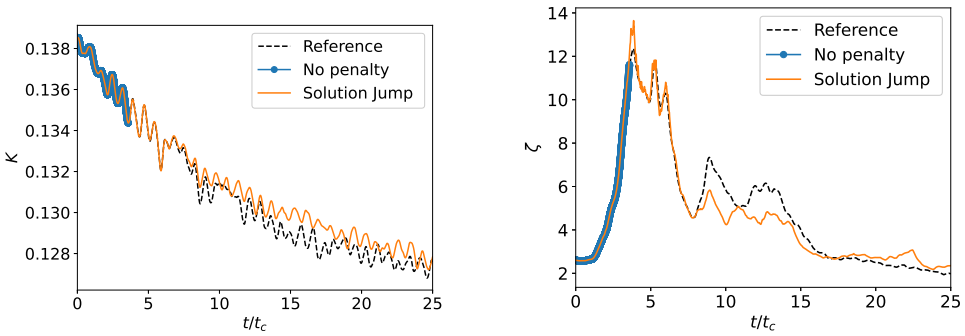


Figure 4.6: Kelvin-Helmholtz Instability: Evolution of the mean mathematical Entropy with and without jump penalty stabilisation.

It can be seen that the standard DG scheme (without jump penalty) diverges at the beginning of the simulation ($t/t_c \simeq 4$). When we include the solution penalty jump, the simulation completes, and provides results that match the reference solution until $t/t_c = 5$, and show small deviations after that time, which corresponds to the shear layer breaking up. For completeness, we depict in Figure 4.7 the evolution of kinetic energy and enstrophy in the domain, where a similar trend can be observed.



(a) (b)

Figure 4.7: Kelvin-Helmholtz Instability: Evolution of mean a) Kinetic energy b) Enstrophy with and without jump penalty stabilisation.

4.4 Summary

In this chapter, we have studied and compared two newly proposed techniques to stabilize under-resolved LES in high-order DG schemes. We analyze the numerical characteristics for two variants of the jump penalty stabilisation, one penalising the solution (proposed in [56]) and another penalising the solution gradient (proposed in [120]). We analyze these schemes with two test cases: a 3D turbulent Navier-Stokes through the Taylor-Green Vortex problem and a Kelvin-Helmholtz Instability. The main remarks are:

- Both jump penalizations improve the baseline scheme. In addition, we also show that they outperform classic LES models (Smagorisky and Vreman) in the 3D TGV problem. The optimal penalty for the solution and gradient jumps are the highest tested. This facilitates the estimation of this parameter but can lead to CFL-type restrictions.
- The jump penalty method can include impressibility effects and challenges classic DG schemes which often diverge. Including the solution jump penalization while using a coarse resolution provides stable simulations and accurate results that compare well with well resolved simulations.

Part III
Aeroacoustic methods

Summary The third part is devoted to methodologies that are used to calculate the generation and propagation of aeroacoustic in airfoils. We start in Chapter 5 with the direct computation, where the whole aeroacoustic is solved as part of the compressible physics of fluids, providing guidelines of this kind of simulations, including a physical one, the forced transition to turbulence and numerical a numerical one, such as the high-order polynomial refinement. In Chapter 6, we separate the generation and the propagation, using aeroacoustic analogies to solve the latter. We use the Ffowcs-Williams and Hawkings analogy, coupling it with the DGSEM method. Finally, in Chapter 7 we present the semi-analytical models of Amiet, providing a fast alternative for airfoil noise calculation, that will be used in the next section as part of the work-flow of computing the aeroacoustic of a whole wind turbine.

Chapter 5

Direct Noise Computation for Airfoils

Contents

5.1 Introduction 55
5.2 Under resolved turbulent airfoil 56
5.2.1 Laminar-turbulent tripping procedure 57
5.2.2 Computational setup 58
5.2.3 Evaluation of the Laminar-turbulent tripping 59
5.2.4 DNC and h/p mesh convergence 62
5.3 Fully resolved 2.5D airfoil 64
5.4 Summary 67

5.1 Introduction

Airfoil self-noise [22] is the minimum amount of noise produced by an aerodynamic surface and is the main noise source in modern wind turbines [126, 135]. It is caused by the interaction of the turbulent boundary layer with the blade surface close to the trailing edge, when the hydrodynamic pressure fluctuations that originated on the airfoil surface are scattered to the far field as noise, due to the sudden change of impedance in the blade trailing edge discontinuity [157]. This is the reason why the first step in analysing the acoustic of wind turbines is obtaining very accurate results on stationary airfoils.

Computational aeroacoustics (CAA) can be divided into two categories. The first one, noise generation, is characterised by turbulence and non-linear effects such as boundary layer and trailing edge noise. These processes are located near the wind turbine (or in general the solid surfaces) and are commonly called the near field. The second category is noise propagation, and is the process related with the propagation of the sound waves on the free stream. This can be simplified to a linear problem, and is often referred to as the far field problem. Each region has a different characteristic length of scale (and time scale) [9].

One possible method of CAA is to solve the near and far field together, using the compressible Navier-Stokes equations in the whole domain, obtaining all the physical effects on the solution without the necessity of using external models. This approach is called Direct Noise Computation (DNC) and has the advantage of dealing with complex phenomena naturally, such as acoustic feedback. The drawback of this method is that the mesh must be refined enough until the receiver's location, which by definition must be inside the domain. Therefore, this method requires high computational cost, especially when the receivers are far from the source. High-order methods are an excellent choice for this kind of computations, where the spectral accuracy is necessary for obtaining good results on the acoustic variables such as the pressure fluctuation.

In the current chapter we will focus on the direct noise computation of two cases using the DGSEM method, deepening in polynomial convergence of the acoustic calculations. The first case in Section 5.2 is an airfoil typical of a wind turbine, in a turbulent regime, being in under resolved conditions. The second case, presented in Section 5.3 is a fully resolved (DNS) NACA0012 airfoil at moderate Reynolds number.

5.2 Under resolved turbulent airfoil

In this section we aim to generate some guidelines of the complex problem of predicting the radiated noise of 3D airfoils sections using high-order techniques. In particular, we are interested in checking the performance of state of the art iLES simulations, presented in Section 3.3, using under resolved meshes, namely having a cell size that is more characteristic of aerodynamics simulations rather than aeroacoustic ones. We discuss how h/p convergence can be achieved for noise results, as well as the use of forcing the turbulent boundary transition (tripping) and

its effect on the acoustic.

We simulate a Siemens-Gamesa wind turbine airfoil section (of constant thickness and chord) with a blunt and straight trailing edge at a design angle of attack ($AoA = 5.5°$), using the HORSES3D compressible Navier–Stokes solver and a Reynolds Number (Re) of $3.3 \cdot 10^6$, based on the chord of the airfoil of $c = 900mm$, and a Mach Number ($M_0 = 0.15$). The airfoil is simulated with and without force transition. The position of the tripping centre (for the cases that have it) is located at a 5% on the suction side and 8% on the pressure side, both measured from the leading edge.

In this Section, we use the energy stable formulations to enhance stability for implicit Large Eddy Simulations (iLES). Since high-order methods are able to accurately resolve low to medium wavelengths, iLES techniques are a good choice for challenging problems at moderate Reynolds numbers, as the ones considered in this work [57, 64]. The required split-form necessitates Gauss–Lobatto points to cancel out boundary terms using the summation-by-parts simultaneous-approximation-term property (SBP-SAT); specifically, we use the Pirozzoli split formulation. In addition, non-linear inviscid and viscous numerical fluxes can be chosen appropriately to control dissipation in the numerical scheme [56, 111]. In this work we introduce dissipation through Roe fluxes. Furthermore, viscous terms are discretised using the Bassi-Rebay 1 (BR1) scheme, which is equivalent to the interior penalty formulation when using Gauss-Lobatto points and hexahedral elements [113].

5.2.1 Laminar-turbulent tripping procedure

Wind tunnel laboratory experiments often include tripping device on airfoil sections. Localised tripping mechanisms reduce the variability of wind tunnel ambient conditions which can be presented in natural laminar-turbulent transition, thus minimising variability in the transition location and subsequent changes in detachment lines, forces and aeroacoustics.

To avoid the high cost associated with explicitly meshing and simulating typical experimental zig-zag tripping devices, in this work, we model tripping using an external volume force acting on the fluid. The tripping model is based on the work of Schlatter [141] for flat plates, which we have adapted to airfoil sections. The forcing is described via the product of two independent functions, one that depends

streamwise and vertical directions (space only) and the other one that describes the spanwise direction and time (space and time):

$$F_{trip}(x,y,z,t) = f_s(x,y) \cdot g(z,t), \tag{5.1}$$

The space only function (f_s) is a Gaussian function of the attenuation of the force, centred at the position of the tripping device (x_0, y_0),

$$f_s(x,y) = \exp\Big(-[(x-x_0)/l_x]^2 - [(y-y_0)/l_y]^2\Big), \tag{5.2}$$

The time and spanwise direction function of (5.1)) is composed of a temporal and a spanwise fluctuation term,

$$g(z,t) = A_s h_1(z) + A_t([1-b(t)]h_2^i(z) + b(t)h_2^{i+1}(z)), \tag{5.3}$$

The former is modelled as a third-order Lagrange interpolant, with a time scale t_s,

$$b(t) = 3p^2 - 2p^3, \tag{5.4}$$

$$p = t/t_s - i, \tag{5.5}$$

$$i = int(t/t_s), \tag{5.6}$$

while the latter is calculated using random harmonic signals (h_1 and h_2^i) with nonzero values of amplitude at wavenumbers lower than a cutoff value of $2\pi/z_s$:

5.2.2 Computational setup

In this Section, two different h-mesh has been evaluated; both are C-type and completely conforming and hexahedral. Both of them can be considered coarsed for fully resolved boundary layer simulation, namely, it is an under-resolved turbulent solution that is possible to obtain using the iLES energy conserving formulation explained in Section 3.3. The coarse (mesh 1) consists of 23,400 elements, while the finer (mesh 2) has 58200, creating a more refined region near the trailing edge and the surface of the aerofoil. The domain consists of 20 chords in the stream and vertical direction, as shown in Figure 5.2. The p-mesh is uses isotropic polynomial orders ranging from 2 to 5, obtaining a total of 10 h/p different combination. In Figure 5.1 the two h-mesh can be seen with one of the chosen polynomial order

each.

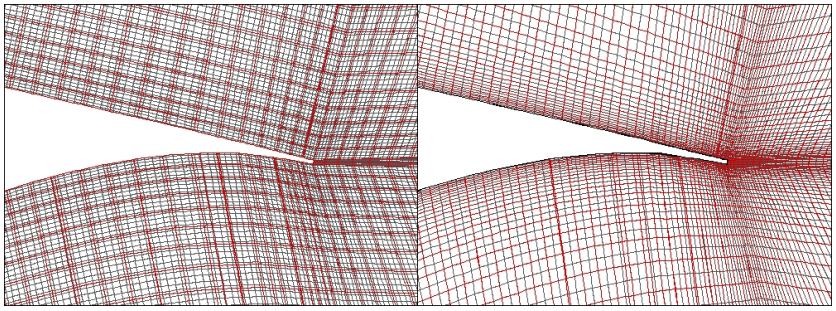


Figure 5.1: h/p meshes: left) mesh 1: red lines show coarse h-mesh and black lines the p=5 mesh and right) mesh 2: finer h-mesh in red and the p-mesh with p=2 in black.

All the boundary conditions are weakly imposed via Riemann solver. An adiabatic no-slip wall on the airfoil surface; constant and uniform velocity profile of $[v_1, v_1, v_3] = [U_\infty cos(AoA), U_\infty sin(AoA), 0]$ at the inlet (left and bottom boundaries of the domain); and a pressure-based boundary condition is imposed at the outlet (right and top of the domain). Periodic boundary conditions are imposed in the spanwise direction.

Pressure probes (receivers) are positioned at a uniform radial distance, at the mid-span point of the straight trailing edge. In addition, another set of probes is placed in a straight line and parallel to the free-stream flow direction, to mimic a typical microphone array. Both can be seen in Figure 5.2, being the former orange and the latter blue, along with their position in the computational domain and their relative position to the airfoil.

5.2.3 Evaluation of the Laminar-turbulent tripping

The effectiveness of the numerical tripping is first assessed. Several simulations are performed to tune the trip model parameters, t_s, z_s, which ensure the transition. The final values used are $1.7 \cdot 10^{-2}$ for the former and $7.4 \cdot 10^{-5}$ for the latter (where the values are nondimensionalized by the characteristic length (airfoil chord) and time (based on the chord and the free stream velocity)).

To verify that transition is forced near the tripping location, the wall pressure at the vicinity of the trailing edge (95% of the chord) is measured on the suction side.

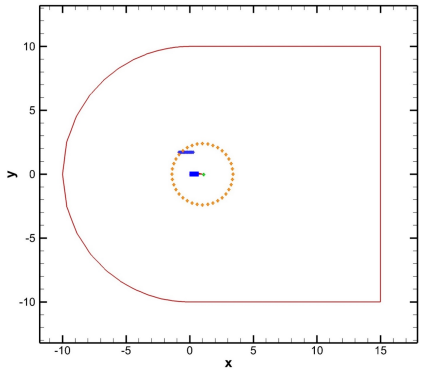


Figure 5.2: Topology of the computational domain and acoustic receiver locations. The lengths are not dimensionalized by the airfoil chord.

Figure 5.3 shows the results of performing a Fourier transform over the time history for both meshes at $p = 5$, no filtering or windowing is included. It is clear that mesh 1 without the tripping activated does not present turbulent behaviour and shows a single tonal peak. The signal completely changes once the tripping is activated, obtaining turbulent-like spectra. It is also important to note that for the refined h-mesh mesh 2, natural transition is observed in the simulation, showing a similar behaviour to that obtained when tripping. Although it is not the objective of this work to evaluate the capabilities of high-order schemes to capture natural transition, its impact of noise emissions will be also evaluated and compared with the case where the boundary layer is tripped. For illustration, the boundary layer transition can be observed using the lambda-2 criterion in Figure 5.4, where turbulent structures can be seen in the vicinity of the trailing edge for both the suction and pressure sides.

The other important parameter of the trip model is the amplitudes of spanwise fluctuation term (A_s and A_t). For the present case, both are chosen to be equal, and its effect on the far field noise is shown in Figure 5.5, in the form of sound pressure level (SPL), defined as,

$$SPL = 20 \log_{10} \frac{p_{rms}}{p_{ref}}, \tag{5.7}$$

where p_{rms} is the root mean square of the acoustic pressure and $p_{ref} = 20\mu Pa$ is a reference pressure. The SPL is calculated at the position of the microphone array (blue dots in Figure 5.2). It can be seen that without the force transition of the boundary layer using the coarse mesh, SPL spectra has a laminar behaviour, having

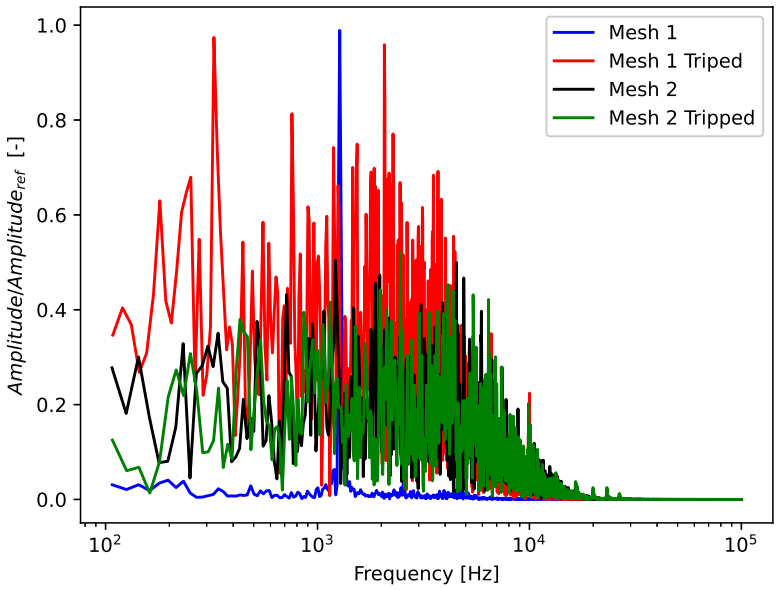


Figure 5.3: Effect of numerical tripping: Fourier transform of wall pressure near the trailing edge, the amplitude is nondimensionalized by the highest peak amplitude.

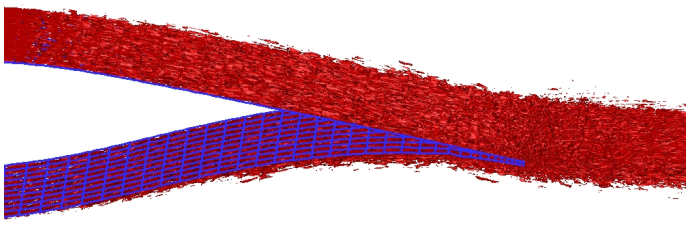


Figure 5.4: Instantaneous isosurface of lambda-2 criterion for refined mesh (mesh 2) with p=5.

a clear peak at about 1200 Hz, which is believed to be due to the bluntness of the trailing edge. When the amplitude is increased, the profile tends to a broad-band noise shape, being converging at a value of 100, where the boundary layer is fully turbulent at the trailing edge. This value was chosen for the rest of the studies.

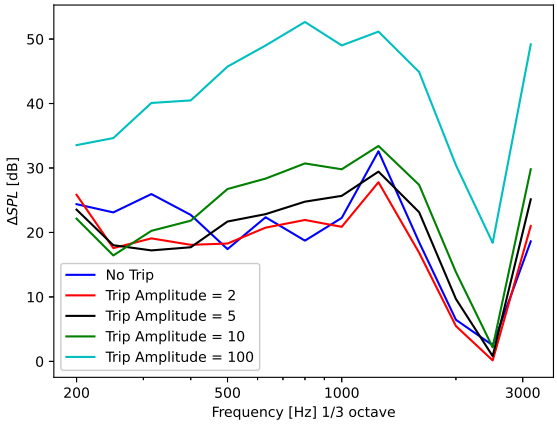


Figure 5.5: Effect of the trip amplitude for the microphone array SPL for the coarse mesh (mesh 1). The SPL is subtracted by the lowest value.

5.2.4 DNC and h/p mesh convergence

To obtain guidelines for direct computations, a mesh convergence study is performed for the acoustic fluctuation pressures at far field receivers. This is performed by comparing the mean value of the SPL at the linear microphone array, for both h-meshes and polynomial orders ranging from 2 to 5, all of them using the natural transition and the trip model.

The results of the natural transition (i.e. without tripping) are shown in Figure 5.6 as a 1/3 octave band. It is clear that a convergence has not been obtained, and that both, the h-mesh and the polynomial refinement have a strong impact on the far field noise. This was expected, as the change in pressure at the trailing edge caused by the boundary layer (Section 5.2.3) was very clear and consequently for the generation of noise. Without the tripping, an even more refined mesh is needed, to be able to capture this natural transition and obtaining a fully turbulent boundary layer at the trailing edge.

On the other hand, when the forced trip is activated, the pattern changes, as seen in Figure 5.7. Good agreement for both h-meshes at the same polynomial order

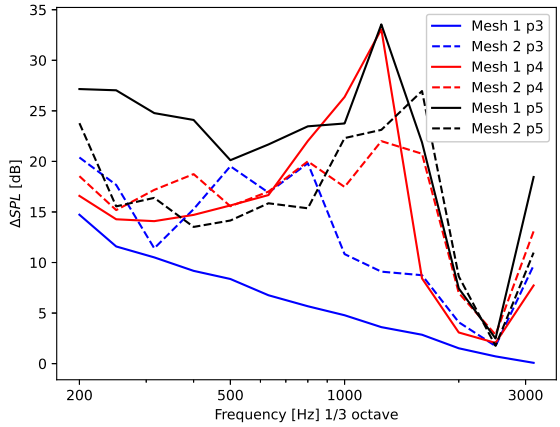


Figure 5.6: Mesh convergence for microphone array SPL, natural transition configuration. The SPL is subtracted by the lowest value.

is found, which suggests a weak dependence of the mesh near the trailing edge region, when analysing the far field signals with trip model.

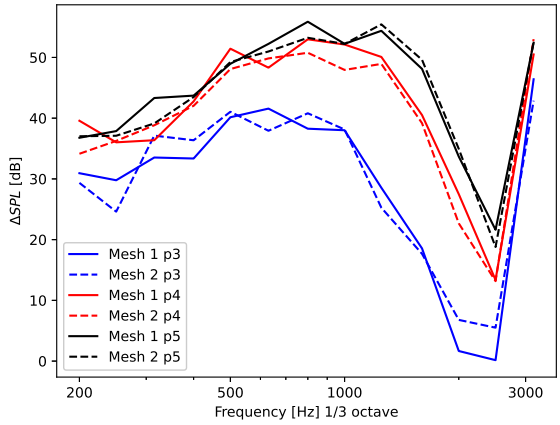


Figure 5.7: Mesh convergence for microphone array SPL, tripped configuration. The SPL is subtracted by the lowest value.

The dependence of the polynomial order is found to be important, obtaining a notorious change when going from polynomials 3 to 4, but attenuated for 4 to 5. As the p-mesh is constructed by isotropic polynomials of the same order throughout the domain, the better accuracy for high polynomials can be linked to better capturing noise propagation rather than the generation (which was unchanged for 2 h-meshes with same polynomials). This idea is reinforced as the differences are higher for medium and high frequencies, where the fluctuations in these ranges are expected to be dissipated by the numerical scheme.

For illustration, the dilation field (the divergence of the velocity), which gives a clear picture of the noise radiation, is shown in Figure 5.8 for the most refined configuration (mesh 2 with p=5). In the figure we clearly observe how the pressure waves are emitted from the trailing edge and propagated to the far field.

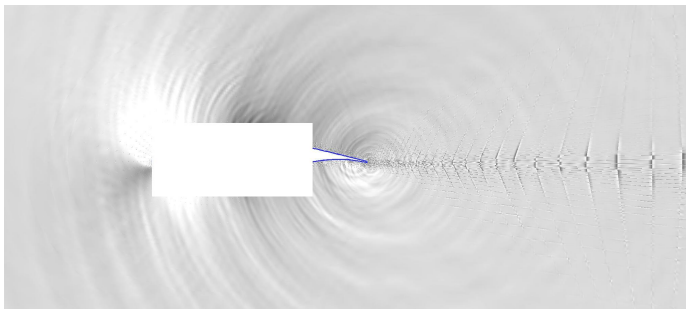


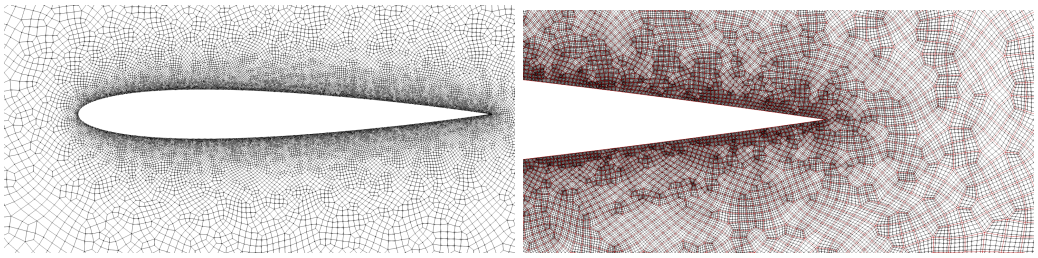
Figure 5.8: Instantaneous dilation field for refined mesh (mesh 2) with p=5.

5.3 Fully resolved 2.5D airfoil

In the following Section we extend the direct computation with an airfoil fully resolved, having a mesh much finer than the previous case. Due to computational restrictions, we do not solve the full 3D flow, but a 2.5D one, that is only one element in the spanwise direction, with a polynomial of order 2 in this direction. We present some instantaneous and time-averaged results, with emphasis in polynomial convergence for aeroacoustic computation in frequency spectra and directivity pattern.

The test case is a NACA0012 airfoil at Re $= 10^5$, $M_0 = 0.4$ and $AoA = 0°$, same configurations of [9, 79]. Boundary conditions are set in the same way as in the previous case, as is the case for all the numerical settings, using the Roe Riemann solver, BR1 viscous discretisation, split-form formulation with the Pirozzoli two-point flux in GL nodes. The domain has a C-shape extendend up to $50C$, discretised in non-conforming hexahedral elements, with refinement near the airfoil walls, as can be seen if Figure 5.9. The mesh has a total of 44,700 elements, with a wall size of $[\Delta x, \Delta y]/C = [1.5 \times 10^{-3}, 1.8 \times 10^{-3}]$. Constant polynomial order is used in all elements, ranging from 1 to 5 in the streamwise and normalwise direction.

First we present instantaneous results for the $p = 5$ simulation, which gives a qualitative view of how well the flow is resolved. Figure 5.10a shows the vorticity con-



(a) (b)

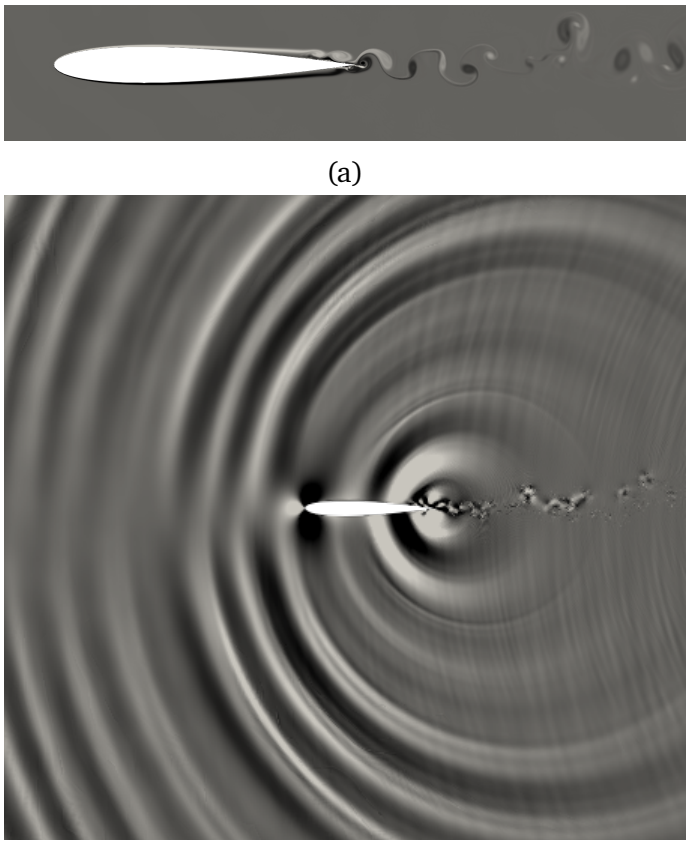
Figure 5.9: Detail of mesh used for the NACA0012 simulation. a) h-mesh near the airfoil. b) h/p mesh near the trailing-edge, red lines show h-mesh and black lines the p=5 mesh .

tour, where the complex flow at the wake can be seen, as well as some oscillations at appropriately $0.9C$ on the suction side of the airfoil. In Figure 5.10b we present the dilation field, as a representation of the aeroacoustic directly resolved from the compressible NS equations. The general behaviour is the emission of acoustic waves from the trailing edge of the airfoil propagating to the far field, with some minor disturbances in the vortex of the wake.

We continue with the polynomial convergence of time-averaged variables. In Figure 5.11 we present the mean streamwise velocity and its fluctuations in the wake of the airfoil, in a vertical line at $x/C = 1.1$, with the origin at the leading edge. We can see some fluctuations in the $p = 1$ results for both variables, which means a poor resolution of the flow, as well as large variation with the next refinement level, $p = 2$. These variations are reduced as we refine, being very small going from $p = 4$ to $p = 5$. In this way, for the higher polynomial order, the flow converges.

We now compare the polynomial convergence of the direct calculation on a point located at $[x, y]/C = [0.5, 0.5]$, comparing the power spectral density (PSD) of the pressure fluctuations obtained with a probe. The PSD is calculated using the Welch method with 50% of overlap and employing Hanning windowing for a total of $36T^*$ after the flow is statistically converged. The results are shown in Figure 5.12, where the expected broadband spectra is found for all polynomial orders except for $p = 1$, which was anticipated in the poor capture of flow hydrodynamics, leading to poor direct aeroacoustic results. A broadband tone appears for the higher polynomials at a Strouhal ($St = fC/U_0$) of approximately 3.8, similar to the numerical results of [9, 79]. Similar broadband decay and trending are captured for the simulations of polynomials 3 to 5 with some differences on the peaks' values.

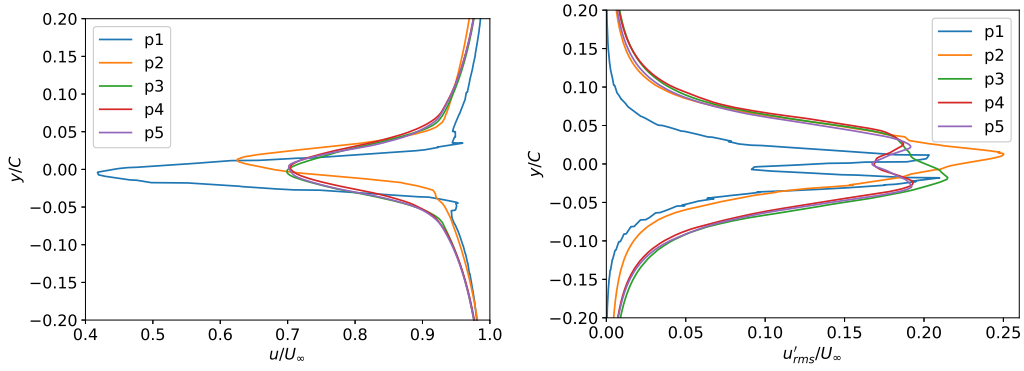
Last we compare the directivity of the acoustic in the form of the overall sound



(a)

(b)

Figure 5.10: Instantaneous flow variables for p=5. a) Vorticity. b) Dilation field



(a) (b)

Figure 5.11: Velocity profile at the wake for all polynomial orders at $x/C = 1.1$. a) Mean streamwise velocity. b) Fluctuations of the streamwise velocity.

pressure level (SPL), calculated as the integral of the PSD over the whole frequency range. The OSPL is calculated for the 120 points located in a circle of $2C$ with the

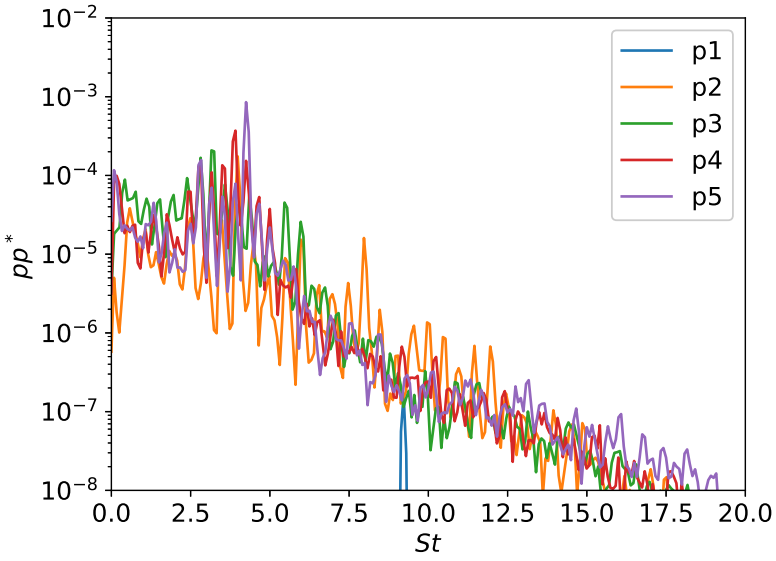


Figure 5.12: Polynomial convergence of the PSD of the acoustic pressure of a point located in $[x, y]/C = [0.5, 0.5]$.

centre at the trailing edge. Figure 5.13 shows the results for all polynomial orders, with very poor results for the $p = 1$ case. The shape obtained for all other cases is a dipole-like tilted to the upwind direction, with small loves at 135° and 225° and a large one in the zone of about $[-10°, 10°]$ which is greatly influenced by the wake of the flow, behaviour also found in [79]. As the OSPL is integrated over all frequencies, a better convergence is achieved while increasing the polynomial order, since the results for polynomials 3 to 5 are in almost perfect agreement, with some differences in the wake zone, as more chaotic behaviour is present.

5.4 Summary

In this Chapter we have shown that it is possible to perform flow and CAA simulations of airfoils using a high-order discontinuous Galerkin compressible Navier-Stokes solver. We have challenged the solver with two conditions, both at moderate Reynolds numbers, which are typically found in wind tunnels. The first one is an under-resolved, 3D turbulent case, where we used an implicit Large Eddy Simulations approach coupled to energy stable formulations to assures stability. The second case is a fully resolved 2.5D DNS scenario, where no model nor special formulations are used.

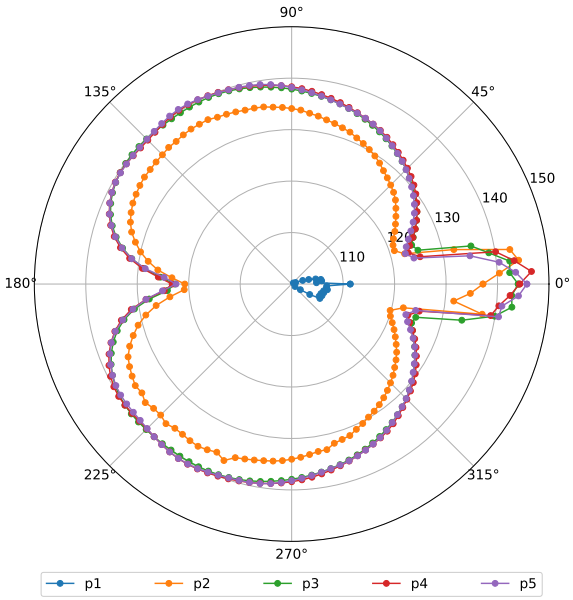


Figure 5.13: Polynomial convergence of the OSPL directivity (in dB) at $r = 2C$ calculated with direct computation.

In the first test case, the dependence of the aeroacoustic solutions on the forced transition of the boundary layer (tripping), the local and global h / p refinement is addressed. We have found a strong dependency of the transition behaviour for coarse meshes, which is minimised when including tripping. The noise generation is less susceptible to changes of mesh size when the transition is forced by the tripping model, whereas the propagation using direct numerical computation requires a fine polynomial resolution in all the space, from the source to the far field in order to capture well the behaviour. In general, for under-resolved meshes, aeroacoustic convergence can be obtained using a force transition of the boundary layer, whereas is not possible for a natural transition configuration. To achieve the latter, finer meshes are needed in order to fully resolve the boundary layer and capture the details of the flow.

In the fully resolved case, the aeroacoustic solutions converged as the polynomial was increased, both in the frequency spectra and overall directivity pattern. As the boundary layer is fully resolved, no external force is needed, such as tripping, to achieve convergence.

Chapter 6

Aeroacoustic Analogies

Contents

6.1 Introduction 69

6.2 The Ffowcs-Williams and Hawkings analogy 71

6.3 Validation 74

6.3.1 Monopole in moving medium 74

6.3.2 Cylinder in moving medium 75

6.4 Airfoil acoustic computation 79

6.4.1 Polynomial convergence 80

6.4.2 Comparison with direct computation 81

6.5 Summary 83

6.1 Introduction

In Chapter 5 we stated that the study of acoustic can be divided into two different regions. Each region has a different characteristic length of scale (and time scale), which are different in order of magnitude. Figure 6.1 illustrates these regions and their characteristics. We also presented the direct method, DNC, where both regions and scales are solved at the same time, limiting to small distances due to restrictions in computational resources.

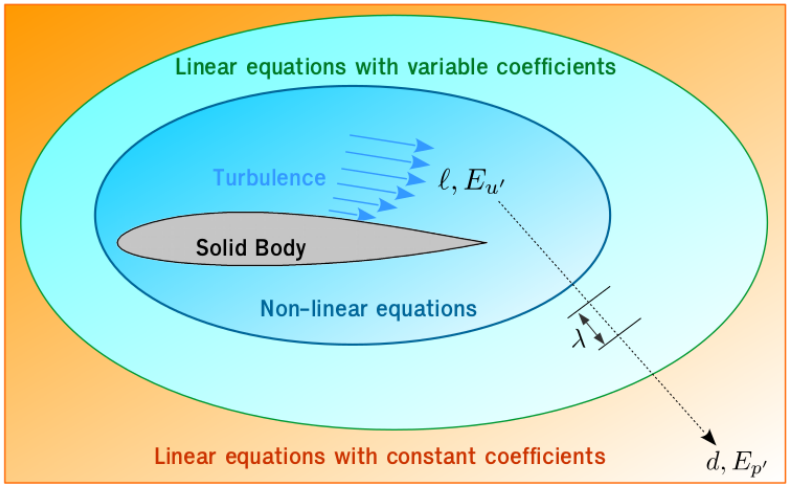


Figure 6.1: Diferent categories and regions of aeroacoustics and their scales [9].

The other possibility for this problem is decoupling the near and far field into two separate computational processes, which is named the hybrid approach. Here, the CAA solution becomes a two-step process, where the near field is computed first and its results are an input for the far field computation. This methodology is generally preferred due to the lower cost in large complex simulations.

The models of the far field are most commonly refered as Acoustic Analogies and, in contrast with the DNC approach, there are many options to model this far field propagation. The first one developed was done by Lighthill [106] where the Navier–Stokes equations were rearranged in such a way that the wave equation appears explicetly on one side of the equation, with the assumption of a quiescent base flow. Later, this was extended by Ffowcs-Williams and Hawkings [172] to flows that are bounded by solid surfaces and can be moving. A more general model was presented by Goldstein [68] rearranging the Navier–Stokes equations in the form of the Euler equations in a linear homogeneous presentation, and it is commonly known as Linearized Euler Equations (LEE). A variant of this model named Acoustic Perturbation Equations (APE) was derived [53] which overcomes the instability problems that occur when the flow is non-uniform.

Following these analogies, equivalent acoustic sources can be extracted from the well-resolved near field region. These can be subsequently modelled and injected into a new simulation to predict their propagation (in the time or frequency domain). The decoupling enables faster computations, since the near field that requires highly accurate flow computations can be performed separately from the

acoustic propagation. The Ffowcs-Williams equations are commonly solved in the time domain [18, 19, 54, 55, 108] and in the frequency domain [2, 65, 109, 115, 156, 174, 175], whereas the LEE and the APE equations are more commonly solved using time domain strategies; particularly high-order methods such as DG have been promising [6, 9, 44, 170].

The LEE and the APE equations are more suitable for regions where the flow is still non-uniform and are more computationally expensive than the Ffowcs-Williams and Hawkings. For this reason, the former group is solved in a closer region (the second part of Figure 6.1), while the latter could be used in longer distances. In this thesis we will focus only on the FWH analogy, as it is more suitable for wind turbine (and airfoil), where the receivers tend to be further away from the turbine itself, the far field.

The rest of this Chapter is organised as follows. First, we introduce the FWH analogy in Section 6.2. Then, we validate the implementation of the FWH solver in HORSES3D with two canonicall test cases in Section 6.3. Finally, in Section 6.4 we compare the results of the FWH analogy with the direct computation of the airfoil case presented in Section 5.3, along with a polynomial convergence of the noise values in the far field.

6.2 The Ffowcs-Williams and Hawkings analogy

The original Ffowcs-Williams and Hawkings (FWH) aeroacoustic analogy [172] is an extension of the Lighthill analogy [106], including solid boundaries. For this, it rearranges the compressible NS equations into an inhomogeneous wave equation. Multiple work has been done to generate further development of this analogy; for example, Farassat [55] and Di Francescantonio [48] have deepened in the use of permeable surfaces. More general formulations can be found in [66, 108, 109]. The particular version explained in the Section follows the formulation of Najafi [122, 123], and Ghorbanias [66], where the equations are recasted to obtained a convective wave equation. This formulation clearly separates the flow velocity fluctuations (u_i), surface velocities (v_i) and the free stream velocity (U_{0i}):

$$\left(\frac{\partial^2}{\partial t^2}+U_{0i}U_{0j}\frac{\partial^2}{\partial x_i\partial x_j}+2U_{0i}\frac{\partial^2}{\partial x_i\partial t}-c_0^2\frac{\partial^2}{\partial x_i\partial x_i}\right)(H(f)\rho')= \left(\frac{\partial}{\partial t}+U_{0i}\frac{\partial}{\partial x_i}\right)(Q_i n_i\delta(f))-\frac{\partial}{\partial x_i}(L_{ij}n_j\delta(f))+\frac{\partial^2}{\partial x_i\partial x_j}(T_{ij}H(f)), \tag{6.1}$$

where the subscript 0 refers to the undisturbed or free stream flow, f is the fictitious surface, H is the Heaviside function, δ is the Dirac delta function, and

$$Q_i=\rho(u_i+U_{0i}-v_i)+\rho_0(v_i-U_{0i}), \tag{6.2}$$

$$L_{ij}=P_{ij}+\rho u_i(u_j+U_{0j}-v_j), \tag{6.3}$$

$$T_{ij}=\rho u_i u_j-\sigma_{ij}+(p'-c_0^2\rho^2)\delta_{ij}, \tag{6.4}$$

$$P_{ij}=(p-p_0)\delta_{ij}-\sigma_{ij}. \tag{6.5}$$

The acoustic pressure can be obtained from the acoustic density fluctuation as $p'=c_0^2\rho'$ on the far field (where $\rho'/\rho_0 << 1$), which is the difference in pressure $p'=p-p_0$. The right-hand side of (6.1) represents the different source terms for the FWH noise model: the loading, thickness, and quadropole terms. In this work, quadropoles are neglected, and thus its contribution to the viscous stress tensor.

For unbounded domains, the convective wave equation can be solved using the integration and convolution of the three-dimensional free-space Green's function [29]:

$$G(\mathbf{x},t;\mathbf{y},\tau)=\frac{\delta(\tau-t+R/c_0)}{4\pi R^*}, \tag{6.6}$$

where x and y are the receiver and source position, t and τ are the receiver and source time, R^* represents the amplitude radius, R is the phase radius, $r=|\mathbf{r}|$ is the geometric radius with $r_i=x_i-y_i$ being the position vector between the receiver and the source (see [60] for a more detailed explanation), and are defined as:

$$R^*=\frac{1}{\gamma}\sqrt{r^2+\gamma^2(M_{0i}r_i)^2}, \tag{6.7}$$

$$R=\gamma^2(R^*-M_{0i}r_i), \tag{6.8}$$

$$\gamma^2 = \frac{1}{1-|\mathbf{M_0}|^2}. \tag{6.9}$$

All cases in this Chapter correspond to a wind tunnel scenario, which is a stationary (permeable or solid) surface ($v_i = 0$) subjected to constant flow in the positive x direction ($U_{0i} = Constant \neq 0$). As a result, many terms are cancelled and the two components of the acoustic pressure fluctuation are solved:

$$p'(\mathbf{x},t) = p'_T(\mathbf{x},t) + p'_L(\mathbf{x},t), \tag{6.10}$$

$$4\pi p'_T = \int_S \left[\frac{(1-M_{0i}R_i)\dot{Q}_i n_i}{R^*}\right]_{\tau_e} dS - \int_S \left[\frac{U_{0i}\hat{R}^*_i Q_i n_i}{R^{*2}}\right]_{\tau_e} dS, \tag{6.11}$$

$$4\pi p'_L = \int_S \left[\frac{\dot{L}_{ij} n_j \hat{R}_i}{c_0 R^*}\right]_{\tau_e} dS + \int_S \left[\frac{L_{ij} n_j \hat{R}^*_i}{R^{*2}}\right]_{\tau_e} dS, \tag{6.12}$$

where the radius vectors are the partial derivative of the radius quantity and are obtained as:

$$\hat{R}^*_i = \frac{r_i + \gamma^2 (M_{0j} r_j) M_{0i}}{\gamma^2 R^*}, \tag{6.13}$$

$$\hat{R}_i = \gamma^2 (\hat{R}^*_i - M_{0i}). \tag{6.14}$$

The subscript τ_e indicates that the integrals are calculated at the emission retarded time, which is calculated using (6.15) (see [54] for more details), being R the phase radius defined in (6.8):

$$\tau_e = t - \frac{R}{c_0}. \tag{6.15}$$

For wind tunnel scenarios, the retarded time can be calculated analytically, as oppose to more complex configurations such as bodies in arbitrary motion, where this calculation has to be done numerically. To obtain a complete time history of the acoustic pressure fluctuation, two possible algorithms can be used, based on the definitions of emission time and observer time [122]. In the first one, known as the related-time algorithm [18], the *observer* time is kept constant, along with its position, calculating the emission time, mainly performed by numerical root finding [19]. The second, called the time-dominant algorithm [18], where at each

numerical time step (i.e. the *emission time*), the *receiver* time is calculated, enabling a time advancing approach. We use the latter algorithm in this Section as it requires to load the CFD of each time step only once.

A different approach to the described solution of the FWH analogy is to use a frequency domain approach, as opposed to the time one. For this, the wave equation (6.1) is converted to the frequency domain using a Fourier transform. An appropriated Green function is used to solve the integrals, similar to (6.6). More detail can be found at [2, 108, 109, 174, 175].

All the integrals of (6.11) and (6.12) are evaluated numerically at each h-mesh face of the FWH surface, using the high-order (p-mesh) discretisation at the face, which is inherently related to the Gauss (or Gauss-Lobatto) nodes. A difficulty that arises here is that for each point on the surface, we have a different value of the emission retarded time, creating a non-uniform distribution of the acoustic pressure, i.e. the sound emitted at a certain time (numerical simulation time) will arrive at a different time for each nodal point to the observer. To handle this, a linear interpolation of the face acoustic pressure history (for each receiver) is performed before adding the contribution of each of the faces.

6.3 Validation

In this Section we validate the FWH implementation described in this chapter with test cases, comparing both of them with reference results either analytical or DNS simulations. The former is an analytical model for a monopole immersed in a moving medium, while the latter is a cylinder in constant flow.

6.3.1 Monopole in moving medium

A classic validation case to validate the FWH implementation is the stationary monopole in a moving medium [108], that is to say in wind tunnel condition. The case consists in an analytical expression for the simple harmonic velocity potential flow as:

$$\phi(\mathbf{x},t) = \frac{A}{4\pi R^*}\left[jw\left(t - \frac{R}{c_0}\right)\right], \tag{6.16}$$

where ω is the frequency of the monopole, $j = \sqrt{-1}$, and R^* and R are the acoustic radius defined in (6.7) and (6.8), respectively. The flow variables are then computed as

$$
\begin{aligned}
u_i(\mathbf{x}, t) &= \mathfrak{Re}\left[\frac{\partial \phi(\mathbf{x}, t)}{\partial x_i} \right], \\
p'(\mathbf{x}, t) &= \mathfrak{Re}\left[-\rho_0 \left(\frac{\partial \phi}{\partial t} + U_{0i} \frac{\partial \phi}{\partial xi} \right) \right], \\
\rho'(\mathbf{x}, t) &= \frac{p'}{c_0^2},
\end{aligned}
\tag{6.17}
$$

where $\mathfrak{Re}[\,]$ denotes the real part of the expression. The monopole tested has a reference length $\ell = 1$, an amplitude 1.0, an angular frequency $\omega = 10\pi$, and is centred at the origin $x_0 = [0, 0, 0]^T$.

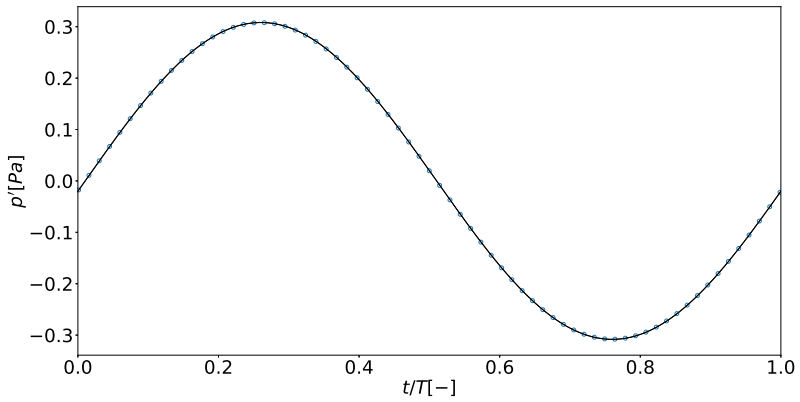
Two conditions are considered, the first one with a free-stream Mach number $M_0 = 0.5$ aligned with the x axis. The second one, with a free-stream velocity not aligned with any axis, equivalent to a case with a general angle of attack, such that the Mach vector is $\mathbf{M} = [0.5, 0.5, 0.5]^T$. In both cases, the analytical values of (6.17) are calculated on the faces of a cube of length ℓ and are used as input to the FWH integrals, using the permeable surface formulation.

The results of the first condition are shown in Figure 6.2, for the acoustic pressure time history at a location of 20ℓ upstream of the monopole and the root mean square of the pressure for observers located in a radius circle 20ℓ. Excellent agreement with the analytical solution is obtained for all the times and all the positions.

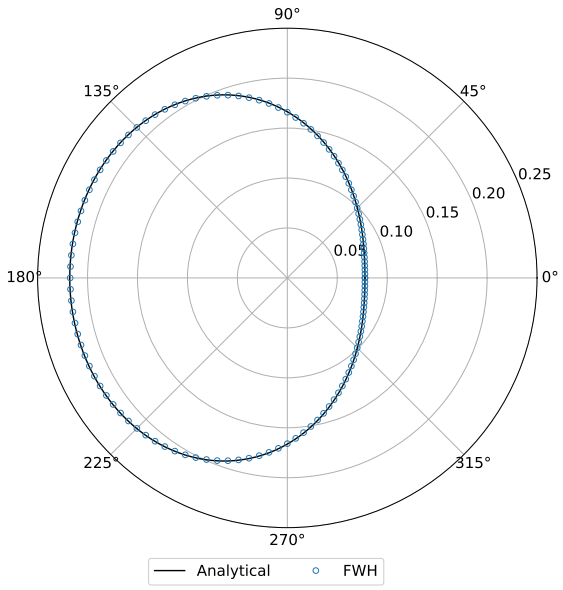
In addition, the same results at the same positions, for the second case, can be seen in Figure 6.3. In this case, the angle of the flow clearly affects the shape of the directivity. Regarding the FWH results, a good agreement is found with the analytical solution, with little error for receivers near 225°.

6.3.2 Cylinder in moving medium

Another classical study case is the sound generated by a cylinder in an external flow, in this case at a $\mathrm{Re} = 200$ based on the diameter of the cylinder at a $M_0 = 0.2$. In this test case we solve the flow with the compressible NS equations and use the



(a)

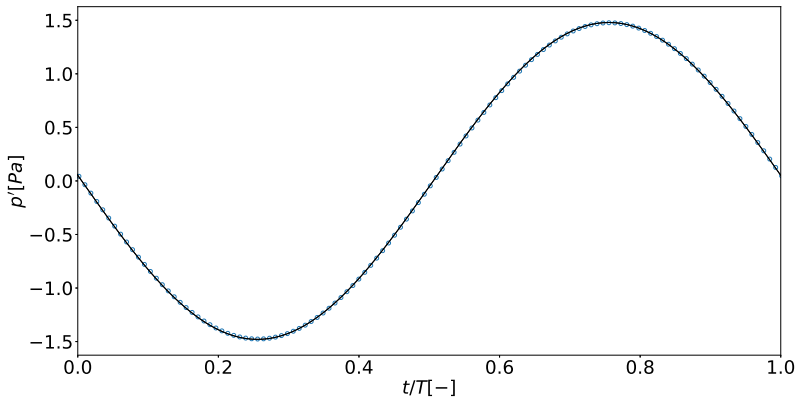


(b)

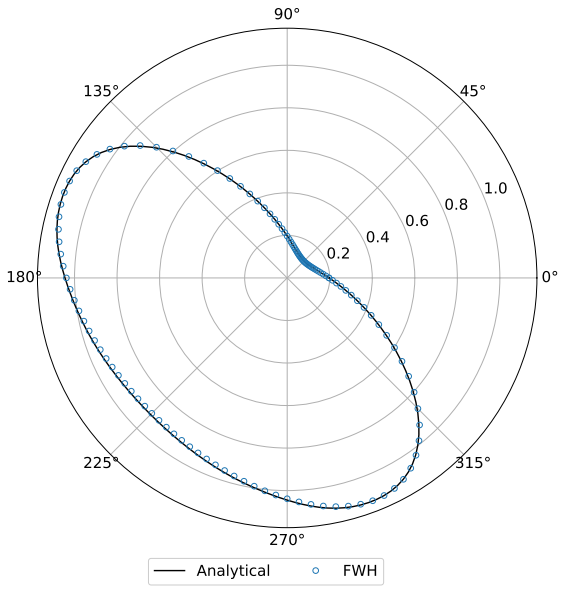
Figure 6.2: Comparison between analytical and FWH acoustic pressure of the stationary monopole in a moving medium [108] with $\mathbf{M} = [0.5, 0, 0]^T$. a) Time history of the pressure at $[-20\ell, 0, 0]^T$. b) RMS of the pressure at $r = 20\ell$.

results to calculate the acoustic pressure using the FWH analogy, with the aim of validating the coupling of the DGSEM solver and the CAA hybrid approach.

The computational domain for the NS solution corresponds to a box of length $[220D, 200D, 1D]^T$ with the centre of the cylinder located at $100D$ of the left boundary in the x direction and in the middle of the y direction. The h-mesh is non-conforming and hexahedral, with more refinement near the cylinder walls and in



(a)



(b)

Figure 6.3: Comparison between analytical and FWH acoustic pressure of the stationary monopole in a moving medium [108] with $\mathbf{M} = [0.5, 0.5, 0.5]^T$. a) Time history of the pressure at $[-20\ell, 0, 0]^T$. b) RMS of the pressure at $r = 20\ell$.

its wake, as shown in Figure 6.4. It consists of 4806 elements and is enriched with a polynomial of order 3 in all directions. The boundary conditions are set exactly as in Sections 5.2 and 5.3, with an angle of attack of 0° such that the flow goes in the x direction. We use Gauss nodes and no turbulence modelling of any kind since the flow has a laminar regime. To complete the formulation, we use the Roe Riemann solver and the BR1 scheme.

The results of the NS simulation is a time-dependent solution, where a vortex

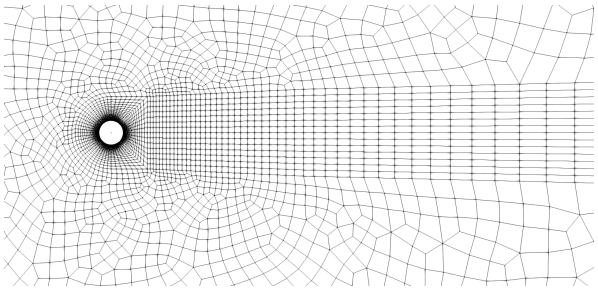
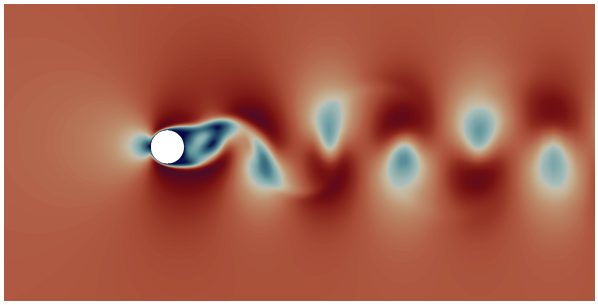
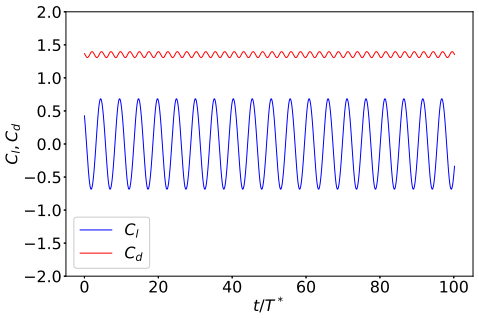


Figure 6.4: Zoom of the h-mesh used to simulate the cylinder.

shedding appears in the wake of the cylinder, as seen in Figure 6.5a. A statistically converged solution is obtained, with the oscillatory behaviour shown in the lift ($C_l = L/(\frac{1}{2}\rho U_0^2 S)$) and drag ($C_d = D/(\frac{1}{2}\rho U_0^2 S)$) coefficients, as shown in Figure 6.5b, obtaining a frequency of $S_t = 0.195$.



(a) Instantaneous velocity magnitude.

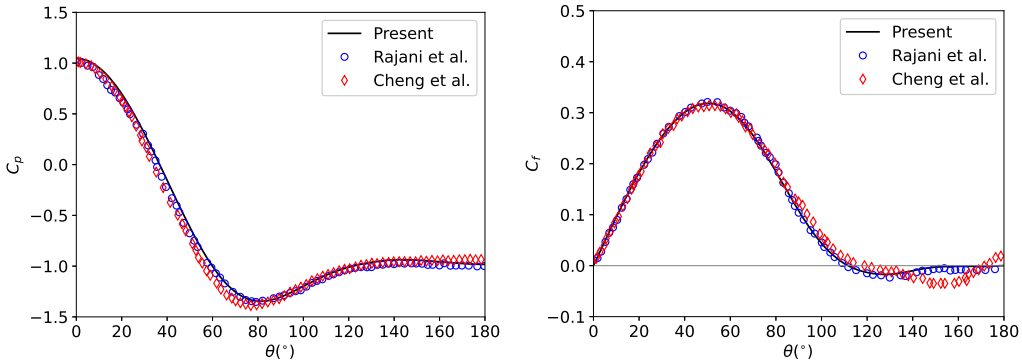


(b) Evolution of the lift and drag coefficients.

Figure 6.5: Results of NS simulation of flow over a cylinder at Re = 200 and $M_0 = 0.2$.

To validate the precision of the NS solution, we gather the results for 40 vortex periods and calculate the time averaged pressure and viscous force on the cylinder wall. We compared these values in the form of the pressure ($C_p = (p - p_0)/(\frac{1}{2}\rho U_0^2)$) and skin friction ($C_f = \tau_w/(\frac{1}{2}\rho U_0^2)$) coefficients against the computational results obtained by [33, 132], shown in Figure 6.6. Very good agreement is found in both coefficients, with little disagreement around 50°.

The FWH analogy is obtained using the solid formulation, using the wall of the cylinder as the integration surface. The conserved variables and its correspondent time derivative are saved during the same period of time as for the averaged calculations, and the pressure and pressure derivative are calculated from them. Since the flow over the cylinder at this Re has a laminar and 2D behaviour, straight forward integration does not produce good results. In this case we reproduce the solution



(a) Pressure coefficient. (b) Skin friction coefficient.

Figure 6.6: Time averaged coefficients on the cylinder wall. Current results compared to the reference values of [33, 132].

in the span direction up to $20D$ (compared to the simulated $1D$) as the periodic boundary conditions in the span direction represents this behaviour, following the recommendations by [17].

The directivity of the acoustic sound pressure level (SPL) in the far field (at $r = 20D$) can be seen in Figure 6.7. The expected dipole shape opened in the normalwise direction is obtained. Additionally, the results obtained with the FWH analogy are compared with two reference cases from the literature for the same flow conditions and observer positions. The first one was obtained by [146] using a split technique of the acoustic, in a similar way to the LEE and the APE, while the second one was obtained by [33] solving the APE. Good agreement is found, capturing the shape and general values, with minor differences at 140° and in the pure wake of the flow, $-10°$ to 10°, which is expected, as no quadropoles are considered and the surface for the integrals is the surface of the cylinder itself, so no effects of the wake are taken into account.

6.4 Airfoil acoustic computation

In the last section we use the FWH coupled to the NS solver to get the acoustic field of a case of classical study, the sound generated by an airfoil in an external, where noise is scattered by the trailing edge. We use the flow results from Section 5.3, where the acoustic is also calculated using the direct approach, so that we can compare both. The case is the NACA 0012 at $\mathrm{Re} = 1 \times 10^5$ based on the airfoil chord,

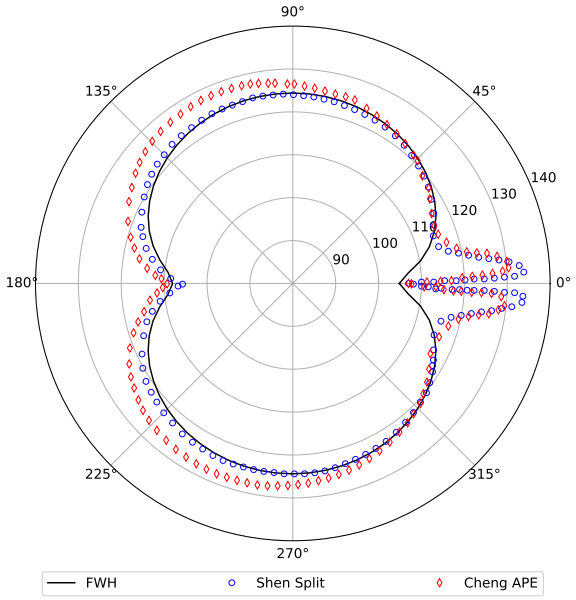


Figure 6.7: Directivity of the SPL (in dB) at $r = 20D$ for the flow over a cylinder obtained with the FWH acoustic analogy. Results compared with reference values of [33, 146].

and $M_0 = 0.4$.

We compute the acoustic pressure in the same points as did for the DNC, that is, in a single point located at $[x, y]/C = [0.5, 0.5]$, and in a circle of radius $2C$ with the centre at the trailing edge. The NS results at the surface of the airfoil are gathered at samples of $0.02T^*$ for $36T^*$, allowing good resolution of both low and high frequencies. The procedure for calculating the FWH is the same as that used in Section 6.3.2, using the solid formulation with the airfoil wall as the integration surface. The post-process of the acoustic pressure signal is the same as in the DNC, for comparison purposes.

6.4.1 Polynomial convergence

First, we compare the FWH results alone, emphasising in the convergence of the acoustic pressure as the polynomial of the NS simulation is increased. We start with the single point in the far field, comparing the PSD for all polynomial orders, as shown in Figure 6.8. A similar trend is obtained for all polynomial orders, but for $p = 1$, as discussed in the DNC results, the resolution is not enough even for

the flow hydrodynamics. The spectra shows a broadband behaviour with constant decay and peaks that vary in magnitude with all polynomial orders.

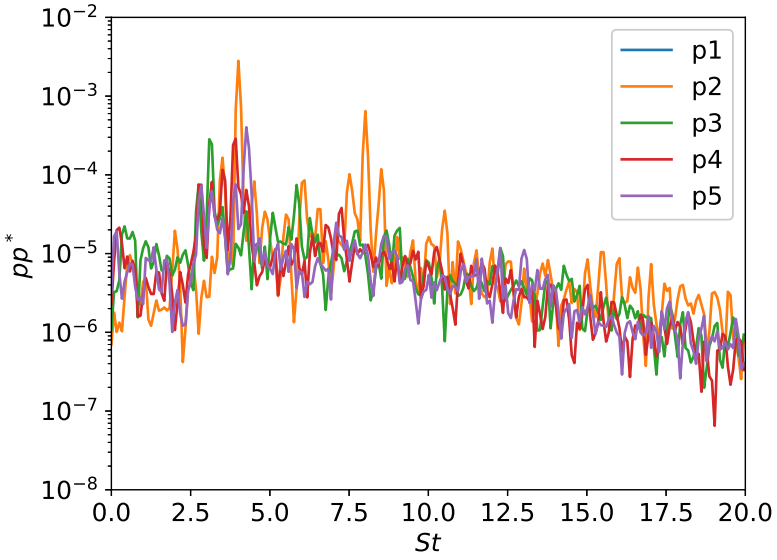


Figure 6.8: Polynomial convergence of the PSD of the acoustic pressure of a point located in $[x, y]/C = [0.5, 0.5]$ calculated with the FWH analogy.

For the directivity of the OSPL presented in Figure 6.9, more variability is found compared to the direct case. The general shape is correctly captured for polynomials 3 to 5, with differences of about 2 dB appearing at different angles.

6.4.2 Comparison with direct computation

To compare both approaches of sound computation, we present the results of the higher polynomial order, $p = 5$, for the same variables. Figure 6.11 shows the PSD at the single point. Similar behaviour is found at low frequencies, with relatively good agreement with the prediction of the peaks, namely, the frequencies and the values of the peak. After a Strouhal of about 5, both predict a broadband behaviour, with constant decay, but with a very different slope. The DNC decays much faster than the FWH, which can be due to numerical dissipation of the propagation using the NS equations directly, as the h-mesh starts to be coarser as we move from the airfoil wall, while the FWH is independent of the distance.

With respect to the directivity, presented in Figure 6.12, more differences can be found. While both predict a tilted dipole-like shape, the FWH has clearer loves in the upstream regions. In addition, the wake love is completely ignored in the

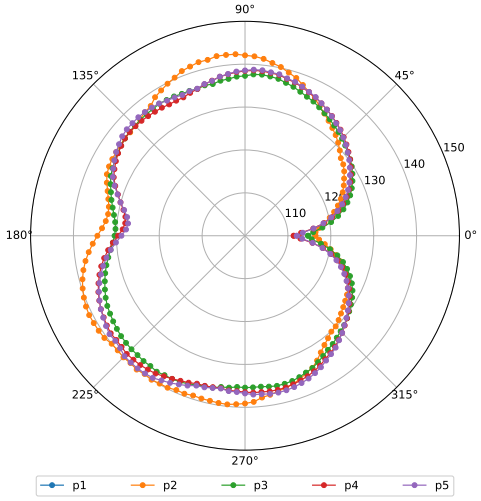


Figure 6.9: Polynomial convergence of the OSPL directivity (in dB) at $r = 2C$ calculated with the FWH analogy.

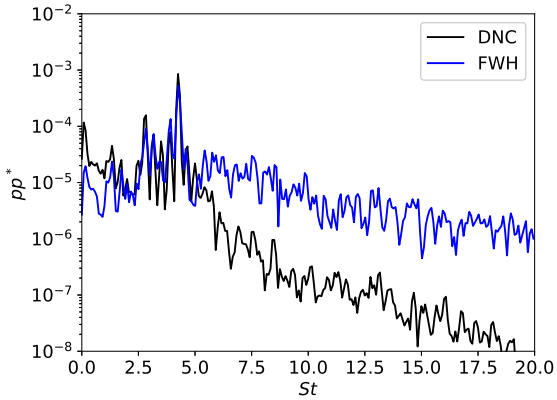


Figure 6.10

Figure 6.11: Comparison of the PSD of the acoustic pressure of a point located in $[x, y]/C = [0.5, 0.5]$ calculated with the direct and the FWH analogy.

FWH results, as the solid formulation does not take into account the values at the wake (to include it, the permeable formulation with the surface enclosing the most important wake region can be used).

To finalise, we compare the convergence of both methods using the OSPL of the single point receiver in the far field, comparing the result of each polynomial order with the most refined, $p = 5$. The results are shown in Figure 6.13 in terms of the difference of OSPL vs. the degrees of freedom of the NS simulation. Spectral convergence is found for both approaches, showing the expected properties of the

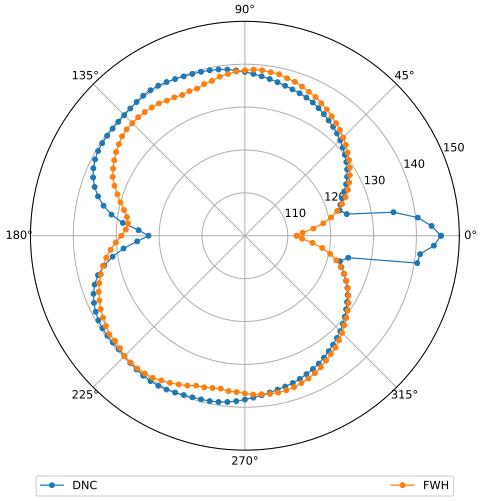


Figure 6.12: Comparison of the OSPL directivity (in dB) at $r = 2C$ calculated with the direct and the FWH analogy.

DGSEM method but for more complex and sensible variables, such as the acoustic pressure. The FWH shows a higher convergence, as the mesh in the far field does not influence it.

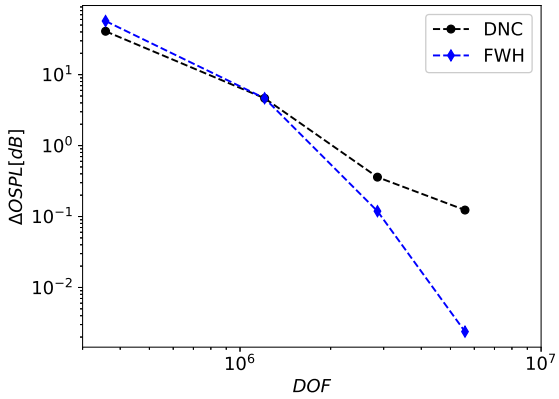


Figure 6.13: Polynomial convergence of the OSPL of a point located in $[x, y]/C = [0.5, 0.5]$ calculated with both, direct and the FWH analogy.

6.5 Summary

In the current Chapter we have presented the hybrid methods that allows performing CAA simulations in two steps, decoupling the flow solver from the acoustic one.

We have chosen the Ffowcs-Williams and Hawkings acoustic analogy as a method to compute the aeroacoustic results. We used the results of the compressible NS solver at a selected surface as input for the FWH calculations.

We have implemented the FWH solver using its integration surface as a collection of faces of the h-mesh used in the DGSEM solver, allowing us to use the same Gauss (or GL) nodes for computing the numerical integrals. We validated the implementation with two test cases, one the case with analytical solution, a monopole in an uniform velocity field and the second the a cylinder subjected to an external flow.

Finally we solved the aeroacoustic of an airfoil with the FWH analogy and compared with the results of using the direct approach by solving the compressible NS equations with the DGSEM method. Some differences are found from both approaches, while the general behaviour is well captured. In addition, both methods have good convergence properties with polynomial refinement.

Chapter 7

Amiet's Model for Leading and Trailing Edge

Contents

7.1 Introduction **85**
7.2 The Amiet model for leading edge noise **86**
7.3 The Amiet model for trailing edge noise **87**
7.4 Wall pressure spectra models **88**
7.4.1 Boundary layer characteristics 90
7.5 Numerical results **91**
7.6 Summary **93**

7.1 Introduction

In Chapter 5 we started with DNC simulations, where high-fidelity simulations are used to predict the generation and propagation of noise until the receiver location. Then, in Chapter 6 we reduced the fidelity using the FWH acoustic analogy to propagate the acoustic to the far field, while the computation of sources remains high-fidelity. In this Chapter we continue this reduction of fidelity, but in plenty steps. The motivation for doing this is that it is possible to predict the noise of a whole wind turbine, using only static airfoil simulations, with some corrections, as

will be presented in Chapter 9. However, the number of simulations required to do this kind of calculations is considerable, making it infeasible using the strategies previously used, especially if time-dependent data of the turbine are used. Therefore, a lower-fidelity method is necessary that can predict stationary airfoil noise with enough precision, but with very high speed and efficiency.

This method must include the main sources of noise of a wind turbine, which have been identified as trailing-edge (TE) and leading-edge (LE) noise [127]. Trailing-edge noise, also known as airfoil self-noise, is caused by the interaction of the turbulence present within the boundary layer with the airfoil trailing edge. Therefore, it is found in all operating conditions and is the minimum amount of noise produced by a wind turbine. Leading-edge noise is caused by the interaction of inflow turbulence with the leading edge of the blades and depends on atmospheric conditions.

In the current chapter we will develop this methodology for predicting LE and TE noise using the semi-analytical Amiet's theory, along with several other semi-empirical models used to calculate its inputs. The theory assumes a flat plate geometry with infinitely small thickness, a stationary observer, and a uniform free-stream condition along the span. Finally, it is validated using a test case consisting of a NACA0012 airfoil with fully turbulent boundary layer.

7.2 The Amiet model for leading edge noise

In this Section we introduce the Amiet model of leading edge [4] to calculate the noise emitted by the interaction of the free-stream turbulence with the leading edge of the airfoil. The power spectral density (PSD) of the far field at the mid-chord and midspan is defined as for an observer located at $[x_o, y_o, z_o]T$ (chordwise, spanwise, and normalwise, respectively) is:

$$S_{pp|\mathrm{LE}} = \left(\frac{\omega z_0 \rho c}{c_o R^{*2}} \right)^2 \pi U_0 d \left| \mathscr{L} \right|^2 \Phi_{ww}, \tag{7.1}$$

where c and d are the chord and span of the airfoil respectively, ω is the angular frequency used to evaluate the PSD, c_0 is the sound velocity, U_0 is the mean velocity of the free stream, R^* is the amplitude, corrected by the flow, the radial distance defined in (6.7), Φ_{ww} is the 2D perpendicular-to-the-wall velocity spectrum and $\mathscr{L}$ is the aeroacoustic transfer function for subcritical or supercritical gusts. $\mathscr{L}$ ac-

counts for the scattering effect of the LE and the backscattering of the TE, based on the conclusions of[21]. The far-field noise is calculated at the reference point used in the source power integration technique. As the coordinate reference system is located at midchord and midspan, an additional translation subtracting $c/2$ in the x_o-axis is conducted for the LE noise prediction.

One of the main parameters of (7.1) the velocity spectrum (Φ_{ww}). The most common way to calculate it is using the von Kármán turbulence spectrum:

$$\Phi_{ww} = \frac{4}{9\pi}\frac{u_{rms}^2}{k_e^2}\frac{(k_x/k_e)^2}{[1+(k_x/k_e)^2]^{7/3}}, \tag{7.2}$$

where $k_x = \omega/U_0$ is the chord-wise aerodynamic wavenumber, u_{rms} is the root mean square of the turbulent velocity fluctuations in the free-stream (related to the turbulent intensity), and k_e is the wavenumber scale of the largest eddies [67], calculated as:

$$k_e = \frac{\sqrt{\pi}}{L}\frac{\Gamma(5/6)}{\Gamma(1/3)}, \tag{7.3}$$

where L is the integral length scale of the velocity in the free-stream, and Γ is the gamma function.

7.3 The Amiet model for trailing edge noise

This section introduces the computational models used to compute the far-field noise caused by the trailing edge of the airfoil, mainly being Amiet's theory for TE [5]. The theory calculates the far-field acoustic pressure spectrum using the wall pressure wavenumber-frequency spectral density in the vicinity of the trailing edge as input. It is assumed that there is a large span, a stationary observer and airfoil, and a uniform flow, and that the boundary layer turbulence is convecting over the trailing edge as a frozen pattern, i.e., the turbulence is not affected by the discontinuity of the trailing edge. The initial method defines an aeroacoustic transfer function to calculate the far-field noise power-spectral density when the near-field is modeled. Later, the acoustic transfer function for both noise sources was extended to consider the back-scattering due to the finite chord length and the effect of subcritical and supercritical gusts [41, 135]. The far-field power spectral

density of an airfoil for an observer perpendicular to the trailing edge at midspan ($y_o = 0$) [157], and with a coordinate system with its origin at the TE as:

$$S_{pp|\mathrm{TE}} = \left(\frac{\omega b z_0}{2\pi c_o R^{*2}}\right)^2 \frac{d}{2} |\mathscr{L}|^2 l_z \Phi_{\mathrm{pp}}, \tag{7.4}$$

where b is the semichord, used to nondimensionalize the wave numbers, Φ_{pp} is the wall-pressure spectrum (which is discussed in Section 7.4) and l_y is the spanwise correlation length which is related to the size of the vortices in the spanwise direction, and is calculated as proposed by Corcos [39] as:

$$l_y = \frac{b_c U_c}{\omega}, \tag{7.5}$$

where U_c is the convection velocity, assumed as $0.7U_0$, and b_c is the Corcos' constant equal to 1.47 [157].

In 7.4, $\mathscr{L}$ is the airfoil response function proposed by [5] which is the transfer between hydrodynamic wall pressure fluctuations caused by the turbulent boundary layer to acoustic waves in the far field. Amiet considered a flat plate, therefore, $\mathscr{L}$ is constant among the different airfoils. We follow the work of [135] to calculate $\mathscr{L}$ which considers the backscattering effect of the leading edge.

7.4 Wall pressure spectra models

The wall pressure spectrum in the vicinity of the trailing edge is comparable to the measurements of a sensor located on the airfoil surface and is related with the generation of acoustic pressure waves from the attached turbulent boundary layer on the airfoil. This is the reason why the wall-pressure spectrum is the only quantity in 7.4 that is different for each airfoil facing the same inflow conditions. This acoustic pressure waves are caused by velocity fluctuations related to the small structures near the airfoil wall and the larger structures in the outer part of the boundary layer [67]. The smaller structures scale with viscous length (u_τ/ν) and are responsible for the high frequency range of the wall pressure spectrum, whereas the larger turbulent structures scale with the boundary layer thickness (δ) and are responsible for the low frequency range of the wall pressure spectrum. The mid-frequency range scales with both types of structures.

The wall pressure spectrum can be calculated with high fidelity using LES or iLES formulation, by sampling the evolution in time of the wall pressure. However, to follow the intention of using lower fidelity models, other options can be consider, such as using semi-empirical models. Several models have been proposed, based on experimental measurements of flat plates or airfoils with pressure gradient [31, 69, 76, 81, 102, 137]. Other model is the one proposed by [14] which is based on physical analysis by solving the Poisson's equation, which governs the relationship between the velocity fluctuations across the boundary layer and the wall-pressure fluctuations in the airfoil wall. The model proposed by [14] was later extended by [128] and is now known as the TNO-Blake model. The TNO-Blake model incorporates more physics and takes into account several turbulence quantities, and not only integral quantities as in semi-empirical models. For this reason, we have selected this model to calculate the wall pressure spectrum that will be an input to the PSD of the TE noise.

The TNO-Blake model is proposed based on the solution of the Poison equation that results from the divergence of the Navier-Stokes equation simplified by the continuity equation. The model can be applied to calculate the wall-pressure spectrum close to the trailing edge, however, the turbulence quantities are calculated assuming that the discontinuity of the trailing edge does not affect the turbulence. Furthermore, the model assumes that the turbulent pressure and velocity field are spatially homogeneous and stationary on time. The wall pressure spectrum can be calculated in the wavenumber-frequency domain by applying the Fourier transform in time-space Fourier transform. Therefore, the wall pressure spectrum would depend on the wavenumber in the chordwise direction (κ_x) and spanwise direction ($ł_z$). We follow the TNO-Blake model extension proposed by [157], which also considers the anistropy of the turbulence by incorporating the stretching parameters, calculated as:

$$\Phi_{pp} = \frac{4\pi\rho^2}{l_y}\int_0^{\delta} \Lambda_{z|vv}(z)U_c(z)\left[\frac{\partial U(z)}{\partial z}\right]^2 \frac{u_{rms,z}(z)}{U_c^2(z)}\phi_{vv}(k_x,z)e^{-2k_x z}dz. \tag{7.6}$$

where δ is the thickness of the boundary layer, $\Lambda_{z|vv}(z)$ is the integral length scale across the boundary layer in the z direction, i.e., in the direction of the boundary layer, perpendicular to the airfoil wall. $U_c(z)$ is the convection velocity across the boundary layer, which is assumed to be between 0.6 and 0.8 the velocity and the stream-wise velocity. $U(z)$ is the velocity at each position along the boundary

layer, $u_{rms,z}$ is the velocity fluctuation in the z direction. ϕ_{vv} is the turbulence spectrum of the velocity fluctuations in the z-direction. Plenty of this values depend on the boundary layer mean flow characteristics and turbulence quantities across the boundary layer, which are presented in the next section.

7.4.1 Boundary layer characteristics

To calculate the parameters of 7.6 related to the boundary layer, a mean flow solution on the airfoil is needed, as well as some complementary models and definitions. This main flow can be obtained with a CFD solver, using for example a steady state RANS, or with other methods created specifically for static airfoils. We have selected XFOIL [51] as the numerical tool to obtain the boundary layer characteristics. XFOIL is a viscous-inviscid iterative software code that does not require any prior mesh preparation. The inviscid pressure distribution is modeled using a linear vortex strength distribution. Viscous effects and the development of the laminar-turbulent boundary layer are modeled using linear stability and integral boundary layer theory.

The boundary layer thickness is calculated using the expression proposed by [52], as:

$$\delta = \theta\left(3.15 + \frac{1.72}{H-1}\right) + \delta^*, \tag{7.7}$$

where δ^* is the boundary layer displacement thickness and θ is the momentum thickness, both of them are obtained directly from XFOIL results. The mean velocity across the boundary layer is modeled by the universal von-Kármán log of the wall coupled with the Coles' wake factor (Π_w) that accounts for the pressure gradient [38], as:

$$\begin{aligned}
\frac{U(z)}{u_\tau} &= z^+ && z^+ < 5 \\
\frac{U(z)}{u_\tau} &= \frac{1}{\kappa}\log\left(z^+\right) + B + \frac{2\Pi_w}{\kappa}\sin^2\left(\frac{\pi z}{2\delta}\right) && z^+ \geq 5 \\
\Pi_w &= 0.8\left(\frac{\delta^*}{\tau_w}\frac{\mathrm{d}C_p}{\mathrm{d}x} + 0.5\right)^{3/4}
\end{aligned} \tag{7.8}$$

where $\kappa = 0.38$ is the von Kárman constant, $B = 5$ is the level constant, $z^+ = zu_\tau/\nu$

is the non-dimensional distance from the wall, C_p the pressure coefficient, $\tau_w = \rho u_\tau^2$ is the local wall shear stress, being u_τ the friction velocity, calculated as:

$$u_\tau = \sqrt{0.5 U_0^2 C_f}, \tag{7.9}$$

where C_f is the local friction coefficient. The pressure and friction coefficients are obtained directly from XFOIL.

To summarise, the XFOIL outputs are used to calculate the inputs of the wall pressure spectrum related to the boundary layer, which, in turn, is used to predict the far-field noise produced by the airfoil.

7.5 Numerical results

In this Section we validate the methodology of trailing edge noise prediction using Amiet theory coupled with the TNO-Blake model and XFOIL, as presented in Sections 7.3 and 7.4. We chose a widely studied airfoil in the literature, the NACA0012 airfoil as a test case, comparing our results with those obtained in the literature. The airfoil is assumed to have a $0.4m$ chord and a $1m$ span. The far-field observer is located at $1m$ from the airfoil trailing edge at mid-span, i.e., $x = 0$, $y = 0$, and $z = 1$. The wall pressure spectrum is calculated at $x/c = 0.99$. The boundary layer transition is fixed at $x/c = 0.06$ on both sides. The angle of attack is fixed at 0°. The inflow velocity is assumed to be 56 m/s, which corresponds to a Reynolds number of 1.5×10^6 and a Mach number of 0.16. The number of panel nodes is set to 160 and the number of iterations to 1000 in the XFOIL simulation. The frequency resolution is 1 Hz and the far-field noise S_{pp} is calculated from 100 Hz to 10 kHz. Sound pressure level (SPL) is calculated at the observer location using (5.7), with p_{rms} obtained from the sum of the power spectral density (S_{pp} from (7.4)) from both, pressure and suction side, and multiplied by the frequency resolution.

Comparisons have been conducted with experimental results reported in [72] (results have been scaled to match the presented conditions) and with noise prediction using Amiet's theory coupled with the semi-empirical model proposed by [81] and RANS simulations [98]. Figure 7.1 shows the far-field noise spectrum in 1/3 octave for the predicted far-field using the methodology presented in this paper and in the literature.

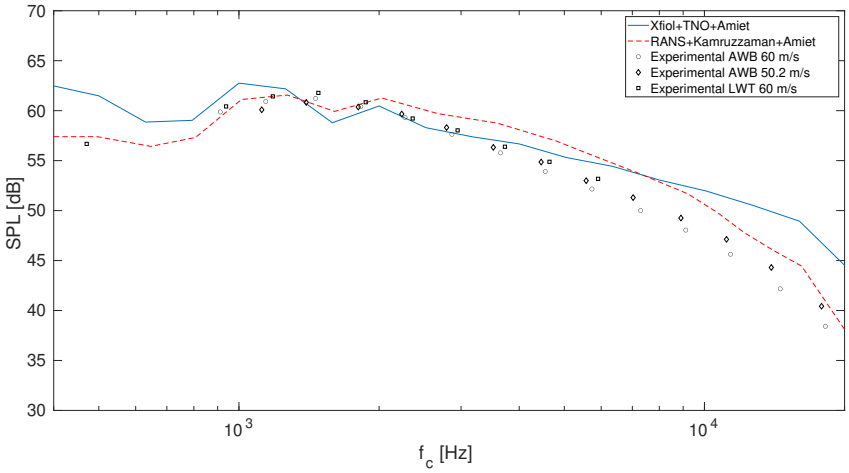


Figure 7.1: Far field noise comparison between current methodology, RANS simulations (from [98]) and experimental measurements (from [72]) for a NACA0012. SPL presented in 1/3 octave band.

Additionally, Table 7.1 shows the integrated pressure level of the spectrum for the same cases, between a frequency range of 1000 to 6300 Hz, i.e., the frequency range where all data is available. The results suggest that the applied methodology, i.e., XFOIL coupled with the TNO-Blake model and Amiet's theory, is appropriate to predict trailing edge noise and agrees with the literature showing less than 1 dB difference in the integrated spectra. The validation indicates that the proposed method provides results with comparable accuracy to more costly flow solvers, while being fast enough to be used for wind turbines, where multiple evaluations of the acoustic performance are needed for different airfoils along each of the blade, as is presented in Chapter 9.

Table 7.1: Comparison of the overall sound pressure level in the frequency range from 1000 to 6300 Hz. Values are presented in dB. (LWT: Laminar Wind Tunnel; AWB: Braunschweig Aeroacoustic Wind Tunnel)

Current work	RANS [98]	AWB [72], at 60 m/s	AWB [72], at 50.2 m/s	LWT [72], at 60 m/s
68.87	68.81	68.36	67.67	68.83

7.6 Summary

In this Chapter we have developed an methodology to calculate the main sources of noise in static airfoils, namely the trailing edge noise produced by an attached turbulent boundary layer and the leading edge noise produced by the interaction with the inflow turbulence. We establish this numerical framework by using Amiet's theory coupled with the TNO-Blake model for acoustics and the XFOIL solver for the aerodynamic variables that are inputs to this models. This methodology can be used in processes where quick evaluations are needed such as optimization, or to calculate the noise of a whole turbine, as will be done in Chapter 9.

We have tested the complete coupled methodology with a test case consisting in a turbulent flow in a NACA0012 airfoil, comparing with other methodology at similar level of fidelity and experimental values. Reasonable agreement is obtained, both in integrated quantities (OASPL) and in the frequency spectrum, where the main broadband behaviour is captured.

Part IV
Wind turbine modelling

Summary In this final part, we focus on wind turbine simulations, coupling different models with the DGSEM method, making possible the use of LES simulations to calculate the aerodynamic and aeroacoustic of the wind turbine. In Chapter 8 we introduce the actuator line method, that provides models to compute the forces on the turbine blades without the necessity of solving the physics around the actual geometry, providing an accurate method for the wake solution. In Chapter 9 we couple these aerodynamic results with the models of Part III to compute the aeroacoustic of the complete wind turbine.

Chapter 8

Wind Turbine Modelling

Contents

8.1 Introduction 97
8.2 The Actuator Line Model 99
8.3 AL in DGSEM 102
8.4 Numerical results 104
8.4.1 Wind turbine coefficients 106
8.4.2 Force distribution along the blade 107
8.4.3 Velocity decay along the blade 109
8.4.4 Wake velocity field 110
8.4.5 Turbulent Kinetic Energy 115
8.4.6 Tower and Nacelle 119
8.4.7 Computational Cost 121
8.5 Summary 122

8.1 Introduction

Solving all the small structures in a rotating wind turbine in the same level of detail as done for airfoils in Chapter 3 is impractical for most scenarios, due to is high computational cost. However, for some applications, this is not necessary. Indeed, to investigate the behaviour of wakes and their interaction, resolving the near blade

boundary layer is of secondary importance, and computational cost can be alleviated by modelling of the blades. Simulations using simplified turbines have been very useful to provide insights into the optimisation of wind turbine farm layouts, see [159].

Pioneering work by Sørensen and Shen [145, 153, 155] laid the foundation for the application of actuator line (AL) methods in the context of wind energy. This method represents the rotating turbine blades as lines of distributed force, known as actuator lines, which interact with the surrounding fluid. The actuator line captures the influence of the blades on the flow field, allowing for a computationally affordable representation of the rotor blades, yet capturing wakes accurately [164]. The validation of actuator line methods against experimental wind tunnel measurements and full-scale field data has shown that these techniques can provide accurate solutions at limited costs [36, 154]. Various turbulence models, such as large eddy simulation and Reynolds-averaged Navier–Stokes, have been integrated with actuator line methods to account for turbulence effects on both the wake structure and turbine performance [82, 177].

Integrating ALs with Large Eddy Simulations allows for the accurate representation of time-varying and turbulent effects, capturing intricate wake dynamics and tip vortices [34, 154, 164]. AL predictions for wake flow have been extensively validated against wind tunnel measurements in both single wind turbine and wind farm scenarios, demonstrating good agreement in both the near and far wake regions [49, 153, 158, 176]. When comparing actuator lines and blade-resolved simulations under nonsheared inflow conditions, [166], found that the actuator disk and AL produced wakes similar to resolved blades when the inflow was turbulent. However, under laminar conditions, resolving the blade boundary layer resulted in higher turbulence and eddy viscosity in the near wake, leading to significant differences in wake several diameters downstream [166].

In recent years, there has been a growing interest in incorporating actuator line models into high-order h/p solvers. These solvers offer several advantages, such as improved accuracy and better capture of flow features through higher-order polynomial approximations. By combining the actuator line method with high-order h/p solvers, the researchers aim to enhance the fidelity of wind turbine simulations and provide more accurate predictions of turbine performance metrics, including power production and aerodynamic loads. In the high order context (continuous formulations), a series of papers have adapted AL to high order finite differ-

ences [45, 46, 47] for a variety of turbulence models ranging from unsteady RANS to LES (modelled through a spectral vanishing viscosity models). Key questions on how to implement actuator lines in high-order methods using h/p meshes, such as DGSEM, remain and are the topic of this work. Namely, we study the effect of the polynomial order, the Gaussian smoothing parameter, and two ways to compute the forces on the actuator lines (averaging the velocity in each cell or using a weighted average forcing).

In the current Chapter, we study the application of actuator lines within the DGSEM method and focus on the numerical implementation and validation of the method against experimental data. The objective is to assess the accuracy, computational efficiency, and robustness of the high-order actuator line method. Through comparisons with experimental data, of a small wind turbine in a wind tunnel, we demonstrate the capabilities of the actuator line method in accurately capturing the complex flow phenomena around wind turbine blades. Additionally, we analyse the computational performance of the high-order h/p solver with actuator lines, and help us to provide guidelines for their implementation and use when simulating wind turbines.

8.2 The Actuator Line Model

In many of the research works, simulations of wind flows modelled using actuator lines have been performed with low-order solvers. For its extension to high-order solvers, we rely on the basis already established in the literature [153, 155, 164], from which certain concepts are generalised.

The model consists of simplifying the wind turbine blades into a line of points (actuator points) that represent the aerodynamic centres of the corresponding airfoil section of the blade. To incorporate the sectional blade forces, the ALM employs blade element theory, which calculates the aerodynamic forces and moments on each line element based on its local angle of attack, airfoil characteristics, and inflow conditions. These forces are then distributed to the surrounding flow in the computational domain, influencing the flow velocity and pressure. Thus, a rotating line is obtained with a series of point-wise source terms along its length.

The forces are calculated by introducing tabulated lift and drag coefficients for

different angles of attack and Reynolds numbers:

$$F_L = \frac{1}{2}\rho U_{rel}^2 S C_l, \qquad F_D = \frac{1}{2}\rho U_{rel}^2 S C_d, \tag{8.1}$$

where S is the sectional area, ρU_{rel}^2 is the local dynamic pressure and C_l,C_d are the sectional aerodynamic coefficients (e.g., 2D forces calculated from XFOIL). Note that we need to sample the velocity at the blade axis to impose the forcing, but this location may be influenced by the force itself. For this reason, various methods have been proposed to calculate the velocity (see, for example, [143]).

We follow a similar approach to [107] to compute the fluid kinematics around the blade sections. We start by considering the global inertial axes, $[x, y, z]^T$, where x represents the direction of the incident flow, y is perpendicular to the free-stream velocity and z is the local vertical axis, as shown in Figure 8.1.

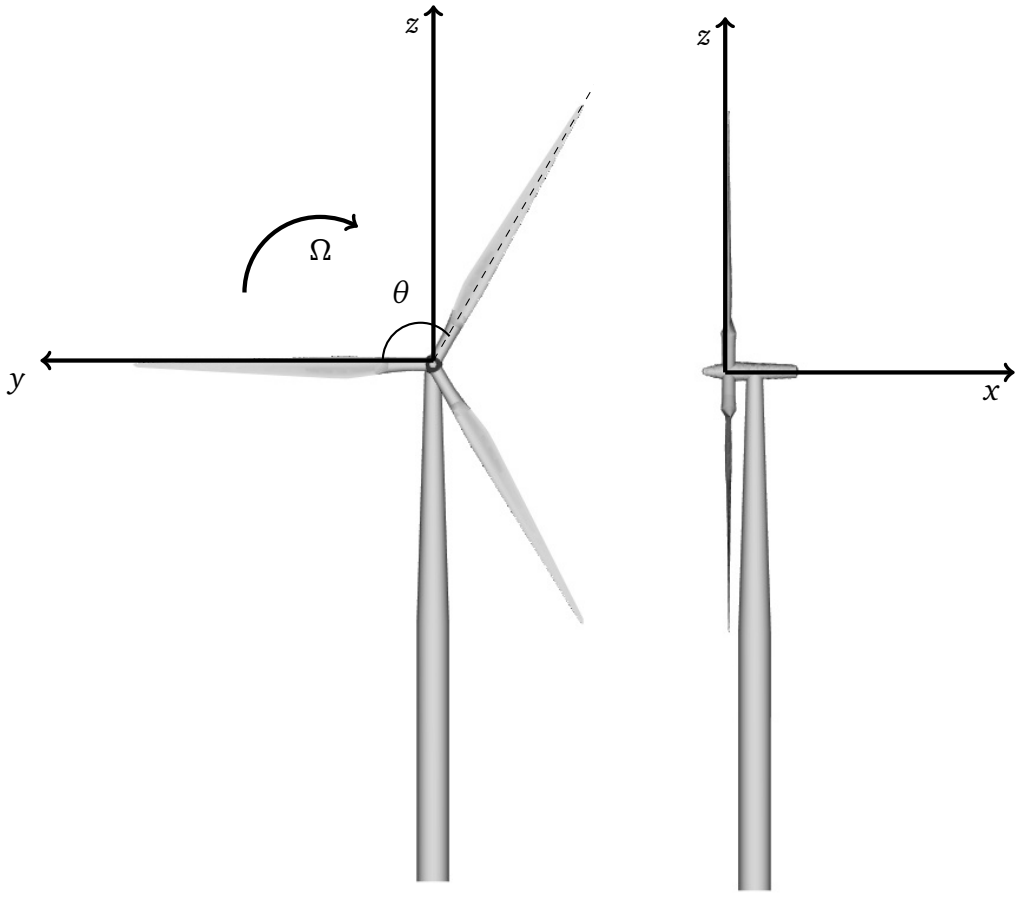


Figure 8.1: Reference frame

Considering the instantaneous flow velocity at a generic location such as $\mathbf{u} = [u_x, u_y, u_z]^T$, it can be converted to cylindrical coordinates using the reference frame. At any actuator point, the azimuthal component of its local velocity, U_θ, is a combination of two components of the fluid velocity and the rotational speed, calculated as:

$$U_\theta = \Omega r + u_y \sin\theta - u_z \cos\theta, \tag{8.2}$$

where Ω is the rotational speed of the actuator line, r is the radius of the actuator point, and θ is the azimuthal angle. Similarly, the angle of attack for each section is defined as

$$\alpha = \phi - \gamma; \quad \phi = \arctan\left(\frac{U_x}{U_\theta}\right), \tag{8.3}$$

where ϕ is the local angle of incidence, γ is the angle due to local twist and pitch of the airfoil, and $U_x = u_x$ is the axial component of the local velocity, as can be seen in Figure 8.2, along with all the velocities, angles, and forces.

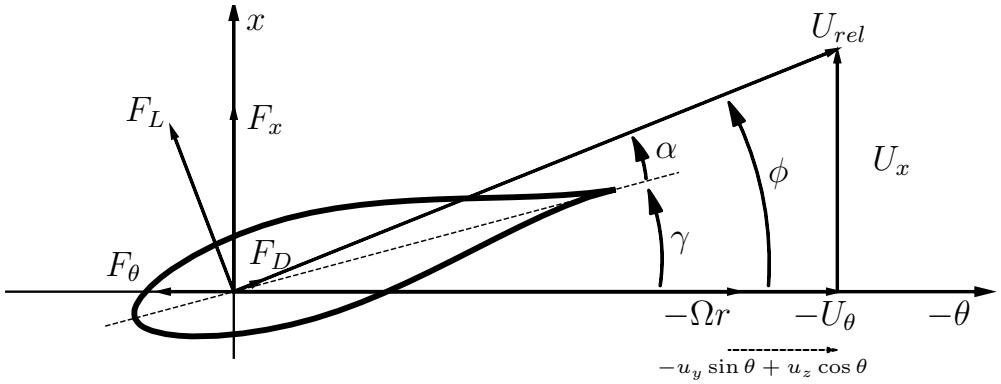


Figure 8.2: Cross-sectional blade section showing velocities and forces on the airfoil.

The relative velocity at the actuator point, $U_{rel} = \sqrt{U_x^2 + U_\theta^2}$, is obtained and the forces exerted by the blade section on the fluid are projected onto the global axes:

$$\begin{aligned} F_x &= -(F_L \cos(\phi) + F_D \sin(\phi)), \\ F_y &= (F_L \sin(\phi) - F_D \cos(\phi)) \sin(\theta), \\ F_z &= -(F_L \sin(\phi) - F_D \cos(\phi)) \cos(\theta). \end{aligned} \tag{8.4}$$

To avoid introducing point-wise forces into the solver, which can create numeri-

cal instabilities, each of these forces is spread across a volume so that it does not compromise the stability of the simulation. This is achieved by using a Gaussian projection,

$$\eta_\epsilon(d) = \frac{1}{\epsilon^3 \pi^{\frac{3}{2}}} e^{-\left(\frac{d}{\epsilon}\right)^2}, \tag{8.5}$$

where:

$$d = \sqrt{(x_{i,j,k} - x_a)^2 + (y_{i,j,k} - y_a)^2 + (z_{i,j,k} - z_a)^2}, \tag{8.6}$$

is the distance between an actuator point and an arbitrary node. The subscript a is used to indicate the actuator point, and the subscripts i, j, and k represent a Gauss or GL node.

Finally, the forces smeared by the Gaussian distribution are included as source terms in the spatially discretised Navier-Stokes equations, the $\mathbf{S}$ term of 2.33, calculated as:

$$\mathbf{S}(\mathbf{q}) = \eta_\epsilon \mathbf{F}. \tag{8.7}$$

where $\mathbf{F} = [0, F_x, F_y, F_z, 0]^T$ includes only the terms for the momentum equations.

8.3 AL in DGSEM

We now address some of the differences for the implementation in high-order schemes. First, we note that in (8.5) the parameter ϵ determines the width of the Gaussian projection function. If it is too small, it does not adequately address the issue of numerical divergence. However, if it is too large, the accurate representation of the rotor blades by the actuator line method will be compromised. Different approaches have been investigated to determine its optimum value in low order methods, such as $\epsilon = max\left[\frac{c}{4}, 4\Delta, \frac{c \cdot C_D}{2}\right]$, or more broadly,

$$\epsilon = k\Delta, \tag{8.8}$$

where k is a constant, usually within a certain range $k \in [1, 4]$ [114, 165], and $\Delta = (\Delta_x \Delta_y \Delta_z)^{\frac{1}{3}}$ represents the size of the cell used, c refers to the airfoil chord and C_D denotes the corresponding drag coefficient. In the context of high-order

DG solvers, there are $(p+1)^3$ Gaussian points contained within a cell. This enables one to redefine the parameter ϵ within each element based on the polynomial order employed in each element. We use the same approach as done in Chapter 3 to define the filter length of the element, averaging in each element with (3.6).

Second, we have pointed out in Section 8.2 that the velocity of the fluid, $stvecv$ used to calculate all the kinematics around the airfoil is influenced by the AL source itself. In the context of low-order volumes, using the value of the velocity at the computational node or interpolation from the neighbour ones might be enough. In the context of DGSEM, the most direct approach is using polynomial interpolation to retrieve this value, as we can find the relative position of the actuator point in the element reference space, as depicted in Figure 8.3. However, this can lead to numerical instabilities. In this Section, we propose and compare two methodologies, named AL1 or averaged velocity and AL2 or weighted sums.

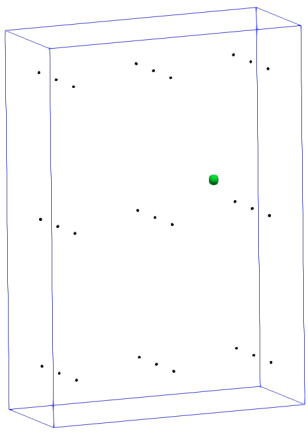


Figure 8.3: Schematic of the actuator point in a cell with its correspondent Gauss nodes, employing p=2.

In the AL1 method, at every time step the positions of all actuator points of the rotor are updated. For each actuator point we find the element of the mesh that contains it, and the conservative state vector of all the nodes contained in this cell are then averaged,

$$\bar{\mathbf{q}} = \frac{1}{NDOF} \sum_{n=1}^{NDOF} \mathbf{q}_n^{eN}, \tag{8.9}$$

and then is used to compute the flow velocity for the specific actuator point. This

procedure is the equivalent of converting the solution of the element into a first-order one. In the way, we avoid the high order frequencies that are present in the real solution to calculate the local variables of the actuator point.

For the AL2, we start with a procedure similar to that of the previous method, where at each time step the position of all actuator points is updated. However, the main difference lies in the fact that instead of projecting the same value of the state vector $\mathbf{q}_t$ onto the nearby nodes, each node contributes to the aerodynamic forces with its own local variables. These variables are scaled using the projection function η_d. Furthermore, instead of summing the contributions of all nodes to the force generated by the actuator point, a weighted average is performed with respect to distance for calculating the axial and tangential forces as below:

$$\overline{f}_j = \frac{\sum_{i=1}^{N} \eta_{ji}(d) \cdot f_i}{\sum_{j=1}^{N_a} \sum_{i=1}^{N} \eta_{ji}(d)} \tag{8.10}$$

where $\eta_{ji}(d)$ represents the Gaussian projection from the actuator point j to node i, f_i denotes the contribution of node i to the force, $\overline{f}_j$ represents the total force generated at the actuator point j, N is the number of nodes in each element and N_a the number of actuator points. The projection of forces onto the intrinsic axes of the problem and the addition to the Navier-Stokes equations as a source term are carried out in the same manner as in the AL1 method.

8.4 Numerical results

This small wind turbine has been tested aerodynamically in the NTNU wind tunnel and has been used as a benchmark [7, 96, 97]. It is a three-blade wind turbine of 0.894 m diameter. The blades use the NREL S826 airfoil along the entire span. The twist and chord distribution, airfoil coordinates and the wind turbine CAD can be found in [96]. The hub height is 0.817 m. The wind turbine blades consist of cylinders up to $R_a = 0.049$ m.

The operational conditions of this wind turbine are: $\Omega = 1281.8$ rpm; $U_0 = 10$ m/s, pitch angle, $\theta_p = 0°$, Tip Speed Ratio, $TSR = \Omega R/U_0 = 6$, being the test case 1 presented in [97]. The incoming flow is uniform, with very low turbulent conditions, reported in the experimental campaign a turbulence intensity of $Tu_0 = 0.23\%$. Since it is a very small value,, we can neglect the turbulence in the numerical setup,

thus the AL simulations were conducted assuming non turbulent inflow.

The domains simulated includes the whole extend of the wind tunnel section, simplifying it to a perfect rectangular prism of dimensions $[11.15, 2.71, 1.8]$ (m). The domain is discretised in a fully conforming hexahedral mesh of $128 \times 24 \times 24$ elements, all of them with the same size. Boundary conditions are weakly imposed via Riemann solver, using uniform velocity for the inlet, pressure-based for the outlet, and free slip wall for the other four faces, simplifying the real behaviour of the wind tunnel walls, as we do not intend to simulate its boundary layer. The numerical settings are Gauss nodes, with the Roe Riemann solver and BR1. Explicit LES is used as the turbulent closure, using the Vreman model.

Polynomials order from 2 to 5 constant for all elements in all directions are used as high-order discretisation. A sweep in the constant k of 8.8 is performed for the lowest polynomial order, performing 5 simulations with values from 1.5 to 2.75, using the convention of ϵ_k to represent the simulation of a certain k value. For the polynomial order 3, the number of simulations is reduced to 2 of them, while only one is used for the two higher polynomial orders. This is done for both methods, AL1 and AL2, obtaining a total of 20 simulations. The exact values of ϵ and k are presented in Table 8.1, along with the correspondent Δ for each polynomial order and the total NDOF.

p	Δ [m]	$\epsilon_{1.5}$	ϵ_2	$\epsilon_{2.25}$	$\epsilon_{2.5}$	$\epsilon_{2.75}$	NDOF
2	0.03012	0.04518	0.06024	0.06777	0.07530	0.08283	1.99M
3	0.02259	–	–	–	0.05647	0.0621	4.72M
4	0.01807	–	–	–	–	0.04969	9.22M
5	0.01506	–	–	–	–	0.04142	15.93M

Table 8.1: Values of the projection parameter, ϵ, based on the polynomial order.

For all the cases, start the simulation from a uniform flow, let it develop for $20T^*$ (about 43 periods of rotation of the wind turbine), and then collect statistics for $10T^*$. The adaptive time step is used based on the CFL value, with values lower than $6 \times 10^{-4}T^*$ for the lowest polynomial order to $2 \times 10^{-4}T^*$ for the highest one, making sure that in one time step the actuator point does not change its position drastically compared to the Gauss nodes.

For both methodologies the $\epsilon_{1.75}$ produced numerical divergence, probably because the value is too small that it does not provide enough smoothing for the projection

of the force into the fluid.

8.4.1 Wind turbine coefficients

First, we present the time averaged power (C_P) and thrust (C_T) coefficients of the wind turbine, defined as,

$$C_P = \frac{Q\Omega}{\frac{1}{2}\rho_0 U_0^3 \pi R^2}; \quad C_T = \frac{T}{\frac{1}{2}\rho_0 U_0^2 \pi R^2}. \tag{8.11}$$

where Q represents the total torque of the wind turbine and T represents the thrust and R the radius of the blades. In the experiments carried out, the values obtained were $C_P = 0.45$ and $C_T = 0.9$. For all the cases, the power and thrust are calculated at each actuator node and the integrated along the blade. The results for each polynomial and ϵ are presented in Table 8.2 for the AL1 method and Table 8.3 for the AL2.

p=2				**AL1**
ϵ	ϵ_2	$\epsilon_{2.25}$	$\epsilon_{2.5}$	$\epsilon_{2.75}$
C_P	0.589478	0.604494	0.62109	0.637955
C_T	0.899552	0.90732	0.916623	0.925953
p=3				**AL1**
C_P	-	-	0.58497	0.595791
C_T	-	-	0.899046	0.903251
p=4				**AL1**
C_P	-	-	-	0.574034
C_T	-	-	-	0.891353
p=5				**AL1**
C_P	-	-	-	0.564624
C_T	-	-	-	0.887237

Table 8.2: Averaged velocity method: C_P and C_T based on the polynomial order and ϵ.

The instantaneous values present oscillations during the simulation ranging from 1% to 3% about the mean value. It can be observed that both the coefficients show an increasing trend with the projection parameter when the polynomial order remains constant.

p=2				**AL2**
ϵ	ϵ_2	$\epsilon_{2.25}$	$\epsilon_{2.5}$	$\epsilon_{2.75}$
C_P	0.628962	0.64718	0.666427	0.684074
C_T	0.904623	0.916546	0.929052	0.939782
p=3				**AL2**
C_P	-	-	0.621007	0.63465
C_T	-	-	0.899047	0.908509
p=4				**AL2**
C_P	-	-	-	0.606609
C_T	-	-	-	0.888485
p=5				**AL2**
C_P	-	-	-	0.594947
C_T	-	-	-	0.875988

Table 8.3: Weighted sums method: C_P and C_T based on the polynomial order and ϵ.

8.4.2 Force distribution along the blade

For each actuator point, the resultant force calculate by the Blade Element Theory is stored. As mentioned in the methodology, for AL1, the fluid variables are the same in all nearby nodes and are scaled only with distance. However, for AL2, each node has its own fluid variables that generate different forces, which are then scaled with respect to the distance and then averaged using a weighted mean. In this Section we present this forces along the blade, calculated as time averaged, comparing results for all the ϵ parameters and then keeping it constant and varying the polynomial order.

Figure 8.4 illustrates the radial variation of both dimensionless axial and tangential forces along the rotor blade. A sharp change in tangential forces can be observed around $r/R \approx 0.1$ in Figures 8.4 b), d) and f) which is attributed to the abrupt profile change in the model studied [96] (from having a circular profile at the root, which only contributes with drag, to the NREL-S826 airfoil for the rest of the blade). Beyond this point, we encounter a homogeneous distribution of tangential force, a result of the twist introduced along the blade to maximize the force generated in the direction of rotation. Alternatively, in the axial forces shown in Figures 8.4 a), c), and e), there is a monotonic increase as we approach the blade tip, resulting from the increase in local velocity (and consequently, aerodynamic forces) with the distance from the axis of rotation. In both the cases, the forces tend to cancel out at $r/R \approx 1$ due to the necessary condition of pressure continuity at the blade tip [147].

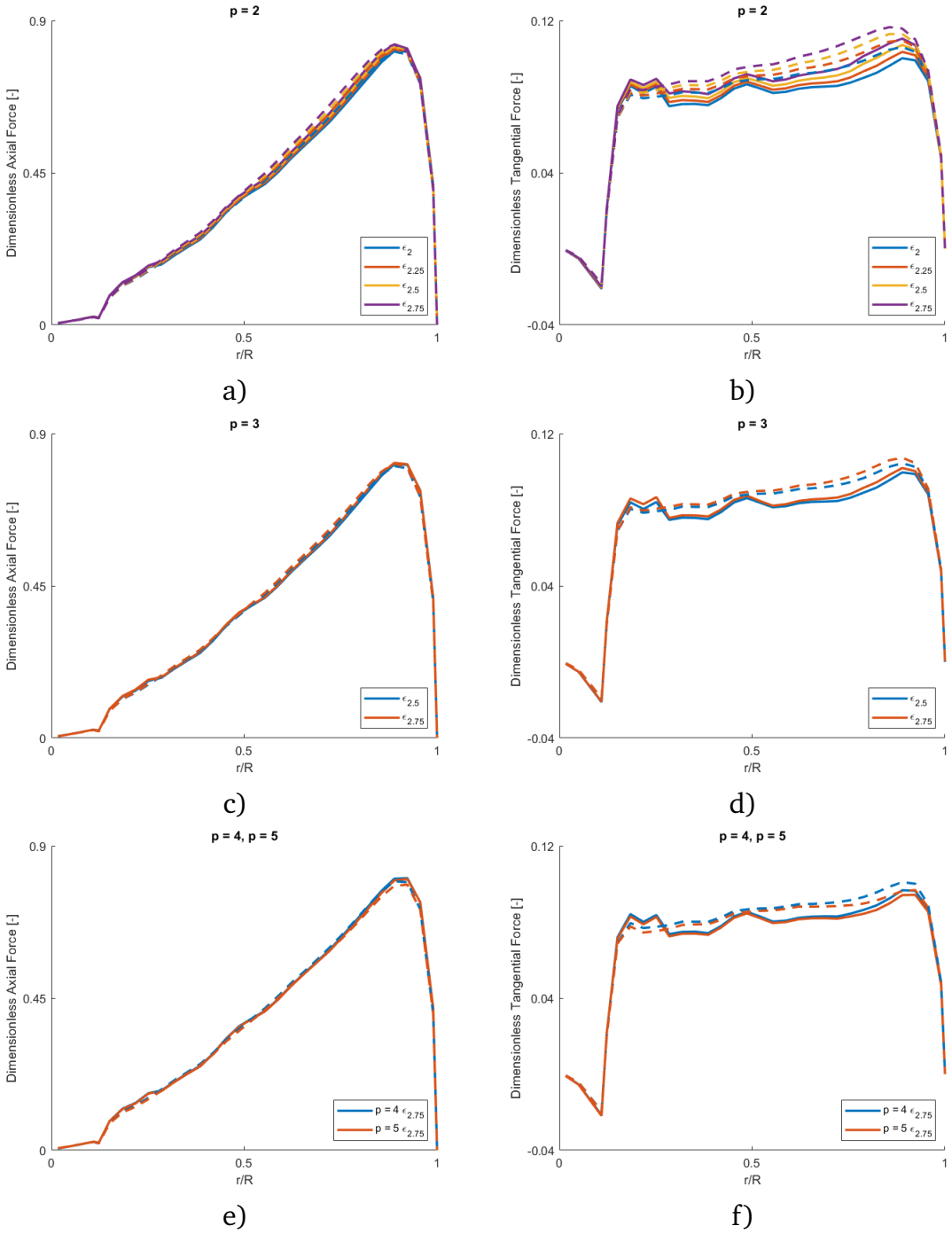
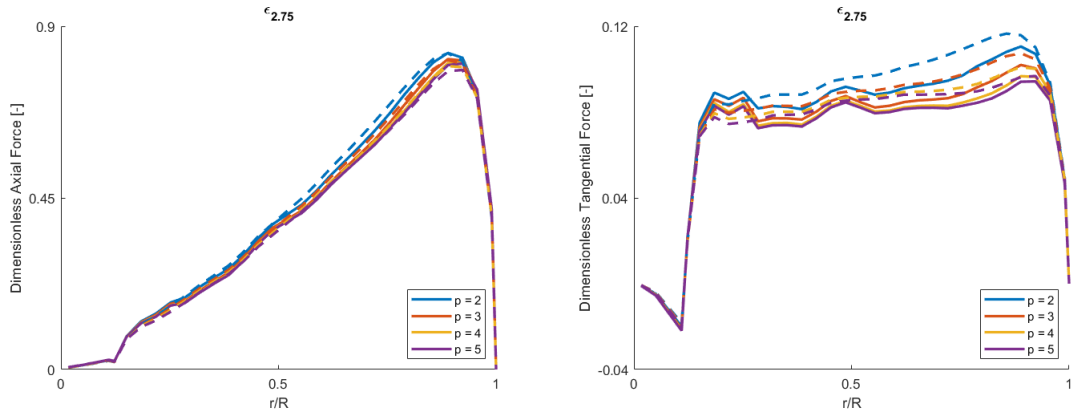


Figure 8.4: Axial and tangential non-dimensional forces along the blade based on polynomial order. '—' AL1, '- -' AL2.

Similar trends in the forces generated on the blade can be observed in previous works, such as those by Deskos et al. [46]. If we compare the two methods em-

ployed, it can be observed that AL2 yields a smoother and slightly superior solution overall compared with the AL2 method. This result is consistent with the previously shown values of the C_P and C_T coefficients, as they are constructed based on these forces (as in (8.11)).

It is interesting to compare the evolution of the difference between these methods for different polynomial orders and observe that, in general, increasing the polynomial order tends to decrease the difference between methods, as shown in Figure 8.5. It can be observed that, in general, a more pronounced convergence between methods is achieved in axial force as the polynomial order increases. However, the error in the tangential force is higher because the AL2 method provides a more homogeneous solution, further away from the oscillations of the AL1 method. Additionally, the convergence between methods with the polynomial is less pronounced.



c) b)

Figure 8.5: Axial and tangential forces along the blade, $\epsilon_{2.75}$. '—' AL1, '- -' AL2.

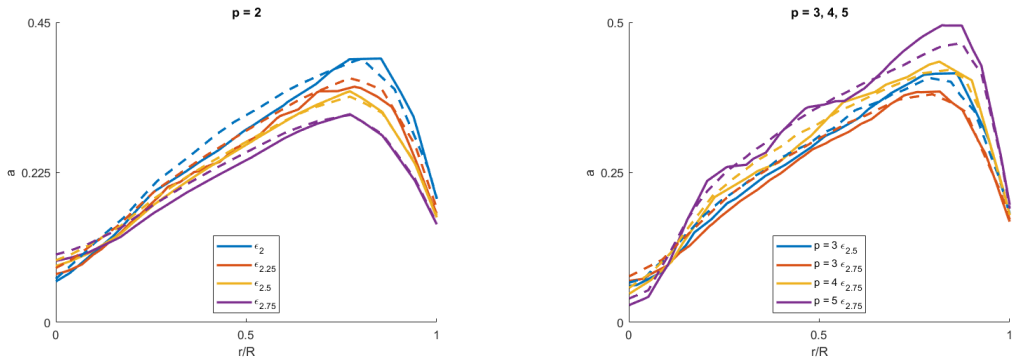
8.4.3 Velocity decay along the blade

As will be discussed in Section 8.4.4, for smaller values of the ϵ parameter, the velocity distribution obtained has sharper gradients that become more blurred as this parameter increases. It is now appropriate to define a new variable: the axial velocity decay,

$$a = 1 - \frac{u_x}{U_0}, \tag{8.12}$$

useful for wake representation. In Figure 8.6, we present this variable along the

blade, similar to the forces. It can be seen that there is a clear relationship between the velocity decay and the axial force of the blade. The growth trend along the blade is the same, and the peaks of the axial force align with the maximum velocity decay. The difference between the AL1 and AL2 methods in the axial direction is more pronounced in the velocity decay than in the previously represented axial force, with the latter method generating smoother solutions. The difference introduced by the polynomial order at a constant ϵ is slightly larger, particularly noticeable in the maximum where the solution becomes smoother, but the overall trend remains the same.



a) b)

Figure 8.6: Velocity decay along the blade based on ϵ for different polynomial orders. '—' AL1, '- -' AL2.

8.4.4 Wake velocity field

To further understand the flow physics of the wake, a streamwise sections of the wake are shown based on the instantaneous flow field, u_x, for different polynomial orders in Figure 8.7. It is evident that the gradients become sharper with increasing polynomial order demonstrating higher wake resolution. Aditionally, with the increase in polynomial order, oscillatory phenomena begin to appear (Figure 8.7 c) and d)), forming vortex structures that eventually collapse in the far wake region, showing a more turbulent behaviour compared to the lowest order one.

In another way to depict the improved resolution with polynomial orders, the iso-contours of the Q-criterion are plotted for all the polynomial degree coloured using streamwise velocity (Figure 8.8). A rapid improvement in resolution can be observed with the increase in polynomial order, making it possible to distinguish the evolution of the generated structures from $p = 4$. Approximately at a distance of

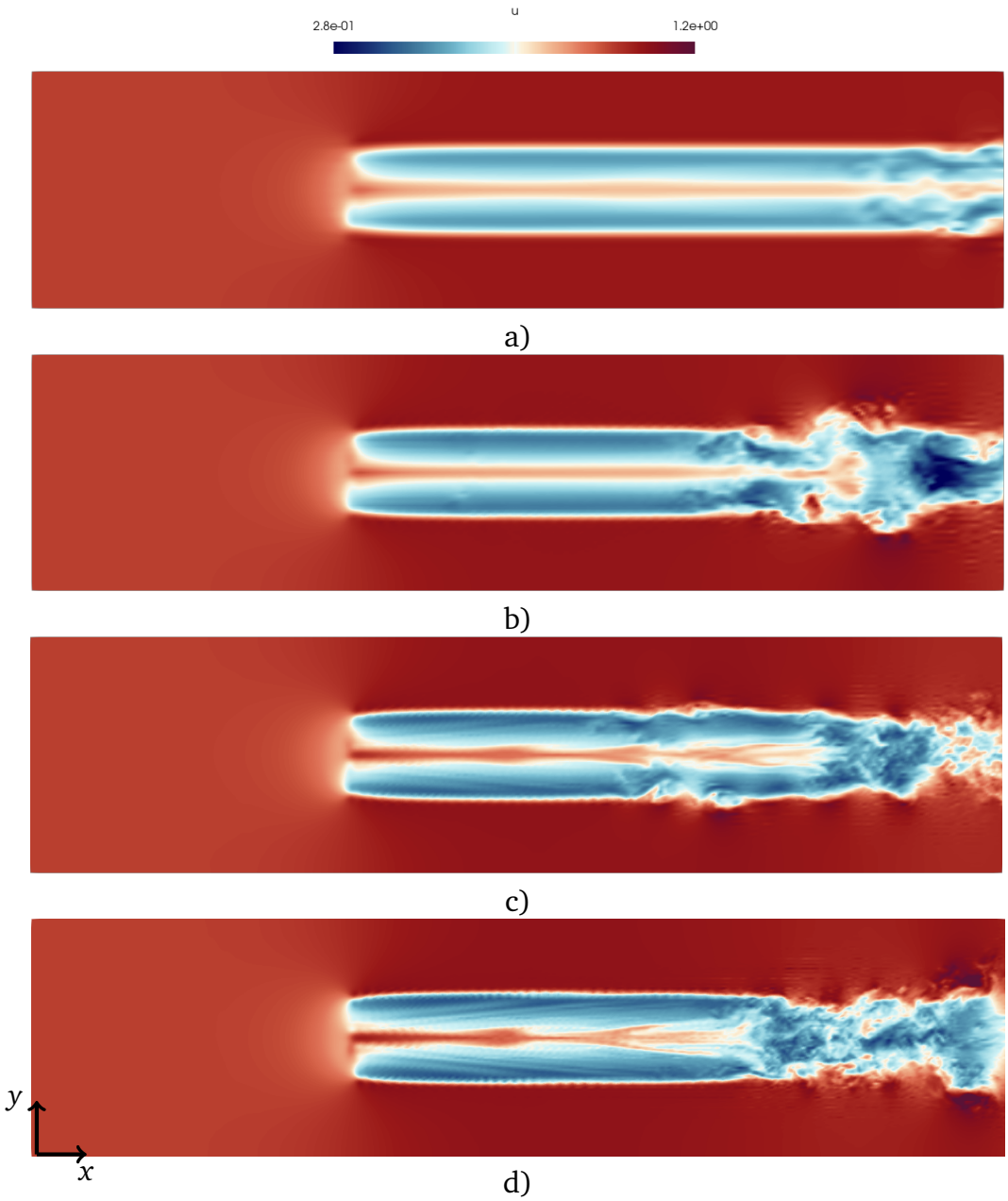


Figure 8.7: Section of the instantaneous velocity field along the x-axis for $\epsilon_{2.75}$, a) $p = 2$, b) $p = 3$, c) $p = 4$ and d) $p = 5$ using AL1 method.

one rotor diameter from the rotor plane, its identity is maintained, clearly reflecting the rotational motion of the blades. Further downstream, the structures break down due to enhanced shear and mixing and tend to become more homogeneous. Qualitalitvely, the wake for both methodologies can be seen as similar.

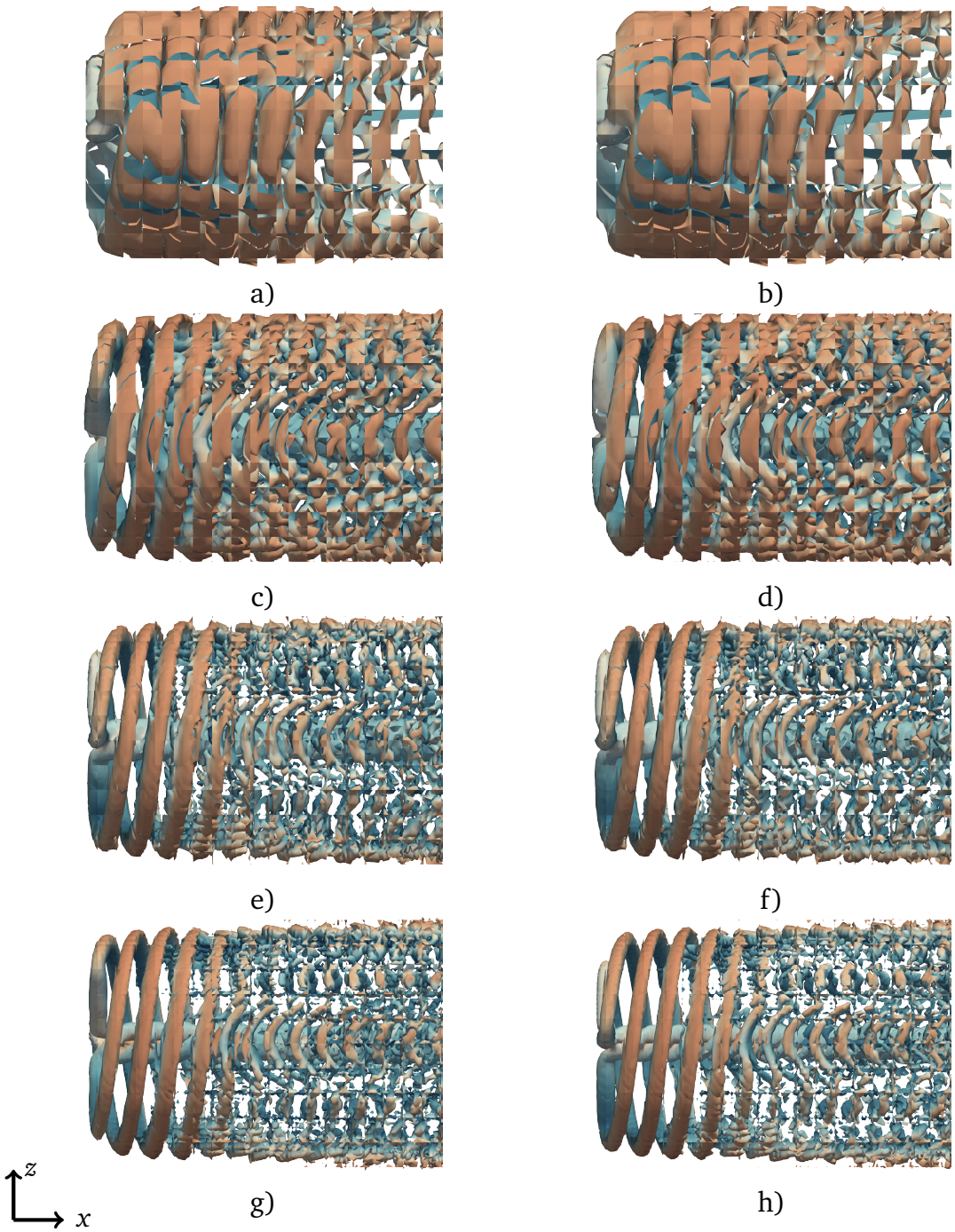


Figure 8.8: Detail of the near wake flow structures visualized using Q-criterion isosurfaces based on the polynomial order colored by u velocity for $\epsilon_{2.75}$ a) AL1 $p = 2$, b) AL2 $p = 2$, c) AL1 $p = 3$, d) AL2 $p = 3$, e) AL1 $p = 4$, f) AL2 $p = 4$, g) AL1 $p = 5$ and h) AL2 $p = 5$.

Stepping into qualitative results, we compare the time-averaged axial velocity at the wake of the turbine with the experimental data for wind tunnel measurements [97]. Available results are for horizontal lines (varing on y direction) at distances from the rotor of $x/D = 1$, $x/D = 3$, and $x/D = 5$, as depicted in Figure 8.9. Here, D represents the diameter of the wind turbine.

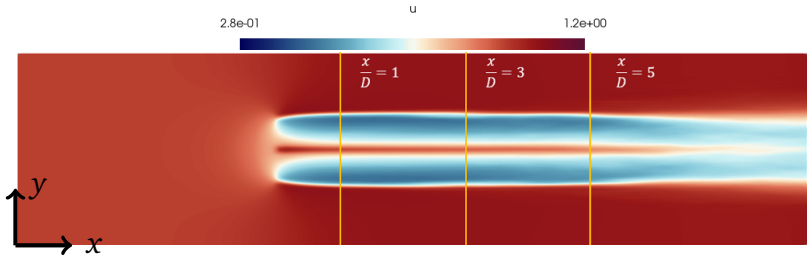


Figure 8.9: Segments in which the velocity decay, a, is represented.

Results for the first line are shown in Figure 8.10 for all the polynomial orders and ϵ factor. The variations across the wake demonstrate that reducing the projection parameter causes the flow to decelerate to a greater extent as it passes through it. When the value of ϵ is reduced, are introducing the forces closer to a punctual source, because the Gaussian curve becomes sharper. This leads to an exponential growth of $\eta(d)$ and, consequently, of the local forces introduced in the solver, resulting in a sharper velocity decay behaviour. At the boundaries y/R $\approx$ 0.8, there is an excess of introduced force, while at the centre $y/R \approx 0$, there is a deficiency of force as the nearby actuator points lack of a wide enough Gaussian curve to encompass the centre of the turbine (the present simulations have not considered the effects of tower or nacelle).

Figure 8.11 shows the effect of increasing the polynomial order on the velocity decay profile for a constant value of k. A more pronounced velocity decay can be observed when increasing the polynomial order, especially at relative extremes, which has also been noted in the work of [180], when performing mesh refinement. It can also be observed, a greater velocity decay in the central region of the wake in the experimental data. The simulations performed do not exhibit this behaviour because the centre of the turbine has not been modeled and the corresponding wake effects are not accounted for. Therefore, the flow in the central region of the rotor wake remains only marginally disturbed.

Figure 8.12 and Figure 8.13 depict the velocity decay on the other two lines, at $x/D = 3$ and $x/D = 5$ respectively. At greater distances from the rotor, the experimental measurements clearly indicate turbulent flow behaviour, where a practically homogeneous velocity field is observed across the wake. While the numerical results show a widening of the region with a higher velocity decay, even in the centre,

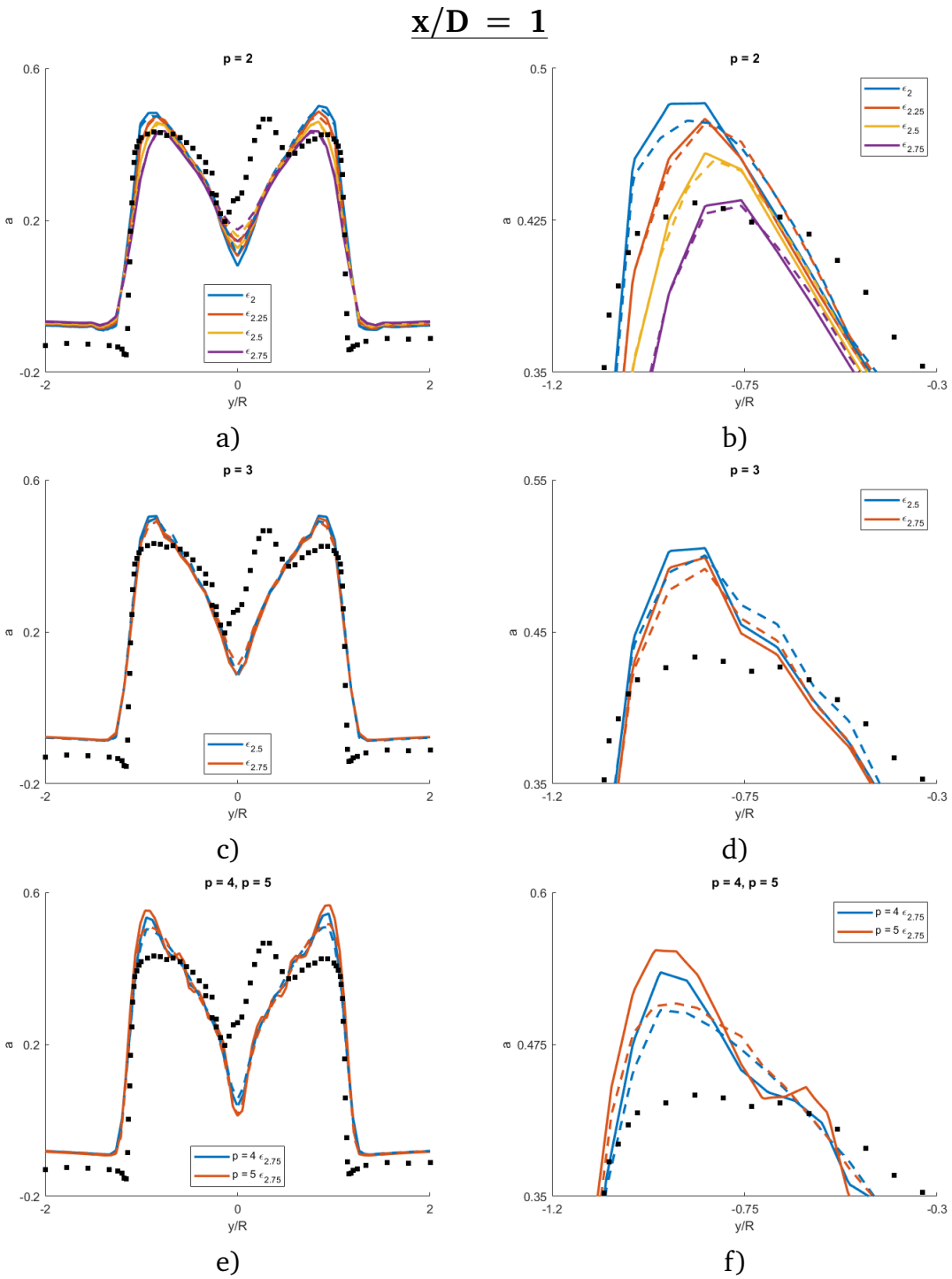
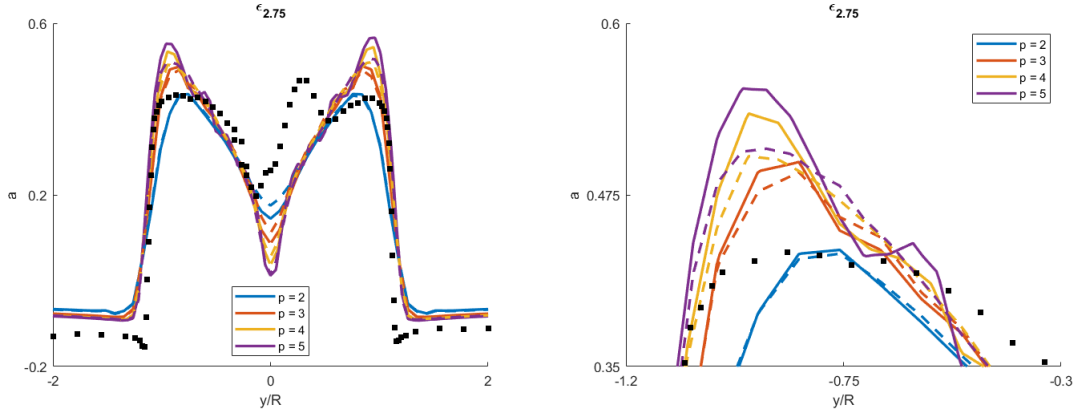


Figure 8.10: Velocity decay, a, for different polynomial order based on ϵ, $x/D = 1$. '—' AL1, '- -' AL2 ', ■' Experimental data.

a directional flow with higher than expected velocities is still obtained. Capturing



a) b)

Figure 8.11: Velocity decay, a, for $\epsilon_{2.75}$ based on p, $x/D = 1$. '—' AL1, '- -' AL2', ■' Experimental data.

this phenomenon can be improved by refining the mesh, as the current simulations are performed on a mesh that is not fine enough to capture the smaller turbulence scales. Based on the results, it may appear that mesh refinement only from $x/D = 3$ would be sufficient. However, refinement near the rotor should also be done to accurately capture the transitional flow behaviour.

In all cases, for the higher polynomial orders, the AL1 method, that uses an average of the element results in wakes with spikes, rather than the smoother solutions of the AL2. This is clearer at greater distances, i.e. Figure 8.12f and Figure 8.13f. To compare it for all polynomial orders, we plot the together in Figure 8.14, comparing them for $\epsilon_{2.75}$. Here is clear that for higher polynomial order, there is a difference in the behaviour of the velocity decay depending on the calculation method. The AL2 method continues to provide more homogeneous profiles, while the AL1 method begins to capture oscillatory phenomena across the wake, which become more pronounced as we move downstream.

The general behaviour of the wake is captured for all cases, with a growth of the velocity deficit in acordance with the experimental values. The centre of the wake has differences due to the tower and nacelle not being include in the simulations.

8.4.5 Turbulent Kinetic Energy

When analyzing the average turbulent kinetic energy at the rotor planes $x/D = 1$, 3 and 5, we see evidences of the need high resolution as provided when increasing the polynomial order. Near the rotor, where turbulent flow has not yet been fully

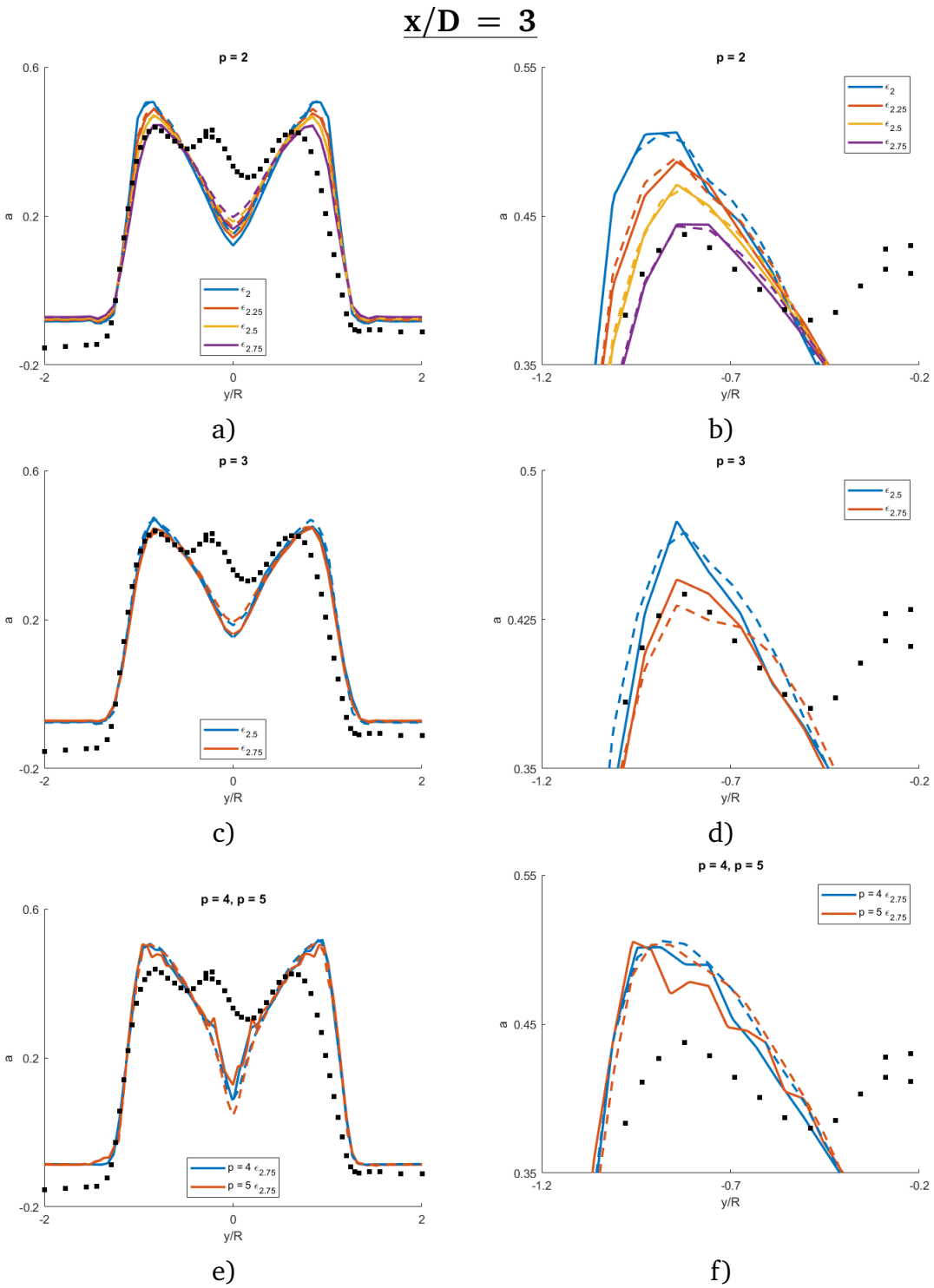


Figure 8.12: Velocity decay, a, for different polynomial order and ϵ parameter, $x/D = 3$. '—' AL1, '- -' AL2', ■' Experimental data.

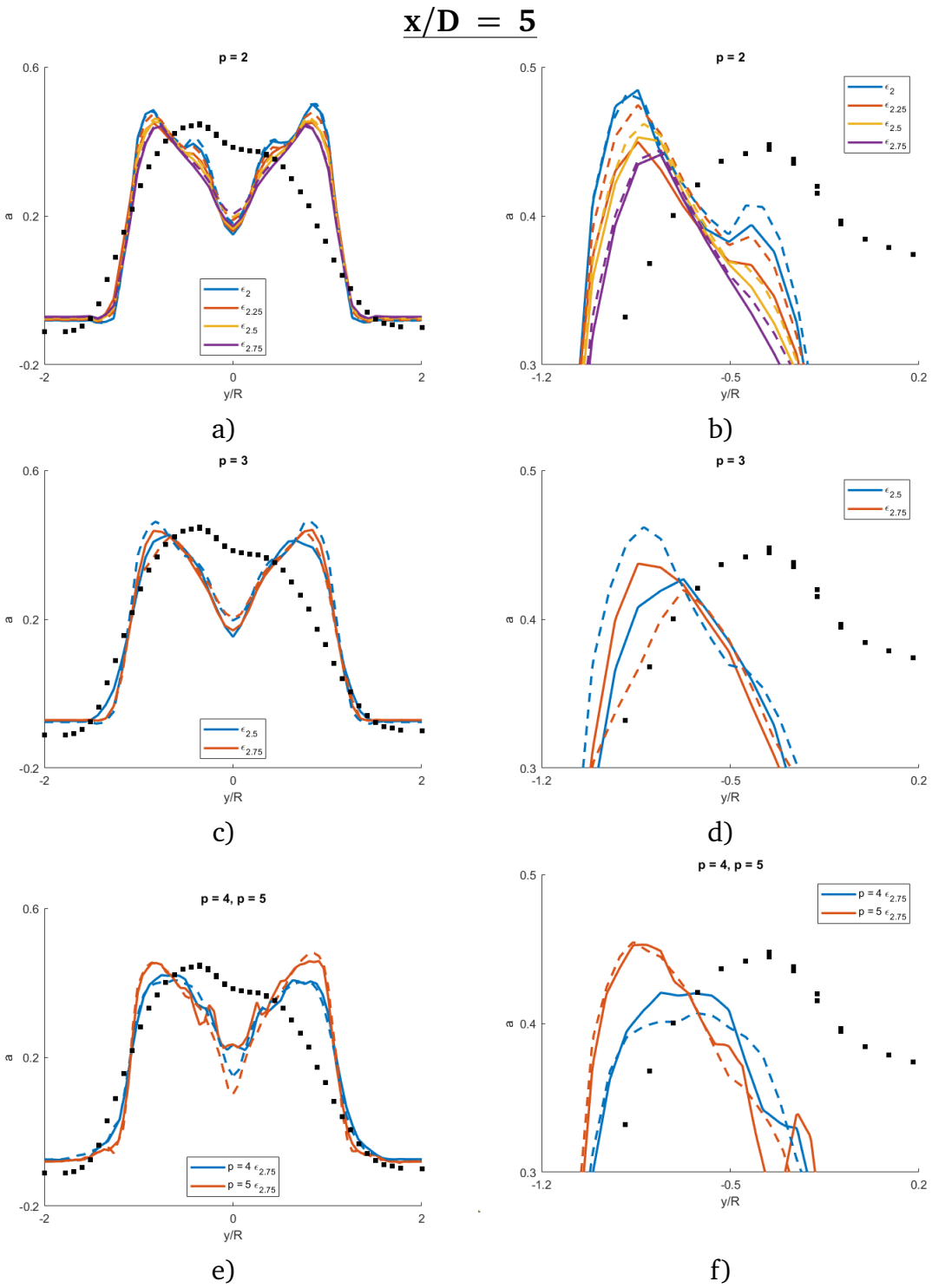


Figure 8.13: Velocity decay, a, for different polynomial order and ϵ parameter, $x/D = 5$. '—' AL1, '- -' AL2', ■' Experimental data.

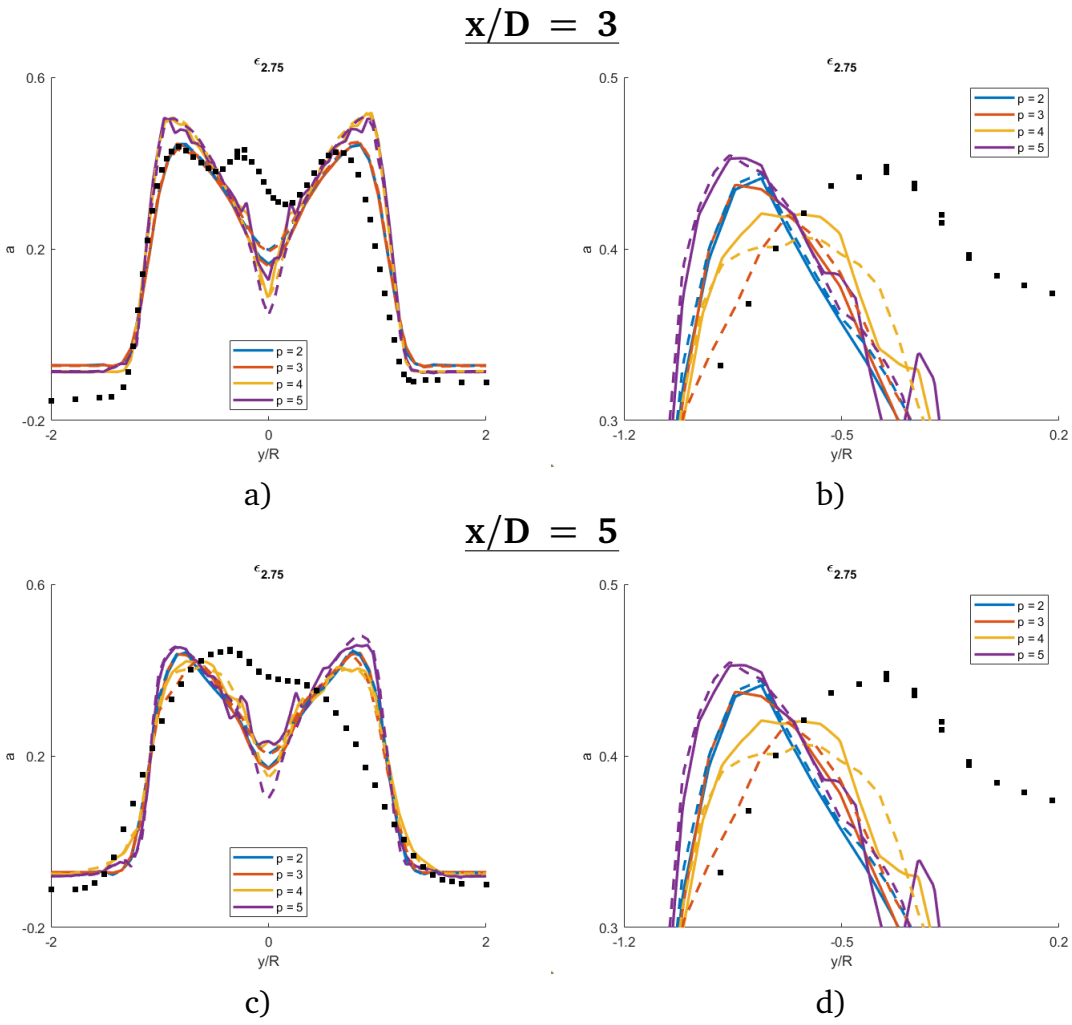


Figure 8.14: Velocity decay, a, for different polynomial order with $\epsilon_{2.75}$.
a) & b) for $x/D = 3$; c) & d) for $x/D = 5$. '—' AL1, '- -' AL2', ■' Experimental data.

developed, the results are distant from experimental data. Additionally, simulations with lower polynomial orders exhibit oscillations around values that deviate from experimental data, confirming their inability to accurately capture the physical phenomenon (Figure 8.15).

At greater distances from the rotor ($x/D = 3$ or 5), we observe better match with the experimental values. Note that the nacelle and tower are not include in these simulations and therefore lower turbulence is expected in the wake. This observation has already been reported [166] where AL methods under-predict turbulent generation but leads to accurate turbulent fluctuation in the far wake. Since the main interest of the actuator line models is to predict the wake at large enough

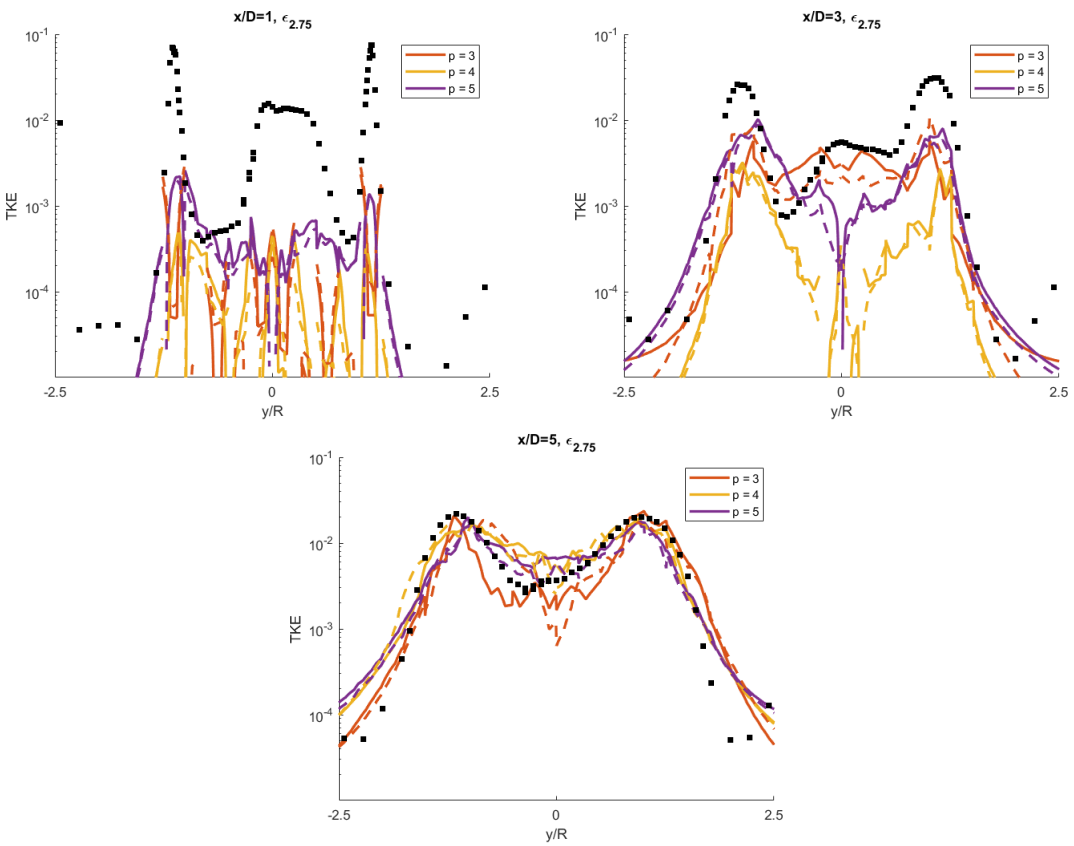


Figure 8.15: Turbulent kinetic energy at $x/D = 1$ (left), $x/D = 3$ (right) and $x/D = 5$ (below) for different polynomial order with $\epsilon_{2.75}$. '—' AL1, '- -' AL2', ■' Experimental data.

distances from the rotor, the results obtained offer a satisfactory balance between calculation time and precision. Regarding the comparison between AL1 and AL2 methods, a greater disparity has been observed than in the calculation of forces and velocity; nonetheless, the solutions clearly converge when increasing the polynomial order.

8.4.6 Tower and Nacelle

When incorporating the tower and nacelle into the simulations, we observe that the presence of the tower alters the flow field near the rotor, enhancing turbulence and mixing in the wake, influencing the turbine's performance and power output. Additionally, the nacelle creates aerodynamic interference, affecting the airflow over the rotor blades and altering the aerodynamic forces experienced by the turbine. These effects are clearly visible in figures , where we compare simulations with/without

nacelle and tower. Here, the nacelle and tower is modelled using immersed boundaries [58, 95] which accounts for the three dimensional shape of these object and is not represented as a flow resistance object though discrete source terms (as in actuator lines). These actuator line with and without immersed boundary are simulated using a h-mesh with element size half size in each direction and polynomial order 2, such that the total number of degrees of freedom are the same as the cases with polynomial order 5 in the previous sections.

Incorporating these factors into simulations allows for more accurate predictions of power outputs, load distributions and wake deficits, see Figure 8.16, but can hide small differences when modeling rotating blades using actuator lines, as seen in Figure 8.17. For this reason, we have preferred to not include the tower and nacelle in the previous comparisons. By doing so, small differences between the actuator line implementations could be identified.

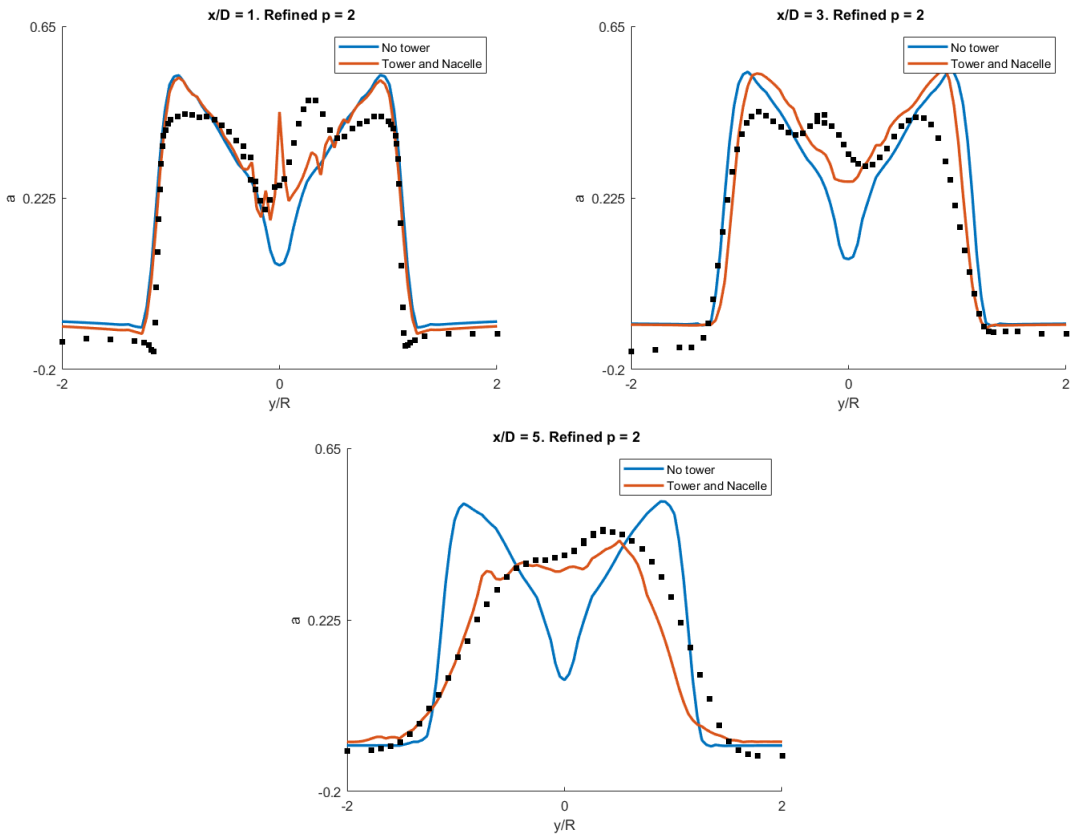
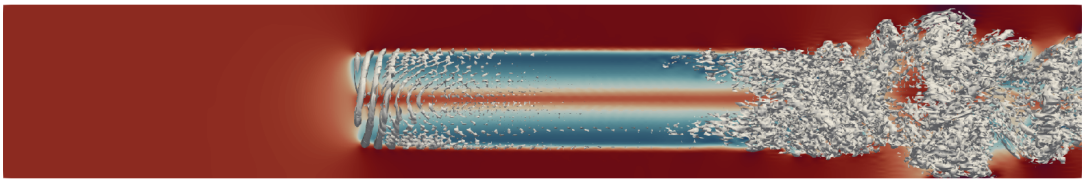
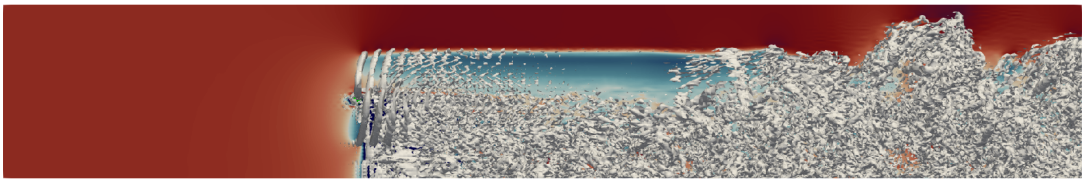


Figure 8.16: Velocity decay, a, with a $p = 2$ h-mesh with and without tower and nacelle implementation. '—' AL1', ■ 'Experimental data.



a) Actuator line without tower and nacelle.



b) Actuator line with tower and nacelle, modelled using immersed boundaries.

Figure 8.17: Section of the instantaneous velocity field along the y-axis with the Q-criterion isosurfaces for $\epsilon_{2.75}$ a) Actuator line without tower and nacelle. b) Actuator line with tower and nacelle, modelled using immersed boundaries.

8.4.7 Computational Cost

The appeal of the Actuator Line methods lies in their ability to generate results close enough to the physical phenomenon under study in a relatively short time, allowing for the establishment of important parameters such as the spacing between rotors in the preliminary phases of wind turbine project development. The variability of these parameters initially is significant, which is why it is advantageous to minimize the computation time to facilitate the study of the project with a wide range of configurations.

To thoroughly study the calculation times, simulations (already in a stable phase) have been run for 100 time steps, and the results have been compared based on the polynomial order used. Since we use a variable time step size based on CFL, it has been averaged to obtain a representative value. Although simulations of orders higher than 5 have not been conducted, values up to $p = 6$ are included in this analysis for greater generalization and to pave the way for future implementations with higher orders.

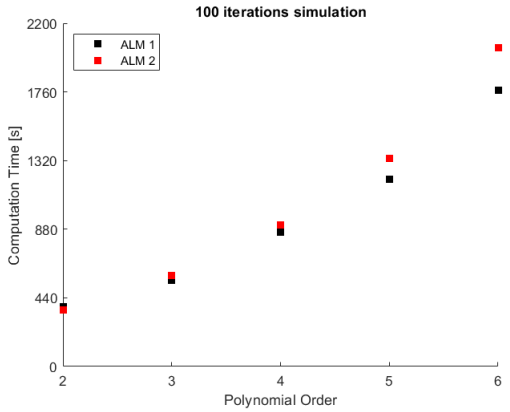


Figure 8.18: Simulation time for AL1 (averaging) and AL2 (projection): 100 Iterations simulation time for polynomial orders ranging from 2 to 6.

As observed in Figure 8.18 a), there is an exponential growth in calculation time with the polynomial order, as expected. It is interesting to note a progressive divergence between AL1 and AL2 methods due to the higher number of projections carried out in the latter. This suggests that using AL1 may be more convenient if prioritizing calculation time, especially for simulations of high order. Since the time step size is calculated based on the number of nodes in the mesh, it is the same for both methods (Figure 8.18 b)), making them equally robust against temporal instabilities.

8.5 Summary

In this chapter, we have studied and compared, we have demonstrated the effectiveness of integrating the actuator line method with high-order h/p solvers for wind turbine modeling. By representing the rotating turbine blades as distributed force lines, with appropriate tip-corrections, the actuator line method captures the blade's influence on the flow field in a computationally efficient manner. Through extensive numerical simulations and validation against experimental data, we have shown that the combined approach of actuator lines and high-order h/p solvers offers improved accuracy and fidelity in capturing the complex flow phenomena around wind turbine blades. The following main :

- Near and far wake first order statistics (e.g., velocity) are well captured once a sufficient polynomial order is selected. Second order statistics (e.g., turbulent kinetic energy) are well captured in the far wake. In the near wake the AL

method under-predict turbulent generation, which has been already observed in previous work [166].

- The two implemented AL methods (averaging and projection) shown similar accuracy and robustness. In terms of accuracy both provide valid results and faithfully captures the oscillatory phenomena in the wake. The AL1 provides more spikes while the AL2 is smoother.
- The AL1 formulation (averaging) is less costly for high polynomial orders than AL2.
- High polynomial orders prove advantageous in capturing the correct physics. Doing polynomial refinement is recommended against h-refinement.

Chapter 9

Coupling for Wind Turbine Acoustic

Contents

9.1 Introduction 125
9.2 The Strip Theory 127
9.2.1 Coordinates transformation 128
9.2.2 Emission frequency 129
9.3 AL coupling 129
9.4 Numerical results 130
9.5 Summary 136

9.1 Introduction

There are several empirical methods to predict the overall noise level produced by a wind turbine based on the rated power and diameter, which are commonly used in noise regulations [71]. These engineering methods are inaccurate when predicting noise in the frequency domain or when dealing with non-nominal operational and atmospheric conditions (e.g., skewed wings, varied turbulence levels, etc.). An alternative for predicting detailed aeroacoustic prediction from wind turbines is to use high-fidelity CAA models, as done in Chapter 6. The main limitation of CAA methods is the high computational costs since the flow needs to capture the evolution of turbulent eddies interacting with the blade surface to obtain the pressure fluctuations responsible for noise generation. Conducting large eddy simulations (LES) with this level of detail remains expensive. A cheaper alternative is

to use Reynolds Averaged Navier-Stokes (RANS) to model turbulence, as conducted by [160]. This approach provided reasonable results for low frequencies but is difficult to generalise to more complex atmospheric or operational conditions.

A mid-ground approach is using strip theory methods, where wind turbine noise is calculated by dividing each blade into uncorrelated blade segments, and the noise of each segment is calculated using prediction methods for 2D airfoils. This method was proposed by [142] for helicopters and has recently been applied to fans [138], wind turbines [15, 37, 161], and open propellers [150].

Two main methods are available in the literature for predicting the trailing-edge noise of 2D airfoils. The first is the empirical method proposed by [23], known as the Brooks-Pope and Marcolini (BPM) model, based on measurements of the boundary layer and the far-field noise of several NACA 0012 airfoils with different chords. Although very useful for quick estimates, the main limitation of this method is that the airfoil geometry and operational conditions of wind turbines differ significantly from a NACA 0012 airfoil and the test conditions used by [23]; therefore, the prediction for general wind turbines may be inaccurate. The second is the semi-analytical approach proposed by Amiet [5], explained in Chapter 7. Here, the geometry of the airfoil and operational conditions are taken into account in the calculation of the wall-pressure spectrum model.

An alternative to overcome these issues is to use the actuator line (AL) model described in Chapter 8, which provides a computationally efficient approach to calculate the aerodynamic loads on the turbine. AL model has been coupled with the BPM model to calculate the trailing-edge noise of wind turbines, either directly [43], or used in conjunction with linearized equations, such as the Acoustic Perturbation Equation (APE) [53], using AL + BPM as input to APE [33, 42, 179]. In these cases, the fundamental problem of the BPM not taking into account the actual geometry of each airfoil section remains.

In this Chapter, we use a method for predicting wind turbine noise based on the AL model coupled with the Amiet-schlinker theory for rotatory noise sources [142], considering the leading- and trailing-edge noise as the unique and independent noise source of a wind turbine, modelled using Amiet's theory. This is obtained both, considering a time-averaged blade loading and instantaneous one at each azimuthal location, which can account for nonaxisymmetric or transient phenomena.

We test this methodology with a full-size real turbine, comparing with experimental data.

9.2 The Strip Theory

In this Section we introduce the strip theory, which is used to calculate The noise produced by the wind turbine by dividing the blade is divided into n segments. For each segment, leading- and trailing-edge noise is calculated as uncorrelated noise sources using Amiet's method for 2D airfoils, as presented in Chapter 7. The parameters of the boundary layer that are used as input for the TE model are calculated for the effective local velocity and angle of attack of each segment obtained from the AL method, which accounts for the rotational velocity plus the induced velocity and inflow velocity. Afterward, the total noise of the blade is calculated as the sum of the total noise of each segment. This procedure is performed for each angular position θ.

The relative motion of the segment that induces a delay between the origin of the noise and the location of the observer is considered by a Doppler effect factor ($= \omega_e/\omega$). The total noise of the blade at each azimuth location is calculated by summing the noise produced by all the segments,

$$S_{pp|\text{blade}}(\omega,\theta) = \sum_{1}^{n} S_{pp|\text{seg}}(\omega_e,\theta)(\omega_e/\omega)^2; \tag{9.1}$$

where $S_{pp|\text{blade}}(\omega,\theta)$ is the total noise of the blade as a function of the angular frequency (ω) for each azimuthal angle (θ), and $S_{pp|\text{seg}}(\omega_e)$ is the total noise of each segment calculated in the emission angular frequency (ω_e). An exponent of 2 in the Doppler factor (ω_e/ω) in (9.1) is considered following the methodology of [150]. The total noise of each segment is calculated as the sum of leading- and trailing-edge noise ($S_{pp|seg}(\omega_e) = S_{pp|\text{LE}}(\omega_e) + S_{pp|\text{LE}}(\omega_e)$).

The average noise produced by the wind turbine in one rotation ($S_{pp|\text{WT}}(\omega)$) is then calculated as:

$$S_{pp|\text{WT}}(\omega) = \frac{B}{2\pi}\int_{0}^{2\pi} S_{pp|\text{blade}}(\omega,\theta)\mathrm{d}\theta; \tag{9.2}$$

where B is the number of blades.

9.2.1 Coordinates transformation

To calculate the noise prediction of each segment, the location of the observer needs to be transformed in the coordinates of Amiet's theory from the wind turbines reference frame. Using the notation of Chapter 6, the former, as defined in Chapter 7 is $\mathbf{y}_a = [x_{oa}, y_{oa}, z_{oa}]^T$ (chordwise, spanwise, and normalwise, respectively), while the latter is defined for the AL, in Chapter 8, as $\mathbf{y}_{WT} = [x_{oWT}, y_{oWT}, z_{oWT}]^T$ (see Figure 8.1).

First, we need two rotations, one to shift the axis such that the main distance, the streamwise one, coincides with the z-axis, and the second to rotate it in the x_{WT} axis such that the y-axis points in the spanwise. For this, we start with the geometrical radius between the turbine hub and the observer in the WT frame, $\mathbf{r}_{WT} = \mathbf{x}_{WT} - \mathbf{y}_{WT}$ and rotated it to obtain it in the blade reference frame:

$$\mathbf{r}_{blade} = M_x M_z \mathbf{r}_{WT}, \tag{9.3}$$

where M_x and M_Z are rotational matrices,

$$M_x = \begin{bmatrix} 0 & 1 & 0 \\ 0 & 0 & 1 \\ 1 & 0 & 0 \end{bmatrix}, \; M_z = \begin{bmatrix} \sin\theta & -\cos\theta & 0 \\ \cos\theta & \sin\theta & 0 \\ 0 & 0 & 1 \end{bmatrix} \tag{9.4}$$

Then, a translation is performed in the radial direction of the blade (spanwise of the segment), to obtain the distance from the actual segment,

$$\mathbf{r}_{seg} = \mathbf{r}_{blade} + \begin{bmatrix} 0 \\ -R_a \\ 0 \end{bmatrix}, \tag{9.5}$$

Finally, a rotation in the y_{seg} -axis is carried out to align the x_{seg}-axis with the segment chord,

$$\mathbf{r}_a = M_y \mathbf{r}_{seg}, \; M_y = \begin{bmatrix} \cos\gamma & 0 & \sin\gamma \\ 0 & 1 & 0 \\ -\sin\gamma & 0 & \cos\gamma \end{bmatrix}, \tag{9.6}$$

where γ is the rotational angle, is the sum of the pitch angle of the blade and the

local twist angle of the segment, as defined in Chapter 8.

9.2.2 Emission frequency

To calculate the Doppler factor, we follow the methodology proposed by [150], defining the Doppler factor as:

$$\frac{\omega_e}{\omega} = \frac{1 + (\mathbf{M}_0 - \mathbf{M}_s) \cdot \hat{CO}}{1 + \mathbf{M}_f \cdot \hat{CO}}, \tag{9.7}$$

where $\mathbf{M}_0$ is the free-stream Mach vector, $\mathbf{M}_s$ is the segment Mach number $\mathbf{M}_s = (\Omega r_a / c_0)[-\sin\theta, \cos\theta, 0]$, and $\hat{CO}$ is the unitary vector between the convected noise source ($\vec{x}_c$) and the observer location in the frame of the wind turbine ($\vec{r_{WT}}$),

$$\hat{CO} = \frac{\mathbf{x}_c - \mathbf{r}_{WT}}{|\mathbf{x}_c - \mathbf{r}_{WT}|}, \tag{9.8}$$

where $\mathbf{x}_c$ is the location of the convected noise source generated at $\mathbf{x}_e$ that is shifted because of the velocity,i.e., using the retarded time concept introduce in Section 6.2. The emission position is located at the middle of the blade segment, $\mathbf{x}_e = -r_a[-\sin\theta, \cos\theta, 0]$, whereas $\mathbf{x}_c$ is calculated by rearranging 6.15,

$$\mathbf{x}_c = \mathbf{x}_e + \mathbf{M}_0 R; \tag{9.9}$$

where R is the phase radius and accounts for the propagation time of the noise as defined in [20].

9.3 AL coupling

In the method proposed in this Chapter, the coupling between AL and the strip theory, can be performed considering a time-averaged blade loading, or instantaneous one at each azimuthal location. The latter would account for non-axisymmetric or transient phenomena that might occur in the inflow, for example due to an atmospheric turbulent boundary layer or by the wake of an upstream wind turbine.

In the averaged approach, at each segment there is only one angle of attack and ap-

parent velocity, thus the boundary layer parameters are considered constant along the azimuthal rotation. In consequence, also the wall pressure spectra is, as it is calculated from 7.6, using only one XFOIL simulation per segment. The changes at each azimuthal position is only geometrical, updating only the distance (9.6) and emission frequency (9.7) per segment, position and frequency, to finally performed the corresponding summation and integral.

On the other hand, for the instantaneous approach, the boundary layers parameters are calculated at each azimuthal position (at a fix number of time steps), for each segment of each blade. Therefore, plenty of XFOIL simulations are required per segment, requiring more cost compared to the averaged case, but that are several orders of magnitude lower than the AL simulation, and with the advantage that obtaining variations in the wall pressure spectra in time. In this case, (9.2) is no longer valid as it is, since each blade is now independent of each other, and the integral of each is necessary.

In cases where the inflow is uniform and constant for all azimuthal angles, the trailing-edge noise can be computed either using the loading results of the approach that consider averaged values or the AL instantaneous results providing loading values at each azimuthal angle. Under these conditions, both approaches are almost identical since the blade loading does not vary significantly over a rotation. However, if non-axisymmetric flow conditions are present in the rotor plane, and the blades are submitted to variable loadings at each azimuthal angle, averaged approaches and corresponding average noise are not fully correct, since the models are highly non-linear.

9.4 Numerical results

In this Section we validate the methodology for predicting the wind turbine noise. The test case is the Siemens SWT-2.3-93 wind turbine, a three-blade horizontal axis wind turbine located in the Høvsøre Wind Turbine Test Center in the northwest of Denmark. It has a nominal rated power of 2.3 MW. The rotor diameter is 93 m, and the hub height is 80 m.

Noise measurements at three different operating conditions are reported in [103]. The acoustic and met-mast measurements, operational curves, and wind turbine

CAD are available in the database [35]. The noise is predicted using two operational conditions, summarized in Table 9.1. The inflow turbulence conditions at the hub height are calculated from atmospheric LES simulations reported in [80] for a specific operational condition. However, the same turbulence parameters are used for other operational conditions, assuming that the atmospheric turbulence does not vary significantly as a function of the wind speed. The turbulence intensity and turbulence integral length scale at the hub height, needed to predict LE noise, are Tu_0 =10.7%, and L =300 m. The noise is measured at the ground at 100 m downwind of the wind turbine, such that $r_{WT} = [100, 0, -800]^T$.

Operational condition	U_0 [m/s]	Ω [rpm]	θ_p [deg]
O.C. 1	9.5	17	5
O.C. 2	6.0	13	3

Table 9.1: Operational conditions of the wind turbine.

The wind turbine simulations are performed using Large Eddy Simulation (LES) coupled with the AL model, with the blades divided into 23 segments. The mesh used is a fully cartesian grid in a rectangular prism domain of dimensions $[28R, 18R, 10R]$, with a constant size region near the turbine and stretching in the far field for all the directions except the vertical one, where it is only at the top. This results in a mesh consisting of approximately $99,600$ hexahedral elements, each of them enriched with Gauss-Legendre nodes of 4^{th} polynomial order (5^{th} order accuracy), obtaining almost 12.45 millions of degrees of freedom (DoF). A lateral view of the h-mesh can be seen in Figure 9.1. At the central refined region, there is approximately 29 DoF per blade radius. To close the LES model, the classical Smagorinky [152] model is used, along with the Lax-Friederichs Riemann solver and the Bassi-Rebay 1 (BR1) scheme to discretise the viscous fluxes.

In Fig. 9.2, the flow visualization of the AL simulation of O.C. 1 is presented using the Q-criteria. It can be seen that downstream the rotor plane up to two times the rotor diameter, the identity of the wake is maintained, clearly reflecting the rotational motion of the blades. Further downstream, the structures break down due to enhanced shear and mixing and tend to become more homogeneous. Figure 9.2 also shows a vertical slice of the velocity, where the transition to turbulence of the wake is observed. The AL methodology implemented in the high-order solver captures the tip vortex and wake development with a considerable level of detail.

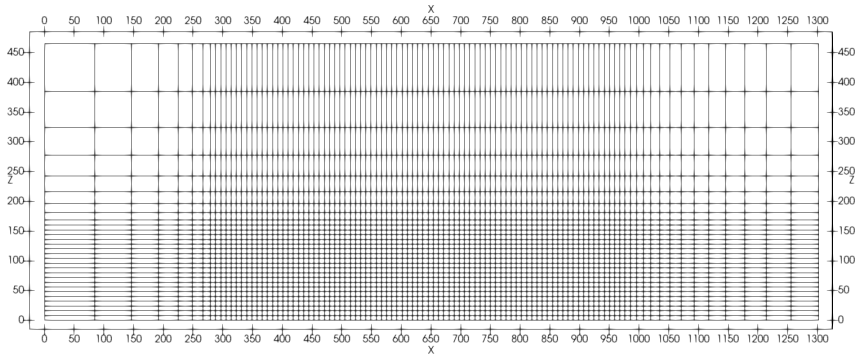


Figure 9.1: Lateral view of the h-mesh.

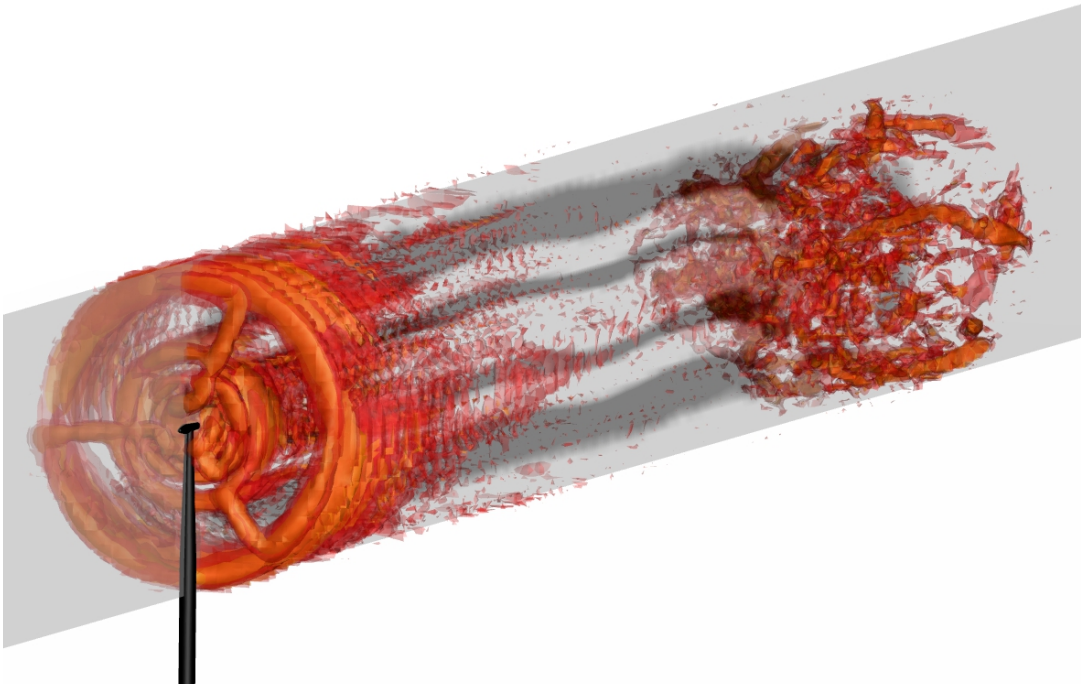
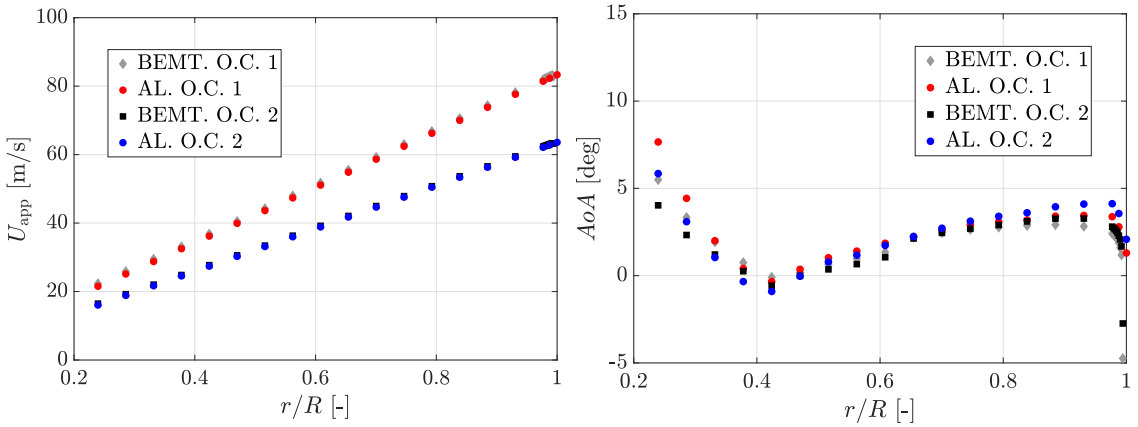


Figure 9.2: Iso-countours of the Q-criteria and vertical slice of the magnitude of the velocity for the AL simulation at O.C. 1. The tower and nacelle are included for visualization purposes only.

To validate the aerodynamic results of the AL simulations, we use blade element momentum theory (BEMT) simulations of the wind turbine under the same operational conditions to compare the noise inputs with AL simulations. The BEMT solutions are obtained using the OpenFAST code [15], which includes the Prandlt tip and root loss factor and the Pitt/Peters skewed-wake correction model. Results are presented in Figure 9.3, where the time-averaged local apparent velocity and

angle of attack along one blade obtained with AL and BEMT simulations are compared. Almost perfect agreement is obtained for the velocity while minor differences are found in the angle of attack, while negligible for changing the boundary layer characteristics of the airfoils.



(a) Apparent velocity

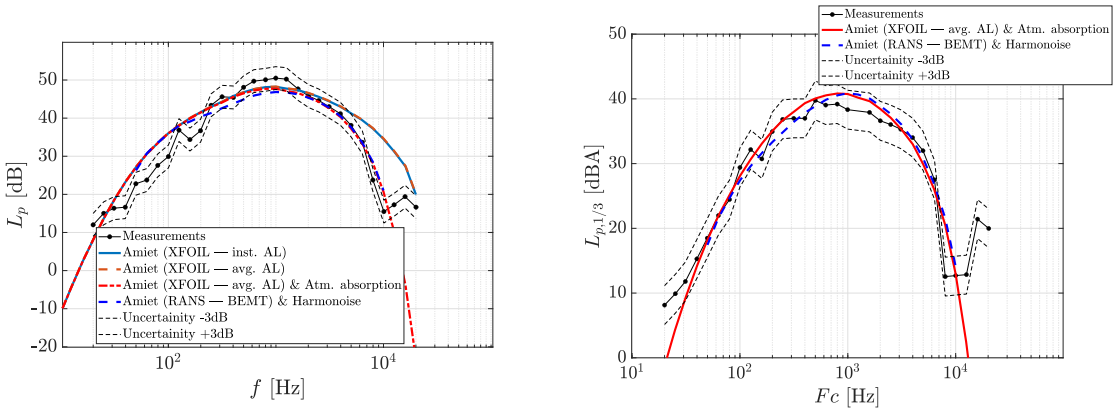
(b) Angle of attack

Figure 9.3: Comparison of apparent velocity and angle of attack distribution along the blade between actuator line averaged over one rotation and BEMT simulations.

The results of the local angle of attack, apparent velocity, and Reynolds number along a single blade are averaged over one rotation, and the instantaneous results of all three blades are saved over one rotation period at 71 angular locations, with $\Delta t = 0.05$ s, which corresponds to a $\Delta\theta = 5.1^o$. For both cases, the initial transient effects are neglected.

Figure 9.4 shows the comparison of the predicted wind turbine noise with the measurements reported in [103] for the two operational conditions shown in Table 9.1. Both operational conditions include the predicted noise with the Amiet-schlinker discussed in this paper and the same prediction accounting for the atmospheric absorption. Furthermore, for both cases, the results obtained by [20], who synthesized the wind turbine noise model using the Harmonoise model are presented. They used the blade loading obtained with BEMT model, which is the same as the ones obtained with AL simulations according to the results in the validation section. Another key difference with ref. [20] is that they use RANS numerical simulations conducted in the commercial software STAR-CCM+, which, in principle, increases the fidelity of the simulations for the extraction of the boundary layer parameters but requires a more complex setup and computational costs compared with XFOIL. For O. C. 1, an additional curve considering the instantaneous results of the actuator line simulations is included. In this case, the noise is calculated at for each segment, for each blade at each azimuth location, considering the instantaneous

results from AL, instead of the average values over one rotation.



(a) Operational condition 1.

(b) Operational condition 2.

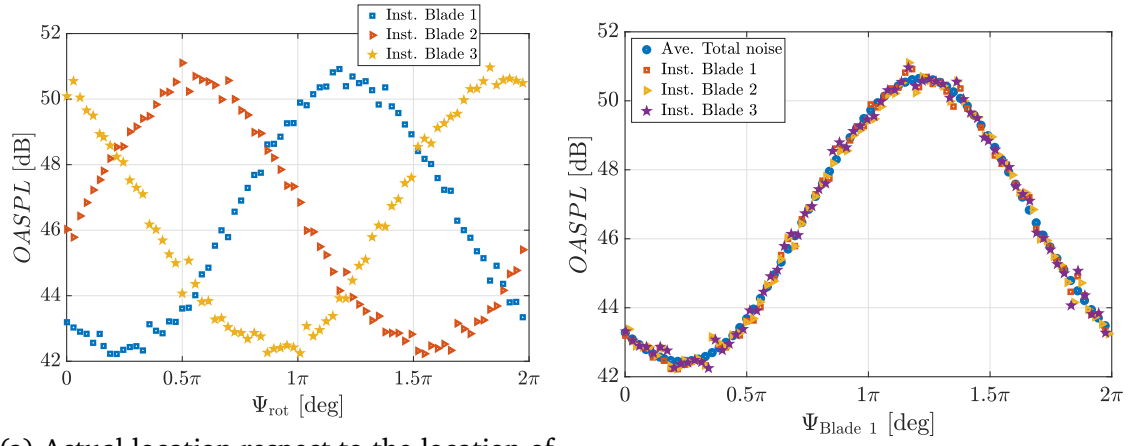
Figure 9.4: Comparison of the wind turbine noise prediction in one-third octave for several operational conditions.

For both operational conditions, the wind turbine noise prediction agrees well with field measurements up to $f \approx 1$ kHz; for higher frequencies, the prediction method overpredicts the wind turbine noise, which is significantly improved when the atmospheric absorption is taken into account. For this case, the prediction method presents a very good agreement with the measurements along the entire frequency range up to $f = 10$ kHz. There is a difference of around 4 dB in the frequency range between 20 and 100 Hz, which is probably because of a slightly different turbulence level between the atmospheric flow and the one calculated in the LES simulations since it was obtained for a different operational condition.

This good agreement validates the methodology presented in this research. Furthermore, the wind turbine noise predicted with the methodology proposed in this research matches with the results of [20], which implies that the results obtained from XFOIL are in relatively good agreement with the ones obtained from the RANS simulations, validating the use of XFOIL for the wind turbine noise prediction.

Figure 9.4a shows that there is a perfect agreement between the far-field noise predicted using instantaneous and averaged results from AL simulations, which implies that in this case, the average values are representatives of the variation along the rotor plane and that there is no sudden variation caused by transient effects of nonsymmetries on the rotor plane. One of the main advantages of having the instantaneous results of the blade loading over a blade rotation is that this

kind of phenomenon can be accounted for in the aerodynamic analysis of the wind turbine and later in the wind turbine noise prediction without expensive noise simulations. Figure 9.5a shows the OASPL for the three blades as a function of the azimuth position of blade 1 and Fig. 9.5b OASPL for the three blades as a function of the same relative azimuth position (Ψ_{rot}). The changes in the noise along the rotation for every blade shown in Fig. 9.5a are due to the change of the noise directivity along the rotation with respect to a fixed observer. This plot also shows that at every azimuth location, one blade is dominant over others. This is evident when analyzing Fig. 9.5b, where there is no deviation of the total wind turbine noise from the noise produced by each blade.



(a) Actual location respect to the location of blade 1

(b) Same relative azimuth location

Figure 9.5: OASPL of each blade using over one rotation. O.C. 1

Figure 9.5a demonstrates that the differences in the noise production are caused by the change of the directivity along the rotor location and not because of a change of the blade loading at a specific azimuth location since if the latter occurred, a difference in the noise produced among the blades at the same relative azimuth location would be observed. Although in this research there is no consideration of non-asymmetries in the rotor plane or significant changes in the blade loading over a rotation, this methodology has the potential of considering them by modeling on the aerodynamic analysis of the wind turbine, which has not been reported before with fast turn-around methods.

9.5 Summary

In this chapter we have coupled the AL DGSEM method with Schlinker and Amiet's theory, enabling the computation of the noise of the turbine. The proposed method is very efficient and takes into account the most important sources of noise in modern wind turbines. It has been tested in a real size turbine, the SWT 2.3 MW of a diameter of 90 m. The noise produced by the SWT wind turbine is compared with the noise measured in real conditions, obtaining good agreement in both, frequency and amplitudes.

A vital advantage of this method is that the wind turbine noise can be calculated using the blade loading at each azimuth location instead of averaged values over a rotation, allowing taking into account the effects of changes in the blade loading caused by, for example, gusts or wake of upstream wind turbines.

Conclusions

The goal of this thesis is simulate aeroacoustics of wind turbines using high–order numerical methods. We use a Discontinuous Galerkin Spectral Element Method (DGSEM), which makes it possible to perform time-acurate simulations efficiently. The main advantage of this method is that it has the properties of lower dissipative and dispersion errors, compared to classical low-order methods.

We have studied fundamental phenomena that are intrinsically related to aeroacoustics, such as numerical resolution, which is directly related to noise generation. We have studied turbulent flows where the mesh is not enough to capture all the small eddies that can be encountered in these kinds of scenarios. This is achieved with different strategies such as explicit Large Eddy Simulations (LES), and an implicit version of if (iLES), changing the numerical discretisation of the standard DGSEM to make it energy conserving, or by adding enough dissipation in the form of jump penalty methods, related with the fluxes in the faces. We have successfully applied all of these techniques in complex canonical cases, such as the turbulent channel, the Taylor-Green Vortex problem, the Kelvin-Helmholtz Instability, and a NACA0012 airfoil. Comparisons among them and more refined solutions have been performed, obtaining good agreement and making it clear when one strategy can be better for certain cases.

Later, different approaches to compute the aeroacoustics of airfoils have been studied. We start from the most expensive and with higher fidelity, the Direct Noise Computation, comparing the effects of the forced transition of the boundary layer and the polynomial refinement. Then, we reduced the mesh requirements by using the Ffowcs-Williams and Hawkings aeroacoustic analogy to propagate the noise

into the far field. We validated the coupling of this analogy with the DGSEM simulations and compared the results in the same NACA0012 case. In both methods, spectral convergence is achieved, as suggested by the theory in linear cases, but on this occasion for a much more complex case. Finally, we significantly reduced the cost using the semi-analytical model of Amiet to compute the leading- and trailing-edge noise of airfoils, which allows fast yet accurate predictions for wind turbines.

Finally, we have computed the aerodynamic and aeroacoustic of wind turbines using LES DGSEM simulations, combined with the Actuator Line model, which replaces the actual wind turbine geometry with moving source terms. Different approaches of this coupling are studied, as well as the mesh requirements, both in h-mesh and polynomial order. The aeroacoustic is computed using strip theory combined with the already validated Amiet's model, using the aerodynamic results of the AL simulations. Good agreement with experimental measurements in the field is achieved.

Future work

As future work of this research we can highlight some key aspects:

- A further detailed understanding of explicit LES models can be achieved in high-order. The noncontinuity of the gradients in interior element faces and the simple definition of the filter width are still topics of research.
- The jump penalty method was tested in cases without walls, and further analysis can be performed in these kinds of cases. Furthermore, how it can be convined with explicit LES models is another research that has not been addressed.
- The computation of a fully resolved turbulent airfoil for aeroacoustic computation had not been addressed using DGSEM, either with direct approach or with the FWH analogy. Relating the LES model or the iLES numerics with the good prediction of the acoustic pressure, especially for high Reynolds numbers, is interesting from a practical point of view.
- Amiet's theory proposed in Chapter 7 uses the boundary layer solution of an airfoil. Coupling it with LES or iLES simulations can be achieved with very

straightforward use of the models and numerical tools developed in this thesis. The time averaged pressure coefficient and velocity profile at the trailing edge vecinity is somehow simple once we get a statistically converged flow. In this way, we will not be using semi-empirical models, increasing the fidelity of the acoustic predictions.

- Continuing the previous line, the Amiet-schlinker model used in Chapter 9 to predict the noise of the complete wind turbine uses the same models. A more expensive but higher-fidelity approach can be done by performing a series of LES simulations of each airfoil section and using the results to calculate the boundary layer parameters. This has the disadvantage of being extremely costly for unsteady conditions, but might be the best approach if the code can be optimised for airfoil LES simulations, and in the near future the increase of HPC resources continues. In any case, this is a cheaper approach than solving the complete geometry of the blade in rotatory LES frameworks.

Appendices

The Governing Equations

.1 Navier-Stokes equations

The compressible Navier–Stokes equations in the general form are expressed as,

$$\begin{aligned} \rho_t + \nabla \cdot (\rho \mathbf{u}) &= s_\rho, \\ (\rho \mathbf{u})_t + \nabla \cdot (\rho \mathbf{u}\mathbf{u}) &= -\nabla p + \nabla \cdot \tau + \mathbf{s}_{\rho \mathbf{u}}, \\ (\rho E)_t + \nabla \cdot (\mathbf{u}(\rho E + p)) &= \nabla \cdot (\tau \cdot \mathbf{u} + \kappa_{th} \nabla T) + s_{\rho E}, \end{aligned} \tag{10}$$

where ρ is the density, $\mathbf{u} = [u_x, u_y, u_z]^T$ is the velocity vector, ρE is the total energy, the sum of the internal and kinetic energy, and s_i are individual source terms of each equation. It can also be written in non-dimensional and conservative form as

$$\mathbf{q}_t + \nabla \cdot \mathbf{f}_a - \nabla \cdot \mathbf{f}_v = \mathbf{s}, \tag{11}$$

by defining $\mathbf{q} = [\rho, \rho \mathbf{u}, \rho E]^T$ as the state vector, $\mathbf{s}$ the source term vector, and $\mathbf{f}_a$ and $\mathbf{f}_v$ are the inviscid and viscous flux tensors respectively. This fluxes have the following form,

$$\mathbf{f}_a(\mathbf{q}) = \begin{bmatrix} \rho \mathbf{u} \\ \rho \mathbf{u} \otimes \mathbf{u} + \mathbf{I} p \\ \mathbf{u}(\rho E + p) \end{bmatrix}, \quad \mathbf{f}_v(\mathbf{q}, \nabla \mathbf{q}) = \frac{1}{\mathrm{Re}} \begin{bmatrix} 0 \\ \tau \\ \tau \mathbf{u} + \kappa \nabla T \end{bmatrix}, \tag{12}$$

where $\mathrm{Re} = V_0 L_0 \rho_0 / \mu_0$ is the Reynolds number based on the reference values that are used to perform the nondimensionalization (velocity, length, density and viscosity respectively), and κ is the nondimensional conductivity, calculated as,

$$\kappa = \frac{\mu}{(\gamma - 1)\,\mathrm{Pr} M_0}, \tag{13}$$

being μ the nondimensional viscosity, τ is the stress tensor, $\mathrm{Pr} = c_p \mu / \kappa_{th}$ the Prandtl number, $\gamma = c_p / c_v$ the heat capacity ratio, $M_0 = V_0 / c_0$ the reference Mach number, $c_0 = \sqrt{\gamma p_0 / \rho_0}$ is the reference speed of sound, and κ_{th} is the molecular conductivity of the fluid. For all the applications in this thesis standard air parameters are used, i.e. $\mathrm{Pr} = 0.72$ (assume to be constant) and $\gamma = 1.4$. The viscosity is computed using the Sutherland's law,

$$\mu = \frac{1 + T_{suth}/T_\infty}{T + T_{suth}/T_\infty} T^{\frac{3}{2}}, \tag{14}$$

with $T_{suth} = 110.4K$ is the Sutherland's temperature. The stress tensor is calculated using Stokes hypothesis,

$$\tau = \mu\left((\nabla \mathbf{u})^T + \nabla \mathbf{u}\right) - \lambda \nabla \cdot \mathbf{u}\mathbf{I}, \tag{15}$$

where $\lambda = -\frac{2}{3}\mu$ is the bulk viscosity coefficient. The pressure is computed using the calorically perfect gas approximation,

$$p = (\gamma - 1)\,\rho e, \tag{16}$$

where $e = E - ||\mathbf{u}||^2$ is the internal energy.

Bibliography

[1] K. Abrahamsen. The ship as an underwater noise source. *Proceedings of Meetings on Acoustics*, 17(1), 2012. Cited on page(s) 1.

[2] M. Alhawwary and Z. Wang. Implementation of a fwh approach in a high-order les tool for aeroacoustic noise predictions. *AIAA Scitech 2020 Forum*, 2020. Cited on page(s) 71, 74.

[3] M. Alhawwary and Z. J. Wang. Fourier analysis and evaluation of dg, fd and compact difference methods for conservation laws. *Journal of Computational Physics*, 373:835–862, 2018. Cited on page(s) 41.

[4] R. Amiet. Acoustic radiation from an airfoil in a turbulent stream. *Journal of Sound and Vibration*, 41(4):407–420, 1975. Cited on page(s) 86.

[5] R. Amiet. Noise due to turbulent flow past a trailing edge. *Journal of Sound and Vibration*, 47(3):387–393, 1976. Cited on page(s) 87, 88, 126.

[6] R. Arina. Validation of a discontinuous galerkin implementation of the time-domain linearized navier–stokes equations for aeroacoustics. *Aerospace*, 3(7), 2016. Cited on page(s) 71.

[7] J. Bartl and L. Sætran. Blind test comparison of the performance and wake flow between two in-line wind turbines exposed to different turbulent inflow conditions. *Wind energy science*, 2(1):55–76, 2017. Cited on page(s) 104.

[8] F. Bassi and S. Rebay. A high-order accurate discontinuous finite element method for the numerical solution of the compressible navier–stokes equations. *Journal of Computational Physics*, 131(2):267 – 279, 1997. Cited on page(s) 21.

[9] A. Beck and C.-D. Munz. Direct aeroacoustic simulations based on high order discontinuous galerkin schemes. In *Computational Acoustics*, pages 159–204. Springer International Publishing, jul 2017. Cited on page(s) xv, 56, 64, 65, 70, 71.

[10] A. D. Beck, T. Bolemann, D. Flad, H. Frank, G. J. Gassner, F. Hindenlang, and C.-D. Munz. High-order discontinuous galerkin spectral element methods for transitional and turbulent flow simulations. *International Journal for Numerical Methods in Fluids*, 76(8):522–548, aug 2014. Cited on page(s) 31.

[11] P. Birken, G. Gassner, M. Haas, and C. D. Munz. Preconditioning for modal discontinuous Galerkin methods for unsteady 3D Navier-Stokes equations. *Journal of Computational Physics*, 240:20–35, 2013. Cited on page(s) 22.

[12] H. Blackburn and S. Schmidt. Spectral element filtering techniques for large eddy simulation with dynamic estimation. *Journal of Computational Physics*, 186(2):610 – 629, 2003. Cited on page(s) 28.

[13] G. Blaisdell, E. Spyropoulos, and J. Qin. The effect of the formulation of nonlinear terms on aliasing errors in spectral methods. *Applied Numerical Mathematics*, 21(3):207–219, jul 1996. Cited on page(s) 28.

[14] W. K. Blake. *Mechanics of flow-induced sound and vibration, Volume 2: Complex flow-structure interactions*. Academic press, 2017. Cited on page(s) 89.

[15] P. Bortolotti, M. Masciola, S. Ananthan, M. J. Schmidt, J. Rood, N. Mendoza, M. Hai, S. L.and Hall, A. Sharma, K. Shaler, K. Bendl, P. Schuenemann, P. Sakievich, E. W. Quon, M. R. Phillips, N. Kusouno, A. Gonzalez Salcedo, T. Martinez, and R. Corniglion. Openfast, 01 2022. Cited on page(s) 126, 132.

[16] M. Braack, E. Burman, V. John, and G. Lube. Stabilized finite element methods for the generalized oseen problem. *Computer Methods in Applied Mechanics and Engineering*, 196(4-6):853–866, 2007. Cited on page(s) 28.

[17] K. S. Brentner, J. S. Cox, C. L. Rumsey, and B. A. Younis. Computation of sound generated by flow over a circular cylinder: An acoustic analogy approach. 1997. Cited on page(s) 79.

[18] K. S. Brentner and F. Farassat. Modeling aerodynamically generated sound of helicopter rotors. *Progress in Aerospace Sciences*, 39(2-3):83–120, feb 2003. Cited on page(s) 71, 73.

[19] G. Brès, F. Pérot, and D. Freed. A ffowcs williams - hawkings solver for lattice-boltzmann based computational aeroacoustics. In *16th AIAA/CEAS Aeroacoustics Conference*. American Institute of Aeronautics and Astronautics, jun 2010. Cited on page(s) 71, 73.

[20] A. C. Bresciani, J. Maillard, S. Le Bras, and L. D. de Santana. Wind turbine noise synthesis from numerical simulations. In *AIAA AVIATION 2023 Forum*, page 3643, 2023. Cited on page(s) 129, 133, 134.

[21] A. P. Bresciani, S. Le Bras, and L. D. de Santana. Generalization of amiet's theory for small reduced-frequency and nearly-critical gusts. *Journal of sound and vibration*, 524:116742, 2022. Cited on page(s) 87.

[22] T. F. Brooks, D. Pope, and M. A. Marcolini. Airfoil self-noise and prediction. Technical report, NASA Reference Publication 1218, 1989. Cited on page(s) 55.

[23] T. F. Brooks, D. Pope, and M. A. Marcolini. Airfoil self-noise and prediction. Technical report, NASA Reference Publication 1218, 1989. Cited on page(s) 126.

[24] E. Burman and M. A. Fernández. Continuous interior penalty finite element method for the time-dependent navier–stokes equations: space discretization and convergence. *Numerische Mathematik*, 107(1):39–77, 2007. Cited on page(s) 42.

[25] E. Burman and P. Hansbo. Edge stabilization for galerkin approximations of convection–diffusion–reaction problems. *Computer methods in applied mechanics and engineering*, 193(15-16):1437–1453, 2004. Cited on page(s) 42.

[26] E. Burman, A. Quarteroni, and B. Stamm. Stabilization strategies for high order methods for transport dominated problems. *Bollettino della Unione Mate matica Italiana. Serie*, 9(1):57–77, 2008. Cited on page(s) 28.

[27] C. Canuto, M. Y. Hussaini, A. Quarteroni, and T. A. Zang. *Spectral Methods: Fundamentals In Single Domains*, volume 1. Springer-Verlag Berlin Heidelberg, 2006. Cited on page(s) 2.

[28] C. Canuto, M. Y. Hussaini, A. Quarteroni, and T. A. Zang. *Spectral Methods. Evolution to Complex Geometries and Applications to Fluid Dynamics*. Springer, 2007. Cited on page(s) 2.

[29] M. Carley and J. Fitzpatrick. Linear acoustic formulae for calculation of rotating blade noise with asymmetric inflow. In *Aeroacoustics Conference*. American Institute of Aeronautics and Astronautics, may 1996. Cited on page(s) 72.

[30] M. H. Carpenter, T. C. Fisher, E. J. Nielsen, and S. H. Frankel. Entropy stable spectral collocation schemes for the navier–stokes equations: Discontinuous interfaces. *SIAM Journal on Scientific Computing*, 36(5):B835–B867, jan 2014. Cited on page(s) 32.

[31] D. M. Chase. Modeling the wavevector-frequency spectrum of turbulent boundary layer wall pressure. *Journal of sound and Vibration*, 70(1):29–67, 1980. Cited on page(s) 89.

[32] M. Chávez-Modena, E. Ferrer, and G. Rubio. Improving the stability of multiple-relaxation lattice boltzmann methods with central moments. *Computers & Fluids*, 172:397–409, aug 2018. Cited on page(s) 49.

[33] Z. Cheng, F.-S. Lien, E. Yee, and H. Meng. A unified framework for aeroacoustics simulation of wind turbines. *Renewable Energy*, 188:299–319, apr 2022. Cited on page(s) xv, 78, 79, 80, 126.

[34] H. S. Chivaee. *Large Eddy Simulation of Turbulent Flows in Wind Energy*. PhD thesis, DTU Wind Energy, Jan. 2014. Cited on page(s) 98.

[35] J. Christophe, S. Buckingham, C. Schram, and S. Oerlemans. zephyr - large on shore wind turbine benchmark. *Zenodo*, Mar. 2022. Cited on page(s) 131.

[36] M. J. Churchfield, S. Lee, J. Michalakes, P. J. Moriarty, G. Vijayakumar, J. G. Brasseur, C. White, C. Draxl, and J. L. Coen. A large-eddy simulation of wind-plant aerodynamics. *Flow, Turbulence and Combustion*, 88(4):507–541, 2012. Cited on page(s) 98.

[37] J. Colas, A. Emmanuelli, D. Dragna, P. Blanc-Benon, B. Cotté, and R. J. A. M. Stevens. Wind turbine sound propagation: Comparison of a linearized euler equations model with parabolic equation methods. *The Journal of the Acoustical Society of America*, 154(3):1413–1426, sep 2023. Cited on page(s) 126.

[38] D. Coles. The law of the wake in the turbulent boundary layer. *Journal of Fluid Mechanics*, 1(2):191–226, 1956. Cited on page(s) 90.

[39] G. M. Corcos. The structure of the turbulent pressure field in boundary-layer flows. *Journal of Fluid Mechanics*, 18(3):353–378, 1964. Cited on page(s) 88.

[40] J. L. Davy, K. Burgemeister, and D. Hillman. Wind turbine sound limits: Current status and recommendations based on mitigating noise annoyance. *Applied Acoustics*, 140:288–295, 2018. Cited on page(s) 1.

[41] L. de Santana. *Semi-analytical methodologies for airfoil noise prediction*. PhD thesis, KU Leuven, 2015. Cited on page(s) 87.

[42] H. Debertshaeuser, W. Z. Shen, and W. J. Zhu. Aeroacoustic calculations of wind turbine noise with the actuator line/ navier-stokes technique. In *34th Wind Energy Symposium*. American Institute of Aeronautics and Astronautics, jan 2016. Cited on page(s) 126.

[43] H. Debertshäuser, W. Shen, and W. Zhu. Development of a high-fidelity noise prediction and propagation model for noise generated from wind turbines. In *Proceedings. 6th International Meeting on Wind Turbine Noise*, 2015. 6th International Meeting on Wind Turbine Noise ; Conference date: 20-04-2015 Through 23-04-2015. Cited on page(s) 126.

[44] R. Della Ratta Rinaldi, A. Iob, and R. Arina. An efficient discontinuous galerkin method for aeroacoustic propagation. *International Journal for Numerical Methods in Fluids*, 69(9):1473–1495, 2012. Cited on page(s) 71.

[45] G. Deskos, S. Laizet, and R. Palacios. Winc3d: A novel framework for turbulence-resolving simulations of wind farm wake interactions. *Wind Energy*, 23(3):779–794, 2020. Cited on page(s) 99.

[46] G. Deskos, S. Laizet, and M. D. Piggott. Turbulence-resolving simulations of wind turbine wakes. *Renewable Energy*, 134:989–1002, 2019. Cited on page(s) 99, 108.

[47] G. Deskos and M. D. Piggott. Mesh-adaptive simulations of horizontal-axis turbine arrays using the actuator line method. *Wind Energy*, 21(12):1266–1281, 2018. Cited on page(s) 99.

[48] P. di Francescantonio. A NEW BOUNDARY INTEGRAL FORMULATION FOR THE PREDICTION OF SOUND RADIATION. *Journal of Sound and Vibration*, 202(4):491–509, may 1997. Cited on page(s) 71.

[49] P. Doubrawa, E. W. Quon, L. A. Martinez-Tossas, K. Shaler, M. Debnath, N. Hamilton, T. G. Herges, D. Maniaci, C. L. Kelley, A. S. Hsieh, M. L. Blaylock, P. van der Laan, S. J. Andersen, S. Krueger, M. Cathelain, W. Schlez, J. Jonkman, E. Branlard, G. Steinfeld, S. Schmidt, F. Blondel, L. J. Lukassen, and P. Moriarty. Multimodel validation of single wakes in neutral and stratified atmospheric conditions. *Wind Energy*, 23(11):2027–2055, 2020. Cited on page(s) 98.

[50] J. Douglas and T. Dupont. Interior penalty procedures for elliptic and parabolic galerkin methods. In *Computing methods in applied sciences*, pages 207–216. Springer, 1976. Cited on page(s) 22, 42.

[51] M. Drela. Xfoil: An analysis and design system for low reynolds number airfoils. In *Low Reynolds number aerodynamics*, pages 1–12. Springer, 1989. Cited on page(s) 90.

[52] M. Drela and M. B. Giles. Viscous-inviscid analysis of transonic and low reynolds number airfoils. *AIAA Journal*, 25(10):1347–1355, oct 1987. Cited on page(s) 90.

[53] R. Ewert and W. Schröder. Acoustic perturbation equations based on flow decomposition via source filtering. *Journal of Computational Physics*, 188(2):365–398, July 2003. Cited on page(s) 70, 126.

[54] F. Farassat. Derivation of formulations 1 and 1a of farassat. Technical report, NASA Technical Reports Server : NTRS, 2007. Cited on page(s) 71, 73.

[55] F. Farassat and G. Succi. A review of propeller discrete frequency noise prediction technology with emphasis on two current methods for time domain calculations. *Journal of Sound and Vibration*, 71(3):399–419, aug 1980. Cited on page(s) 71.

[56] E. Ferrer. An interior penalty stabilised incompressible discontinuous galerkin–fourier solver for implicit large eddy simulations. *Journal of Computational Physics*, 348:754–775, nov 2017. Cited on page(s) 28, 42, 45, 52, 57.

[57] E. Ferrer, J. Manzanero, A. M. Rueda-Ramirez, G. Rubio, and E. Valero. Implicit large eddy simulations for NACA0012 airfoils using compressible and incompressible discontinuous galerkin solvers. In *Lecture Notes in Computational Science and Engineering*, pages 477–487. Springer International Publishing, 2020. Cited on page(s) 32, 57.

[58] E. Ferrer, G. Rubio, G. Ntoukas, W. Laskowski, O. Mariño, S. Colombo, A. Mateo-Gabín, H. Marbona, F. M. de Lara, D. Huergo, J. Manzanero, A. Rueda-Ramírez, D. Kopriva, and E. Valero. : A high-order discontinuous galerkin solver for flow simulations and multi-physics applications. *Computer Physics Communications*, 287:108700, jun 2023. Cited on page(s) 6, 120.

[59] T. C. Fisher and M. H. Carpenter. High-order entropy stable finite difference schemes for nonlinear conservation laws: Finite domains. *Journal of Computational Physics*, 252:518–557, nov 2013. Cited on page(s) 31, 32.

[60] I. E. Garrick, C. E. Watkins, I. E. Garrick, and C. E. Watkins. A theoretical study of the effect of forward speed on the free-space sound-pressure field around propellors. Technical report, NASA Technical Reports Server : NTRS, 1954. Cited on page(s) 72.

[61] G. Gassner, A. Winters, F. Hindenlang, and D. Kopriva. The br1 scheme is stable for the compressible navier–stokes equations. *Journal Scientific Computing*, 77:154––200, 2018. Cited on page(s) 31, 46.

[62] G. J. Gassner. A skew-symmetric discontinuous galerkin spectral element discretization and its relation to SBP-SAT finite difference methods. *SIAM Journal on Scientific Computing*, 35(3):A1233–A1253, jan 2013. Cited on page(s) 28, 31.

[63] G. J. Gassner and A. D. Beck. On the accuracy of high-order discretizations for underresolved turbulence simulations. *Theor. Comput. Fluid Dyn.*, 27:221–237, 2013. Cited on page(s) 41.

[64] G. J. Gassner, A. R. Winters, and D. A. Kopriva. Split form nodal discontinuous galerkin schemes with summation-by-parts property for the compressible euler equations. *Journal of Computational Physics*, 327:39–66, dec 2016. Cited on page(s) 31, 32, 35, 45, 57.

[65] G. Ghorbaniasl, Z. Huang, L. Siozos-Rousoulis, and C. Lacor. Analytical acoustic pressure gradient prediction for moving medium problems. *Proceedings of the Royal Society A: Mathematical, Physical and Engineering Sciences*, 471(2184):20150342, dec 2015. Cited on page(s) 71.

[66] G. Ghorbaniasl and C. Lacor. A moving medium formulation for prediction of propeller noise at incidence. *Journal of Sound and Vibration*, 331(1):117–137, jan 2012. Cited on page(s) 71.

[67] S. Glegg and W. Devenport. *Aeroacoustics of Low Mach Number Flows*. Academic Press, 2017. Cited on page(s) 87, 88.

[68] M. E. Goldstein. A generalized acoustic analogy. *Journal of Fluid Mechanics*, 488:315–333, jul 2003. Cited on page(s) 70.

[69] M. Goody. Empirical spectral model of surface pressure fluctuations. *AIAA journal*, 42(9):1788–1794, 2004. Cited on page(s) 89.

[70] T. Götz, G. Hastie, L. Hatch, O. Raustein, B. Southall, M. Tasker, F. Thomsen, J. Campbell, and B. Fredheim. Overview of the impacts of anthropogenic underwater sound in the marine environment. Technical report, OSPAR Commission, 2009. Cited on page(s) 1.

[71] C. H. Hansen, C. J. Doolan, and K. L. Hansen. *Wind farm noise: measurement, assessment, and control*. John Wiley & Sons, 2017. Cited on page(s) 125.

[72] M. Herr, C. J. Bahr, and M. Kamruzzaman. Problem statement for the aiaa/ceas second workshop on benchmark problems for airframe noise computations (banc-ii). In *Workshop documentation: https://info. aiaa. org/tac/ASG/FDTC/DG/BECAN_files_/BANCII_category1*, 2012. Cited on page(s) xvi, 91, 92.

[73] J. S. Hesthaven and T. Warburton. *Nodal Discontinuous Galerkin Methods*. Springer New York, 2008. Cited on page(s) 28.

[74] F. Hindenlang, G. J. Gassner, C. Altmann, A. Beck, M. Staudenmaier, and C. D. Munz. Explicit discontinuous Galerkin methods for unsteady problems. *Computers and Fluids*, 61:86–93, 2012. Cited on page(s) 22.

[75] S. Hoyas and J. Jiménez. Reynolds number effects on the reynolds-stress budgets in turbulent channels. *Physics of Fluids*, 20(10), oct 2008. Cited on page(s) xiii, 34.

[76] N. Hu and M. Herr. Characteristics of wall pressure fluctuations for a flat plate turbulent boundary layer with pressure gradients. In *22nd AIAA/CEAS Aeroacoustics Conference*, page 2749, 2016. Cited on page(s) 89.

[77] H. H. Hubbard and K. P. Shepherd. Wind turbine acoustics. Technical report, NASA Langley Research Center, 2009. Cited on page(s) 1.

[78] J. Hunt, A. Wray, and P. Moin. Eddies, streams, and convergence zones in turbulent flows. *Studying Turbulence Using Numerical Simulation Databases*, pages 193–208, 11 1988. Cited on page(s) 37.

[79] L. E. Jones and R. D. Sandberg. Numerical analysis of tonal airfoil self-noise and acoustic feedback-loops. *Journal of Sound and Vibration*, 330(25):6137–6152, Dec. 2011. Cited on page(s) 64, 65, 67.

[80] B. Kale. *ABL simulations with uncertain weather parameters and impact on WT performance and near-field noise*. PhD thesis, PhD thesis, Universidad Politécnica de Madrid, 2023. Cited on page(s) 131.

[81] M. Kamruzzaman, D. Bekiropoulos, T. Lutz, W. Würz, and E. Krämer. A semi-empirical surface pressure spectrum model for airfoil trailing-edge noise prediction. *International Journal of Aeroacoustics*, 14(5-6):833–882, 2015. Cited on page(s) 89, 91.

[82] S. Kang, M. Esmaily-Moghadam, and K. Bhaganagar. Large-eddy simulation of a wind turbine wake: Comparison between actuator-line and disk models. *Wind Energy Science*, 4(1):129–144, 2019. Cited on page(s) 98.

[83] G. E. Karniadakis and S. J. Sherwin. *Spectral/hp element methods for CFD*. OUP, 2005. Cited on page(s) 2.

[84] C. A. Kennedy and A. Gruber. Reduced aliasing formulations of the convective terms within the navier–stokes equations for a compressible fluid. *Journal of Computational Physics*, 227(3):1676–1700, jan 2008. Cited on page(s) 33, 35.

[85] R. M. Kirby and G. E. Karniadakis. De-aliasing on non-uniform grids: algorithms and applications. *Journal of Computational Physics*, 191(1):249–264, Oct. 2003. Cited on page(s) 28.

[86] R. M. Kirby and S. J. Sherwin. Aliasing errors due to quadratic nonlinearities on triangular spectral /hp element discretisations. *Journal of Engineering Mathematics*, 56(3):273–288, Oct. 2006. Cited on page(s) 28.

[87] R. M. Kirby and S. J. Sherwin. Stabilisation of spectral/hp element methods through spectral vanishing viscosity: Application to fluid mechanics modelling. *Computer Methods in Applied Mechanics and Engineering*, 195(23-24):3128–3144, apr 2006. Cited on page(s) 28.

[88] M. Kompenhans, G. Rubio, E. Ferrer, and E. Valero. Adaptation strategies for high order discontinuous galerkin methods based on tau-estimation. *Journal of Computational Physics*, 306:216 – 236, 2016. Cited on page(s) 2.

[89] M. Kompenhans, G. Rubio, E. Ferrer, and E. Valero. Comparisons of p-adaptation strategies based on truncation- and discretisation-errors for high order discontinuous galerkin methods. *Computers and Fluids*, 139:36 – 46, 2016. Cited on page(s) 2.

[90] E. Koppen and K. Fowler. International legislation for wind turbine noise. In *Proceedings of the Euronoise*, pages 321–326. NAG, ABAV Maastricht, The Netherlands, 2015. Cited on page(s) 1.

[91] D. Kopriva. *Implementing Spectral Methods for Partial Differential Equations: Algorithms for Scientists and Engineers*. Springer, 2009. Cited on page(s) 15, 17, 35.

[92] D. A. Kopriva. A staggered-grid multidomain spectral method for the compressible navier-stokes equations. *Journal of Computational Physics*, 244:142–158, 1998. Cited on page(s) 2.

[93] D. A. Kopriva. Metric identities and the discontinuous spectral element method on curvilinear meshes. *Journal of Scientific Computing*, 26(3):301–327, Mar. 2006. Cited on page(s) 17.

[94] D. A. Kopriva and G. J. Gassner. An energy stable discontinuous galerkin spectral element discretization for variable coefficient advection problems. *SIAM Journal on Scientific Computing*, 36(4):A2076–A2099, jan 2014. Cited on page(s) 31.

[95] J. Kou, S. Joshi, A. H. de Mendoza, K. Puri, C. Hirsch, and E. Ferrer. Immersed boundary method for high-order flux reconstruction based on volume penalization. *Journal of Computational Physics*, 448:110721, 2022. Cited on page(s) 120.

[96] P.-Å. Krogstad, P. Eriksen, and J. Melheim. Blind test workshop; calculations for a model wind turbine. *Summary report*, 10, 2011. Cited on page(s) 104, 107.

[97] P.-Å. Krogstad and L. Sætran. Wind turbine wake interactions; results from blind tests. In *Journal of Physics: Conference Series*, volume 625, page 012043. IOP Publishing, 2015. Cited on page(s) 104, 113.

[98] Y. C. Küçükosman, J. Christophe, and C. Schram. Trailing edge noise prediction based on wall pressure spectrum models for naca0012 airfoil. *Journal of Wind Engineering and Industrial Aerodynamics*, 175:305–316, 2018. Cited on page(s) xvi, 91, 92.

[99] R. E. Kurt, H. Khalid, O. Turan, M. Houben, J. Bos, and I. H. Helvacioglu. Towards human-oriented norms: Considering the effects of noise exposure on board ships. *Ocean Engineering*, 120:101–107, 2016. Cited on page(s) 1.

[100] J. C. D. LAMO, J. JIMNEZ, P. ZANDONADE, and R. D. MOSER. Scaling of the energy spectra of turbulent channels. *Journal of Fluid Mechanics*, 500:135–144, jan 2004. Cited on page(s) xiii, 34.

[101] P. D. Lax. Weak solutions of nonlinear hyperbolic equations and their numerical computation. *Communications on pure and applied mathematics*, 7(1):159–193, 1954. Cited on page(s) 21.

[102] Y.-T. Lee, W. K. Blake, and T. M. Farabee. Modeling of wall pressure fluctuations based on time mean flow field. *Journal of Fluids Engineering*, 2005. Cited on page(s) 89.

[103] G. Leloudas. Optimization of wind turbines with respect to noise. master's thesis, Technical University of Denmark, Technical University of Denmark, Anker Engelunds Vej 1, Building 101A, 2800 Kgs. Lyngby, Nov. 2006. Cited on page(s) 130, 133.

[104] M. Lesieur and O. Metais. New trends in large-eddy simulations of turbulence. *Annual Review of Fluid Mechanics*, 28:45–82, 1996. Cited on page(s) 30.

[105] R. J. LeVeque et al. *Finite volume methods for hyperbolic problems*, volume 31. Cambridge university press, 2002. Cited on page(s) 21, 22.

[106] M. J. Lighthill. On sound generated aerodynamically i. general theory. *Proceedings of the Royal Society of London. Series A. Mathematical and Physical Sciences*, 211(1107):564–587, mar 1952. Cited on page(s) 70, 71.

[107] L. Liu, L. Franceschini, D. Oliveira, F. Galeazzo, B. Carmo, and R. Stevens. Evaluating the accuracy of the actuator line model against blade element momentum theory in uniform inflow. *Wind Energy*, pages 1–14, 2022. Cited on page(s) 100.

[108] D. Lockard. A comparison of ffowcs williams-hawkings solvers for airframe noise applications. In *8th AIAA/CEAS Aeroacoustics Conference & Exhibit*. American Institute of Aeronautics and Astronautics, jun 2002. Cited on page(s) xv, 71, 74, 76, 77.

[109] D. P. Lockard. An efficient, two-dimensional implementation of the ffowcs williams and hawkings equation. *Journal of Sound and Vibration*, 229(4):897–911, jan 2000. Cited on page(s) 71, 74.

[110] Y. Maday and E. Tadmor. Analysis of the spectral vanishing viscosity method for periodic conservation laws. *SIAM Journal on Numerical Analysis*, 26(4):854–870, 1989. Cited on page(s) 28.

[111] J. Manzanero, E. Ferrer, G. Rubio, and E. Valero. Design of a smagorinsky spectral vanishing viscosity turbulence model for discontinuous galerkin methods. *Computers & Fluids*, 200:104440, mar 2020. Cited on page(s) 28, 31, 41, 45, 57.

[112] J. Manzanero, G. Rubio, E. Ferrer, and E. Valero. Dispersion-dissipation analysis for advection problems with nonconstant coefficients: Applications to discontinuous galerkin formulations. *SIAM Journal on Scientific Computing*, 40(2):A747–A768, jan 2018. Cited on page(s) 28, 31.

[113] J. Manzanero, A. M. Rueda-Ramírez, G. Rubio, and E. Ferrer. The bassi rebay 1 scheme is a special case of the symmetric interior penalty formulation for discontinuous galerkin discretisations with gauss–lobatto points. *Journal of Computational Physics*, 363:1–10, jun 2018. Cited on page(s) 57.

[114] L. Martínez-Tossas, M. Churchfield, and C. Meneveau. Large eddy simulation of wind turbine wakes: detailed comparisons of two codes focusing on effects of numerics and subgrid modeling. *J Phys Conf Ser*, 625:12024, 2015. Cited on page(s) 102.

[115] S. Mendez, M. Shoeybi, S. K. Lele, and P. Moin. On the use of the ffowcs williams-hawkings equation to predict far-field jet noise from large-eddy simulations. *International Journal of Aeroacoustics*, 12(1-2):1–20, jan 2013. Cited on page(s) 71.

[116] G. Mengaldo, D. D. Grazia, D. Moxey, P. Vincent, and S. Sherwin. Dealiasing techniques for high-order spectral element methods on regular and irregular grids. *Journal of Computational Physics*, 299:56–81, Oct. 2015. Cited on page(s) 28.

[117] M. L. Minion and D. L. Brown. Performance of under-resolved two-dimensional incompressible flow simulations, II. *Journal of Computational Physics*, 138(2):734–765, dec 1997. Cited on page(s) 49, 50.

[118] R. Moura, P. Fernandez, and G. Mengaldo. Diffusion and dispersion characteristics of hybridized discontinuous Galerkin methods for under-resolved turbulence simulations. In *APS Division of Fluid Dynamics Meeting Abstracts*, pages F31–007, 2017. Cited on page(s) 45.

[119] R. Moura, S. Sherwin, and J. Peiró. Eigensolution analysis of spectral/hp continuous galerkin approximations to advection–diffusion problems: Insights into spectral vanishing viscosity. *Journal of Computational Physics*, 307:401–422, Feb. 2016. Cited on page(s) 28.

[120] R. C. Moura, A. Cassinelli, A. F. da Silva, E. Burman, and S. J. Sherwin. Gradient jump penalty stabilisation of spectral/hp element discretisation for under-resolved turbulence simulations. *Computer Methods in Applied Mechanics and Engineering*, 388:114200, 2022. Cited on page(s) 42, 44, 52.

[121] R. C. Moura, S. J. Sherwin, and J. Peiró. Linear dispersion–diffusion analysis and its application to under-resolved turbulence simulations using discontinuous galerkin spectral/hp methods. *Journal of Computational Physics*, 298:695–710, 2015. Cited on page(s) 41.

[122] A. Najafi-Yazdi, G. A. Brès, and L. Mongeau. An acoustic analogy formulation for moving sources in uniformly moving media. *Proceedings of the Royal Society A: Mathematical, Physical and Engineering Sciences*, 467(2125):144–165, jun 2010. Cited on page(s) 71, 73.

[123] A. Najafi-Yazdi, L. Mongeau, and G. Bres. An acoustic analogy formulation for uniformly moving media: Formulation 1c. In *16th AIAA/CEAS Aeroacoustics Conference*. American Institute of Aeronautics and Astronautics, jun 2010. Cited on page(s) 71.

[124] F. Nicoud and F. Ducros. Subgrid-scale stress modelling based on the square of the velocity gradient tensor. *Flow, Turbulence and Combustion*, 62:183–200, 1999. Cited on page(s) 30.

[125] E. Nieuwenhuizen and M. Köhl. Differences in noise regulations for wind turbines in four european countries. In *Proceedings of the Euronoise*, page 333, 2015. Cited on page(s) 1.

[126] S. Oerlemans. Wind turbine noise: primary noise sources. *National Aerospace Laboratory NLR*, 2011. Cited on page(s) 55.

[127] S. Oerlemans, P. Sijtsma, and B. Méndez López. Location and quantification of noise sources on a wind turbine. *Journal of Sound and Vibration*, 299(4):869–883, 2007. Cited on page(s) 86.

[128] R. R. Parchen. *Progress report DRAW: A prediction scheme for trailing edge noise based on detailed boundary layer characteristics*. TNO Institute of Applied Physics, 1998. Cited on page(s) 89.

[129] E. Pedersen, F. van den Berg, R. Bakker, and J. Bouma. Response to noise from modern wind farms in the netherlands. *The Journal of the Acoustical Society of America*, 126(2):634–643, aug 2009. Cited on page(s) 1.

[130] S. Pirozzoli. Numerical methods for high-speed flows. *Annual Review of Fluid Mechanics*, 43(1):163–194, jan 2011. Cited on page(s) 35.

[131] F. Porté-Agel, M. Bastankhah, and S. Shamsoddin. Wind-turbine and wind-farm flows: A review. *Boundary-Layer Meteorology*, 174(1):1–59, sep 2019. Cited on page(s) xiii, 3.

[132] B. Rajani, A. Kandasamy, and S. Majumdar. Numerical simulation of laminar flow past a circular cylinder. *Applied Mathematical Modelling*, 33(3):1228–1247, Mar. 2009. Cited on page(s) xv, 78, 79.

[133] P. Roe and J. Pike. Efficient construction and utilisation of approximate riemann solutions. In *Proc. of the sixth int'l. symposium on Computing methods in applied sciences and engineering, VI*, pages 499–518, 1985. Cited on page(s) 21.

[134] P. L. Roe. Approximate riemann solvers, parameter vectors, and difference schemes. *Journal of computational physics*, 43(2):357–372, 1981. Cited on page(s) 21.

[135] M. Roger and S. Moreau. Back-scattering correction and further extensions of amiet's trailing-edge noise model. part 1: theory. *Journal of Sound and vibration*, 286(3):477–506, 2005. Cited on page(s) 55, 87, 88.

[136] A. L. Rogers, J. F. Manwell, and S. Wright. Wind turbine acoustic noise. *Renewable Energy Research Laboratory, Amherst: University of Massachusetts*, 2006. Cited on page(s) 1.

[137] Y. Rozenberg, G. Robert, and S. Moreau. Wall-pressure spectral model including the adverse pressure gradient effects. *AIAA journal*, 50(10):2168–2179, 2012. Cited on page(s) 89.

[138] Y. Rozenberg, M. Roger, and S. Moreau. Rotating blade trailing-edge noise: Experimental validation of analytical model. *AIAA journal*, 48(5):951–962, 2010. Cited on page(s) 126.

[139] A. Rueda-Ramírez and G. Gassner. A subcell finite volume positivity-preserving limiter for DGSEM discretizations of the euler equations. In *14th WCCM-ECCOMAS Congress*. CIMNE, 2021. Cited on page(s) 49.

[140] A. M. Rueda-Ramírez, J. Manzanero, E. Ferrer, G. Rubio, and E. Valero. A p-multigrid strategy with anisotropic p-adaptation based on truncation errors for high-order discontinuous galerkin methods. *Journal of Computational Physics*, 378:209 – 233, 2019. Cited on page(s) 2.

[141] P. Schlatter and R. Örlü. Turbulent boundary layers at moderate reynolds numbers: inflow length and tripping effects. *Journal of Fluid Mechanics*, 710:5–34, aug 2012. Cited on page(s) 57.

[142] R. Schlinker and R. Amiet. Helicopter rotor trailing edge noise. In *7th Aeroacoustics Conference*, page 2001, 1981. Cited on page(s) 126.

[143] J. Schluntz and R. H. J. Willden. An actuator line method with novel blade flow field coupling based on potential flow equivalence. *Wind Energy*, 18(8):1469–1485, 2015. Cited on page(s) 100.

[144] N. Sharma and T. K. Sengupta. Vorticity dynamics of the three-dimensional taylor-green vortex problem. *Physics of Fluids*, 31(3):035106, 2019. Cited on page(s) 45.

[145] W. Z. Shen. Actuator line simulation of wind turbine wakes. *Journal of Computational Physics*, 229(9):3135–3154, 2010. Cited on page(s) 98.

[146] W. Z. Shen, J. A. Michelsen, and J. N. Sørensen. A collocated grid finite volume method for aeroacoustic computations of low-speed flows. *Journal of Computational Physics*, 196(1):348–366, May 2004. Cited on page(s) xv, 79, 80.

[147] W. Z. Shen, R. Mikkelsen, J. N. Sørensen, and C. Bak. Tip loss corrections for wind turbine computations. *Wind Energy*, 8(4):457–475, 2005. Cited on page(s) 107.

[148] S. Sherwin. Dispersion analysis of the continuous and discontinuous Galerkin formulations. In *in International Symposium on Discontinuous Galerkin Methods*, pages 425–431. Springer, 1999. Cited on page(s) 28.

[149] T. C. &. C.-W. Shu. Review article:review of entropy stable discontinuous galerkin methods for systems of conservation laws on unstructured simplex meshes. *CSIAM Transactions on Applied Mathematics*, 1(1):1–52, jun 2020. Cited on page(s) 31.

[150] S. Sinayoko, M. Kingan, and A. Agarwal. Trailing edge noise theory for rotating blades in uniform flow. *Proceedings of the Royal Society A: Mathematical, Physical and Engineering Sciences*, 469(2157):20130065, 2013. Cited on page(s) 126, 127, 129.

[151] J. Smagorinsky. General circulation experiments with the primitive equations. *Monthly Weather Review*, 91(3):99–164, 1963. Cited on page(s) 48.

[152] J. Smagorinsky. General circulation experiments with the primitive equations: I. the basic experiment. *Monthly weather review*, 91(3):99–164, 1963. Cited on page(s) 29, 131.

[153] J. N. Sørensen, R. F. Mikkelsen, D. S. Henningson, S. Ivanell, S. Sarmast, and S. J. Andersen. Simulation of wind turbine wakes using the actuator line technique. *Philosophical Transactions of the Royal Society A: Mathematical, Physical and Engineering Sciences*, 373(2035):20140071, feb 2015. Cited on page(s) 98, 99.

[154] J. N. Sørensen, R. F. Mikkelsen, and K. Hjort. Wind farm turbulence and its impact on wind turbine performance. *Wind Energy*, 18(7):1257–1278, 2015. Cited on page(s) 98.

[155] J. N. Sorensen and W. Z. Shen. Numerical modeling of wind turbine wakes. *J. Fluids Eng.*, 124(2):393–399, 2002. Cited on page(s) 98, 99.

[156] P. R. Spalart and M. L. Shur. Variants of the ffowcs williams - hawkings equation and their coupling with simulations of hot jets. *International Journal of Aeroacoustics*, 8(5):477–491, jul 2009. Cited on page(s) 71.

[157] O. Stalnov, P. Chaitanya, and P. F. Joseph. Towards a non-empirical trailing edge noise prediction model. *Journal of Sound and Vibration*, 372:50–68, 2016. Cited on page(s) 55, 88, 89.

[158] R. J. Stevens, L. A. Martínez-Tossas, and C. Meneveau. Comparison of wind farm large eddy simulations using actuator disk and actuator line models with wind tunnel experiments. *Renewable Energy*, 116:470–478, 2018. Cited on page(s) 98.

[159] R. J. Stevens and C. Meneveau. Flow structure and turbulence in wind farms. *Annual Review of Fluid Mechanics*, 49(1):311–339, 2017. Cited on page(s) 98.

[160] A. Tadamasa and M. Zangeneh. Numerical prediction of wind turbine noise. *Renewable Energy*, 36(7):1902–1912, jul 2011. Cited on page(s) 126.

[161] Y. Tian and B. Cotté. Wind turbine noise modeling based on amiet's theory: Effects of wind shear and atmospheric turbulence. *Acta Acustica united with acustica*, 102(4):626–639, 2016. Cited on page(s) 126.

[162] G. G. Tong, D. Kamensky, and J. A. Evans. Skeleton-stabilized divergence-conforming b-spline discretizations for incompressible flow problems of high reynolds number. *Computers & Fluids*, 248:105667, 2022. Cited on page(s) 42.

[163] E. F. Toro. *Riemann solvers and numerical methods for fluid dynamics: a practical introduction*. Springer Science & Business Media, 2013. Cited on page(s) 21.

[164] N. Troldborg. *Actuator Line Modeling of Wind Turbine Wakes*. PhD thesis, DTU Wind Energy, Jan. 2009. Cited on page(s) 98, 99.

[165] N. Troldborg, J. Sørensen, and R. Mikkelsen. Numerical simulations of wake characteristics of a wind turbine in uniform inflow. *Wind Energy*, 13:86–99, 2010. Cited on page(s) 102.

[166] N. Troldborg, F. Zahle, P.-E. Réthoré, and N. N. Sørensen. Comparison of wind turbine wake properties in non-sheared inflow predicted by different computational fluid dynamics rotor models. *Wind Energy*, 18(7):1239–1250, 2015. Cited on page(s) 98, 118, 123.

[167] H. Versteeg and W. Malalasekera. *An introduction to computational fluid dynamics: The finite volume method*. Prentice Hall, 2 edition, 2007. Cited on page(s) 27, 29.

[168] A. W. Vreman. An eddy-viscosity subgrid-scale model for turbulent shear flow: Algebraic theory and applications. *Physics of Fluids*, 16(10):3670–3681, oct 2004. Cited on page(s) 30.

[169] A. W. Vreman. An eddy-viscosity subgrid-scale model for turbulent shear flow: Algebraic theory and applications. *Physics of Fluids*, 16(10):3670–3681, 2004. Cited on page(s) 48.

[170] H. Wang, I. Sihar, R. P. Muñoz, and M. Hornikx. Room acoustics modelling in the time-domain with the nodal discontinuous galerkin method. *The Journal of the Acoustical Society of America*, 145(4):2650–2663, apr 2019. Cited on page(s) 71.

[171] Z. Wang, K. Fidkowski, R. Abgrall, F. Bassi, D. Caraeni, A. Cary, H. Deconinck, R. Hartmann, K. Hillewaert, H. Huynh, N. Kroll, G. May, P.-O. Persson, B. van Leer, and M. Visbal. High-order cfd methods: current status and perspective. *International Journal for Numerical Methods in Fluids*, 72(8):811–845, 2013. Cited on page(s) xiv, 31, 47.

[172] J. E. F. Williams and D. L. Hawkings. Sound generation by turbulence and surfaces in arbitrary motion. *Philosophical Transactions of the Royal Society of London. Series A, Mathematical and Physical Sciences*, 264(1151):321–342, may 1969. Cited on page(s) 70, 71.

[173] J. H. Williamson. Low-storage Runge-Kutta schemes. *Journal of Computational Physics*, 35(1):48–56, 1980. Cited on page(s) 22.

[174] W. R. Wolf and S. K. Lele. Aeroacoustic integrals accelerated by fast multipole method. *AIAA Journal*, 49(7):1466–1477, jul 2011. Cited on page(s) 71, 74.

[175] W. R. Wolf and S. K. Lele. Fast acoustic scattering predictions with non-uniform potential flow effects. *Journal of the Brazilian Society of Mechanical Sciences and Engineering*, 35(4):407–418, jun 2013. Cited on page(s) 71, 74.

[176] Y.-T. Wu and F. Porté-Agel. Large-eddy simulation of wind-turbine wakes: evaluation of turbine parametrisations. *Boundary-layer meteorology*, 138:345–366, 2011. Cited on page(s) 98.

[177] X. Yang and F. Sotiropoulos. Large eddy simulation of wind turbine wakes: Evaluation of turbulence models. *Wind Energy*, 18(4):625–642, 2015. Cited on page(s) 98.

[178] T. A. Zang. On the rotation and skew-symmetric forms for incompressible flow simulations. *Applied Numerical Mathematics*, 7(1):27–40, jan 1991. Cited on page(s) 28.

[179] W. J. Zhu, W. Z. Shen, E. Barlas, F. Bertagnolio, and J. N. Sørensen. Wind turbine noise generation and propagation modeling at DTU wind energy: A review. *Renewable and Sustainable Energy Reviews*, 88:133–150, may 2018. Cited on page(s) 126.

[180] M. Zormpa, S. L. Clainche, E. Ferrer, C. Vogel, and R. Willden. Dynamic mode decomposition of merging wind turbine wakes. *Journal of Physics: Conference Series*, 2505(1):012020, may 2023. Cited on page(s) 113.